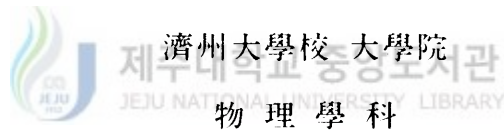


博士學位論文

Studies on Quantum Transport and Single Electron
Tunneling in Quantum Nanostructure Systems



李 尙 七

110.361

2000年 12月

Studies on Quantum Transport and Single Electron Tunneling in Quantum Nanostructure Systems

指導教授 柳 在 演

李 尙 七

이 論文을 理學 博士學位 論文으로 提出함



李 尙 七의 理學 博士學位 論文을 認准함

審査委員長 _____ 印
委 員 _____ 印
委 員 _____ 印
委 員 _____ 印
委 員 _____ 印

濟州大學校 大學院

2000年 12月

Studies on Quantum Transport and Single Electron Tunneling in Quantum Nanostructure Systems

Sang-Chil Lee
(Supervised by Professor Jai-Yon Ryu)

A Thesis Submitted in Partial Fulfillment of the Requirements
for the Degree of Doctor of Philosophy in Physics

2000. 11.

This thesis has been examined and approved.

DEPARTMENT OF PHYSICS
GRADUATE SCHOOL
CHEJU NATIONAL UNIVERSITY

Contents

	Abstract	vii
I	Introduction	1
II	Transverse Electric-Field-Induced Magnetophonon Resonance in n-type Germanium	9
	A Model of the System	11
	B Field-Dependent Magnetoconductivity Associated with Relaxation Rates	12
	C Results and Conclusions	16
III	Magnetophonon Resonance of Quasi-Two-Dimensional Electronic System in Tilted Magnetic Fields	22
	A Model for Q2D Electronic System in Tilted Magnetic Fields	23
	B Magnetoconductivity Associated with Relaxation Rates	25
	C Magnetophonon Resonances in Tilted Magnetic Fields	27
	D Numerical Results and Discussion	30
IV	Magnetophonon and Electrophonon Resonances in Quantum Wires	35
	A Model for Quantum Wires	36
	B Magnetophonon and Electrophonon Resonances	39
	C Numerical Results	42
	D Conclusions	47

V	Magnetophonon Resonances in Quasi-One-Dimensional Electronic Systems in Tilted Magnetic Fields	49
A	Model for Q1D Electronic Systems in Tilted Magnetic Fields	51
B	Magnetoconductivity Associated with Relaxation Rates	54
C	Numerical Results and Discussion	59
D	Conclusions	76
VI	Magnetophonon Resonances in the Miniband Transport in Semiconductor Superlattices	79
A	Electronic Model	81
B	Magnetoconductivity Associated with Relaxation Rates	83
C	Numerical Results and Discussion	88
D	Conclusions	96
VII	Exact Solution of the Electrostatic Problem for a Single Electron Dual-Junction-Array Trap	98
A	Potential Profile	102
B	Free Energy and Charging Energy	105
C	Threshold Voltage	107
D	Numerical Results	109
E	Conclusions	117
VIII	Hysteretic Voltage Gap for a Single Electron Dual-Junction-Array Trap with Stray Capacitances	120
IX	Conclusions	136

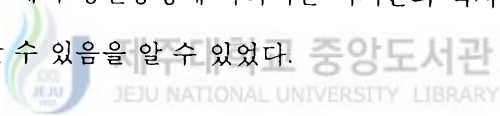
References	140
Curriculum Vitae	146
Acknowledgements	153



초 록

양자 나노 구조계에서의 두 가지 주제, 즉 (1) 3차원, 준2차원 전자계인 양자우물과 준1차원 전자계인 양자선, 초격자에서의 자기포논 공명효과와 전자포논 공명효과, 및 (2) 단일전자 이중 트랩 소자계에서의 저지전압과 이력 전압차에 대하여 연구하였다. 3차원 전자계인 n-형 게르마늄 물질에서 뜨거운 전자 영역의 자기포논 공명현상을 조사하였다. 이러한 전자계에서는 내부 충돌장 효과에 기인한 비 수직 천이에 의해서 공명정점의 쪼개짐 현상이 발생한다는 것을 알 수 있었다. 그들의 정점 중 하나는 전기장의 세기가 증가하거나 가능한 포논 에너지와 란다우 지수 차가 감소할 때, 공명 자기장이 낮은 방향으로 이동하고 또 다른 하나는 공명 자기장이 증가하는 방향으로 이동한다는 것을 알 수 있고, 또한 공명정점이 초기상태와 최종상태 사이의 유효질량 차이로 발생하는 자기장 방향에 의존한다는 것을 알 수 있었다. 자기장이 수직으로 걸릴 때의 준1차원 전자계인 양자선에서 자기포논 및 전자포논 공명현상을 다양한 구속퍼텐셜에 대해서 조사하였다. 3차원 전자계와는 달리 이러한 저차원 전자계에서는 구속퍼텐셜에 의해서 형성된 부 준위로 말미암아 전자포논 공명현상과 자기포논 공명 정점의 쪼개짐 현상 및 정점의 이동이 발생하게 된다. 특히, 이러한 공명효과의 자기장, 우물두께, 구속진동수, 및 바이어스 전압에 따른 의존성을 상세히 제시하였다. 만약, 자기장이 경사지게 걸리는 경우에는 준 2차원 및 준 1차원 전자계에서 경사진 자기장과 구조적으로 주어지는 정전위 페텐셜에 의해서 형성된 란다우 준위의 가상 비공명 천이로 인하여 보조 자기포논 공명정점이 나타나고, 이러한 자기포논 공명정점 위치는 구조적인 구속퍼텐셜 진동수와 자기장의 방향 및 세기에 의존한다는 사실이다. 게다가 위의 조건으로부터 자기장이 가해지지 않은 경우에는 구속퍼텐셜에 의해서 전자포논 공명이 발생하게 되어 전기전도도는 이러한 공명현상으로 인해서 진동하는 형태를 가지게 된다. 또한, 보조 자기포논 공명정점의 발생, 자기포논 공명정점의 이동, 그리고 자기포논 공명 진폭과 너비의 변화와 같은 자기포논 공명의 선모양에 대해서 자세히 조사하였다. 초격자계에서는 미니밴드 너비와 온도에 따라서 자기포논 공명효과를 분석하였다. 특히, 자기포논 공명정점들 사이에서의 평활영역의 존재, 자기포논 공명정점의 사라짐과 자기포논 공명 진폭의 변화와 같은 자기포논 공명의 선모양을 자

세히 제시하였다. 학위 논문의 두 번째 주제로서 차세대 메모리소자로 각광을 받고있는 단일 전자 이중트랩 소자의 정전위 문제에 대한 해석적인 완전 해를 제시하였다. 여기서 이 소자는 동일한 여러 개의 스트레이 정전용량, 동일한 여러 개의 소자 정전용량, 동일한 두 개의 입력 게이트 정전용량 및 하나의 결합 정전용량으로 구성된다. 이러한 이중배열소자에서의 저지 전압과 이력 전압차를 다양한 전하 솔리톤, 즉 단일 전자, 엑시톤 및 엑시톤-전자 결합 솔리톤에 대해서 조사하였다. 저지전압과 이력전압차는 동시 터널링, 스트레이 정전용량, 소자 정전용량, 입력 게이트 정전용량 및 결합 정전용량에 민감하게 의존하고, 이러한 변수에 의해서 다양한 전하 솔리톤 수송 현상이 발생하게 된다. 본 연구에서는 스트레이 정전용량 효과를 고려하였고, 그 효과가 전하 솔리톤 수송에 중요한 역할을 한다는 것과 임계 스트레이 정전용량 값 이상에서는 이력 곡선이 존재하지 않음을 보였다. 스트레이 정전용량이 없는 경우에는 엑시톤이 보다 안정적인 단전자 회로를 구성하지만, 스트레이 정전용량에 따라서는 엑시톤과 엑시톤-전자 결합 솔리톤이 안정적인 단전자 회로를 구성할 수 있음을 알 수 있었다.



I. INTRODUCTION

With the continuous advance in epitaxial technologies and lithographic or etching techniques, various studies of low-dimensional systems such as quantum-well structures, quantum-wire structures, quantum-dot structures, superlattice structures, and one-dimensional (1D) quantum box array structures have been in progress for several years. Among these, the investigation of quantum resonance effects, such as magnetophonon resonance (MPR) [1,2] and electrophonon resonance (EPR) [3] in low-dimensional electronic systems is a subject of great current interest since it can be used as a powerful spectroscopic tool to investigate various transport properties in nanostructures.

The MPR effect was predicted by Gurevich and Firsov [2], which can be used a powerful spectroscopic tool to investigate the physical properties such as a precision determination of the effective mass and the detailed information of electron-phonon interactions in semiconductors. Under the action of a magnetic field, the MPR effect occurs whenever the optical phonon energy is equal to an integral multiple of energy separations between two Landau levels, and the ordinary MPR condition is given as

$$N\hbar\omega_c = \hbar\omega_{LO}, \quad N = 1, 2, 3, \dots, \quad (1.1)$$

where $\omega_c = eB_N/m^*$ is the cyclotron frequency of the electron with the effective mass m^* in the resonance magnetic field B_N and $\hbar\omega_{LO}$ is the longitudinal optical (LO) phonon energy. The resonances which are caused by the absorption of thermally generated phonons at high temperatures in low electric fields (linear regime) are known as the “normal” MPR effect. These resonances are almost exclusively due to the absorption of LO phonons, and due to the requirement that there should be a significant phonon population, they are usually only observed at temperatures above

$\sim 50 K$. The scattering process causes a relaxation of carrier momentum, which is then reflected in the various transport coefficients of the material under study. A necessary condition for observing the “ normal ” MPR effect is (1) that Landau levels should be sharp and well defined so that $\omega_c\tau \gg 1$ (τ is the mean time between collisions), (2) that scattering by LO phonons should make a significant contribution to limiting the carrier transport, and (3) that temperature is high enough (typically $T > 77K$) such that there exist a sufficient number of LO phonons needed for absorption.

These three factors combine to give the characteristic temperature dependence of the amplitude of the oscillations. At high temperatures the thermal broadening of the Landau levels reduces the strength of the resonant extrema, while at lattice temperatures well below the characteristic temperature of the LO phonon, the population of the phonons falls off and the scattering is no longer important. There is thus an optimum temperature for the observation of magnetophonon oscillations, which is typically in $50 \sim 150 K$ depending on the LO phonon energy.

At low temperatures, in degenerate materials, conduction takes place within a small region around the Fermi energy. As the magnetic field changes, the singularities at the bottom of each Landau level cross the Fermi level in succession, and thus give rise to a succession of structures in the resistivity which are periodic in $1/B$. The first experimental demonstration of this effect was the observation by Shubnikov and de Hass of small oscillations in the magnetoresistance of bismuth [1]. These oscillations, known as Shubnikov-de Hass effects, are observed at very low temperatures, around $4.2K$, and are dependent upon the carrier concentration in the material. In contrast the MPR effect usually occurs at higher temperatures, and is almost independent of electron concentration.

From the above discussion, the magnetophonon oscillations may be easily distinguished from Shubnikov-de Hass oscillations which are strongest at the lowest temperatures and almost universally show a rapid fall in amplitude as temperature increases. The periodicity of the magnetophonon oscillations is almost independent of the electron concentration, except for a small shift due to non-parabolicity, in contrast to the Shubnikov-de Hass periodicity. Shubnikov-de Hass oscillations are only observed in degenerate semiconductors with a high carrier concentration, while the MPR effect is more usually observed in pure, non-degenerate samples where the mobility is higher, although both effects may be observed in the same sample of some narrow gap materials.

When the lattice temperature is reduced below 20 K in low electric fields the LO phonon population has fallen so much that magnetophonon oscillations due to the absorption of phonons are no longer observable. It has been found, however, that when the electric field applied to the sample is increased the oscillations may be made to reappear. This is due to the heating of the carriers by the electric field called the hot-electron effect so that phonons may then be emitted. When the magnetic field satisfies the resonance condition, a rapid emission of phonons occurs at resonance, there is a resonant cooling of the carriers, and the electron temperature decreases. This change in electron temperature affects the transport properties, and a series of oscillations in the magnetoresistance results. The reappearance of MPR effect called the hot-electron MPR effect at low temperatures in high electric fields (non-linear regime) usually reflects the magnetic field dependence of energy relaxation time rather than any direct variation in the momentum relaxation time. Because the energy of acoustic phonons is much smaller than that of LO phonon, the energy relaxation process is dominated by emission of LO phonons.

Since electron-electron scattering is rapid compared with the momentum relaxation rate, the resonant cooling produces almost identical structure in the transverse and longitudinal magnetoresistances.

Another example of a resonant energy loss or gain process is when the phonon energy is equal to energy separation between two subband levels in low-dimensional electron gas system. This also gives rise to resonant structure in the transport coefficients, and is known as the EPR effect [3]. The EPR condition is given as

$$\Delta E_{mn} = |E_n - E_m| = \hbar\omega_{LO}, \quad (1.2)$$

where m and n are subband indices, respectively. The EPR has been recently realized in a graded quantum well. To explain this phenomena theoretically, some authors [3] have investigated the EPR effect in a quasi-two-dimensional electronic system. However, concerning the hot-electron MPR and the hot-electron EPR in low-dimensional systems, to the best of our knowledge, we are not aware of theoretical work and are still at an initial stage both experimentally and theoretically. It is therefore desired to develop a theory which could analyze MPR, EPR, hot-electron MPR, and hot-electron EPR effects, in low-dimensional systems, ranging from very small (linear regime) to large electric fields (hot-electron regime).

In this thesis, we study theoretically MPR, EPR, hot-electron MPR, and hot-electron EPR effects in low-dimensional systems with various confinement potentials including a parabolic well, a square well, and a triangular well, using the formalism of nonlinear response theory developed previously by Ryu et al. [4].

As the second subject, single electron tunneling (SET) in ultras-small tunnel junctions is investigated. The tunneling of a single charge across a tunneling barrier can seriously affect the macroscopic state of the system. Furthermore, because of the so-called Coulomb blockade, the microscopic tunneling transitions may be controlled by

means of macroscopic applied voltages such as bias or gate voltages. SET devices whose fundamental operation principle is based on the Coulomb blockade effect, where it is found that in a single small tunnel junction, having tunnel resistance R_T and capacitance C , such that $R_T \gg R_k = h/e^2 = 25.8k\Omega$ and charging energy $E_c = e^2/2C$ exceeds the characteristic energy $k_T T$ of thermal fluctuations, i.e., $E_c \gg k_T T$, a suppression of single charge tunneling dramatically reduces the current at voltages $V < e/2C$. In practice, only islands having capacitances not much below a fF can be reliably designed, thus imposing experiments done at a few tens of mK, now attainable with a dilution refrigerator. Essentially, condition $R_T \gg R_k$ ensures that the wave function of an excess electron on an island is localized there. Conditions $R_T \gg R_k$ and $E_c \gg k_T T$ ensure that the transport of charge from island to island is governed by the Coulomb charge energy. A lot of work have been made on the physics of SET phenomena and on the wide variety of SET device applications [5,6].

These devices have been widely used to transfer, with the help of the Coulomb blockade effect, and are, in particular, potentially useful for metrological applications such as fundamental standards of dc current and for digital devices. The most remarkable candidates for such standards are the single electron turnstile, where a gate electrode controlled by an rf signal is capacitively coupled to the center of the array, and the single electron pump, where two gate electrodes controlled by two rf signals are capacitively coupled to the electrodes inside the array. One of the most important features of these devices is that they all contain 1D long arrays of small tunnel junctions. The use of long arrays results in at least three advantages: (1) it is easier to fabricate high quality devices with high R_T and low C in the form of long arrays; (2) the electromagnetic environment influence, which tends to smear the

Coulomb blockade effect, can be kept at a minimum; (3) it possesses some unique features of electronic transfer such as space correlation. Therefore, the study of long arrays is a key to understand the physics of these devices. However, it is known that charge fluctuations give rise to small deviation from the controlled dc current flowing through these devices. Thus for possible metrological applications of these devices, it is essential to know the error rate of the operation, which depends on how frequent and by what processes the electrons transit the device in the presence of Coulomb barrier.

The starting point in studying the electrostatics of the long array systems is to identify the potential profiles for a given set up of the system. The key to our approach is to rewrite electrostatic equations as matrix equations for the island potentials $\{\varphi_i\}$; this enables us to derive the electrostatic equations in a tridiagonal matrix form and obtain an exact analytic result for the finite 1D array of tunnel junctions. With the help of the exact solution of the electrostatics of a 1D arrays, we can also solve the electrostatic problems of other single electron device with long arrays, such as trap, pump, and turnstile. Although the bias voltage controls the average value of the current passing through the system, the dynamics of an electron in the system at $T = 0$ is in principle solely determined by the Gibbs free energy. The transfer of an electron from one island to another through the tunnel junction between them is favorable if the Gibbs free energy decreases in this process, and vice versa. Thus the essence of the dynamics is the evaluation of the Gibbs free energy, which consists of a charging energy term and a work done term. The above mentioned exact solutions of the electrostatics for the long arrays systems enable us to perform systematic studies for the Gibbs free energy and derive an exact analytical form for it at arbitrary charge configurations.

In this thesis, we first find an exact analytical solution to the electrostatic problem of the single electron dual-junction-array trap, which consists of equal stray capacitances C_0 , equal junction capacitances C , equal input gate capacitances C_1 , and coupling capacitance C_C . Second, we analyze the dynamics of single charge transfer for various charge solitons including a single electron, an exciton, and a combined exciton and single electron by studying the change of the Gibbs free energy.

This thesis is organized as follows. In chapter 2, we examine the influence of the intracollisional field effect in the hot-electron regime of the transverse magnetophonon resonances in n -type germanium. In chapter 3, we deal with the physical characteristics of the MPR effects in quasi-two-dimensional electronic system brought about by the electron confinement due to the electrostatic potential and the magnetic confinement by tilting a magnetic field. In chapter 4, we study magnetophonon resonances and electrophonon resonances for various confinement potentials in quantum wires. Occupation of several electric subbands due to these confinement potentials leads to electrophonon resonances and the splitting and shift of MPR peak positions. Dependence of both resonance peak positions on the magnetic field, the thickness of the well, the confinement frequency, and the bias field is shown explicitly. In chapter 5, we obtain the magnetoconductivity in quasi-one-dimensional electronic systems in tilted magnetic fields, based on a simple model of parabolic confining potentials, and investigate the qualitative features of the MPR effects according to the strength of electrostatic potentials and the tilt angle of the applied magnetic field in the quantum limit condition. In particular, the behaviors of the MPR lineshape, such as the appearance of subsidiary MPR peaks, the shift of these MPR peaks, and a change in MPR amplitude and width will be examined

in detail. In chapter 6, we obtain the longitudinal magnetoconductivity of superlattices for polar and nonpolar optical LO phonons and investigate the qualitative features of the MPR effects according to the miniband width and the temperature. In particular, the behaviors of the MPR lineshape, such as the appearance of plateau between neighboring MPR peaks, the disappearance of MPR peaks, and a change in MPR amplitude will be investigated in detail. In chapters 7 and 8, we present an exact analytical solution to the electrostatic problem of the biased single electron dual-junction-array trap consisting of equal stray capacitances C_0 , equal junction capacitances C , equal input gate capacitances C_1 , and coupling capacitance C_C . The threshold voltages are investigated for various charge solitons including a single electron, an exciton, and a combined exciton and single electron. The hysteretic voltage gap $\Delta V(m)$, the difference between the threshold voltages for single charge soliton to tunnel into and escape from a single electron dual-junction-array trap through an m -junction cotunneling process, is investigated for various charge solitons including a single electron, an exciton, and a combined soliton. Conclusions will be presented in the last chapter.

II. TRANSVERSE ELECTRIC-FIELD-INDUCED MAGNETOPHONON RESONANCE IN N-TYPE GERMANIUM

With the recent advance of pulsed high magnetic field technique, it has been possible to measure the MPR effect in very high magnetic field. Many studies on the ordinary and hot-electron MPR effects in *n*-type Ge have been made for the longitudinal and transverse configuration [1,7-12]. It is known that Ge exhibits rich spectra of MPR because optical phonons and zone edge acoustic phonons couple with electrons by the deformation potential interaction although it is not a polar semiconductor. The MPR spectra in *n*-type Ge is quite complicated due to the complexity of phonon branches and the variety of intervalley transitions, which results in difficulties in the assignment of each electronic transition [12]. In the high-field range, the MPR peaks for *n*-type Ge are well resolved from each other, so that one can assign each peak to a specific transition.

For the transverse magnetoconductivity configuration, where the current and the magnetic field directions are perpendicular to each other, Harper et al. [9] presented the experimental results of MPR in *n*-Ge for the magnetic field parallel to the $\langle 100 \rangle$ and $\langle 110 \rangle$ directions. Their results show that the transverse magnetoconductivity oscillates as a function of the magnetic field. Eaves et al. [7] also presented the experimental results of MPR in *n*-Ge for the magnetic field parallel to the $\langle 100 \rangle$ and $\langle 111 \rangle$ directions. A recent review of the MPR effects was given by Ridley [10].

For the longitudinal hot-electron magnetoconductivity configuration, where the current and the magnetic field directions are parallel, Hamaguchi et al. [1,8] found that in the electric field ranging from 17 V/cm to 73 V/cm several different series

of oscillations for the $\langle 100 \rangle$ direction of n -Ge at 20 K were present. Recently, Futagawa et al. [12] presented the new experimental results of n -type Ge for the magnetic field direction parallel to the $\langle 100 \rangle$, $\langle 111 \rangle$, and $\langle 110 \rangle$ directions. Their results show that the dominant MPR signal arises from the hot-electron transitions from the valley with lighter cyclotron mass to the valley with heavier mass in n -type Ge. It was also shown that the hot-electron MPR peaks are observed for the intervalley and intravalley scatterings. Note that all the experiments discussed above were performed for the case where the intracollisional field effect (ICFE) are not effective in the hot-electron regime. Therefore, our concerns are to investigate the changes of the resonance fields due to the ICFE which are effective in the hot-electron regime with electric fields of the order of 10^5 V/cm [13].

In this work, we present a theory of transverse electric-field-induced MPR in n -type Ge, on the basis of the high-field quantum-statistical transport theory [4] developed by some of the present authors, and investigate the MPR extrema of n -type Ge for the magnetic field direction parallel to the $\langle 100 \rangle$, $\langle 110 \rangle$, and $\langle 111 \rangle$ directions as the strength of the electric fields increases.

The rest of the chapter is arranged as follows. In Sec. A, we describe a simple model of the system. In Sec. B, we present the field-dependent magnetoconductivity formula related to the relaxation rate, by using the result of nonlinear response theory obtained previously. The transverse hot-electron MPR is discussed, where special attention is given to the MPR peak positions. Results and conclusions are made in Sec. C.

A. Model of the System

We choose Cartesian coordinate axes with the z -axis parallel to the principal axis of an ellipsoidal energy surface. In the presence of a static magnetic field tilted with an angle of θ from z -axis, $\mathbf{B} = B(\sin \theta, 0, \cos \theta)$, and a uniform external electric field $\mathbf{E} = E\hat{y}$, the one-electron Hamiltonian is given as

$$h_{eE} = \frac{1}{2}(\mathbf{p} + e\mathbf{A}) \begin{pmatrix} 1/m_t & 0 & 0 \\ 0 & 1/m_t & 0 \\ 0 & 0 & 1/m_l \end{pmatrix} (\mathbf{p} + e\mathbf{A}) + eEy, \quad (2.1)$$

where \mathbf{A} is the vector potential, \mathbf{p} is the momentum operator, and m_t and m_l represent the transverse and longitudinal mass components of the ellipsoidal energy surface of the conduction band, respectively. By taking into account the Landau gauge $\mathbf{A} = B(-y \cos \theta, 0, y \sin \theta)$, the one-electron normalized eigenfunctions and eigenvalues of the s valley of the conduction band are, respectively, given by

$$\langle \mathbf{r} | \lambda s \rangle \equiv \langle \mathbf{r} | N, k_x, k_z, s \rangle = U^s(\mathbf{r}) F_\lambda(\mathbf{r}), \quad (2.2)$$

$$E_\lambda^s = E_N^s(k_x, k_z) = \varepsilon_\lambda^s + eEy_\lambda^s + \frac{m_t m_l}{2m_B^s} V_d^2 \quad (2.3)$$

with

$$\varepsilon_\lambda^s = (N + 1/2)\hbar\omega_s + \frac{\hbar^2}{2m_B^s} \left(\frac{\mathbf{k} \cdot \mathbf{B}}{B} \right)^2, \quad (2.4)$$

$$y_\lambda^s = -\frac{\hbar}{eBm_B^s} \left[m_t k_z \sin \theta - m_l k_x \cos \theta + \frac{m_t m_l V_d}{\hbar} \right], \quad (2.5)$$

where $N(= 0, 1, 2, \dots)$ are the Landau-level indices, k_x and k_z are, respectively, the wavevector components of the electron in the x and z direction, the symbol s

in the superscript or subscript indicates the valley index of the conduction band, $V_d(= E/B)$ is the drift velocity, and $\omega_s(= eB/m_s^*)$ and m_B^s are, respectively, the cyclotron frequency and the effective mass in the magnetic field direction, which are

$$\frac{1}{m_s^{*2}} = \frac{\cos^2 \theta}{m_t^2} + \frac{\sin^2 \theta}{m_l m_t}, \quad (2.6)$$

$$m_B^s = m_l \cos^2 \theta + m_t \sin^2 \theta. \quad (2.7)$$

Also in Eq. (2.2), $U^s(\mathbf{r})$ denotes the Bloch function of the s valley and $F_\lambda(\mathbf{r})$ means the envelope function given by

$$F_\lambda(\mathbf{r}) = \frac{1}{\sqrt{L_x L_z}} \phi_N(y - y_\lambda^s) \exp(ik_x x + ik_z z), \quad (2.8)$$

where $\phi_N(y)$ in Eq. (2.8) are the eigenfunctions of the simple harmonic oscillator, and L_x and L_z are, respectively, the x - and z -directional normalization lengths.

We assume that the Bloch function $U^s(\mathbf{r})$ and the envelope function $F_\lambda(\mathbf{r})$ are, respectively, normalized in the crystal as follows:

$$\int_C U^{s*}(\mathbf{r}) U^{s'}(\mathbf{r}) d^3 r = \delta_{s,s'}, \quad (2.9)$$

$$\int_\Omega F_\lambda^*(\mathbf{r}) F_{\lambda'}(\mathbf{r}) d^3 r = \delta_{\lambda,\lambda'}, \quad (2.10)$$

where C is the volume of the unit cell and $\Omega(= L_x L_y L_z)$ is the crystal volume in the real space.

B. Field-Dependent Magnetoconductivity Associated with Relaxation Rates

We now want to evaluate the field-dependent magnetoconductivity $\sigma_{yy}(E)$ for the system modeled in section A, by using eigenfunctions and eigenvalues given in

Eqs. (2.2) and (2.3) and the general expression for the nonlinear dc conductivity $\tilde{\sigma}_{kl}(E)(k, l = x, y, z)$ derived in Ref. 4. It is straightforward to show that the transverse magnetoconductivity $\sigma_{yy}(E)$ can be expressed in terms of Eqs. (2.2) and (2.3) as

$$\sigma_{yy}(E) \cong \frac{\hbar}{\Omega} \sum_{\lambda_s} \sum_{\lambda'_{s'}} |\langle \lambda_s | j_y | \lambda'_{s'} \rangle|^2 \frac{f(\varepsilon_{\lambda}^s) - f(\varepsilon_{\lambda'}^{s'})}{\varepsilon_{\lambda}^s - \varepsilon_{\lambda'}^{s'}} \frac{\Gamma_{\lambda'_{s'}, \lambda_s}(E)}{(E_{\lambda}^s - E_{\lambda'}^{s'})^2}, \quad (2.11)$$

where $j_y = -(e/m_t)p_y$ is the y component of a single electron current operator, $f(\varepsilon_{\lambda}^s)$ is the Fermi-Dirac distribution function associated with the eigenvalue of Eq. (2.4), and $\Gamma_{\lambda'_{s'}, \lambda_s}(E)$ is the field-dependent relaxation rate, which appears in terms of the collision broadening due to the electron-phonon interaction. To obtain Eq. (2.11), we have assumed that the energy difference $(E_{\lambda}^s - E_{\lambda'}^{s'})$ between the Landau energy of s -valley and that of s' -valley is larger than the quantities such as the width and the shift in the spectral line shape, which is usually satisfied and which is in fact the condition to observe the oscillatory behavior of hot-electron MPR [14]. In the intervalley transitions, the matrix elements of the single electron current operator in Eq. (2.11) are given, in terms of Eq. (2.2), by

$$|\langle \lambda_s | j_y | \lambda'_{s'} \rangle|^2 = S(s, s') \delta_{\lambda, \lambda'}, \quad (2.12)$$

where $S(s, s') = |\langle s | j_y | s' \rangle|^2$ and the Kronecker symbols ($\delta_{\lambda, \lambda'} = \delta_{N', N}, \delta_{k_x, k'_x}, \delta_{k_z, k'_z}, \delta_{s, s'}$) denote the selection rules.

Within the first-order Born approximation of scattering processes, the matrix elements of $\Gamma(E)$ associated with the transition between the states $|\lambda_s\rangle$ and $|\lambda_{s'}\rangle$ is generally given [4,14] by

$$M_+ = \sum_{\lambda_1 s_1} |\langle \lambda_{s'} | \gamma_{\mathbf{q}} | \lambda_1 s_1 \rangle|^2 \delta(E_{\lambda_1}^{s_1} - E_{\lambda}^s + \hbar\omega_{\mathbf{q}})$$

$$\begin{aligned}
& + \left| \langle \lambda_1 s_1 | \gamma_{\mathbf{q}}^\dagger | \lambda s \rangle \right|^2 \times \delta(E_{\lambda_1}^{s_1} - E_{\lambda}^{s'} - \hbar\omega_{\mathbf{q}})], \\
M_- = & \sum'_{\lambda_1 s_1} \left[\left| \langle \lambda s' | \gamma_{\mathbf{q}}^\dagger | \lambda_1 s_1 \rangle \right|^2 \delta(E_{\lambda_1}^{s_1} - E_{\lambda}^s - \hbar\omega_{\mathbf{q}}) \right. \\
& \left. + \left| \langle \lambda_1 s_1 | \gamma_{\mathbf{q}} | \lambda s \rangle \right|^2 \right]. \tag{2.14}
\end{aligned}$$

Here $\gamma_{\mathbf{q}} (= C(\mathbf{q}) \exp(i\mathbf{q} \cdot \mathbf{r}))$ represents the one-electron operator. The phonons couple to the electron via the interaction potential $C(\mathbf{q})$, the form of which depends on the type of interaction. It should be noted that the prime on the summation sign in Eq. (2.14) indicates the exclusion of the diagonal element of $\gamma_{\mathbf{q}}$ and $\sum_{\lambda s}$ represents the triple summations $\sum_N \sum_{k_y} \sum_{k_z}$ of the s valley. Also in Eq. (2.14), the δ -functions express the law of energy conservation in one-phonon collision (emission and absorption) processes, where the effect of the electric field (ICFE) is included exactly through the eigenstate E_{λ}^s of an electron. The energy-conserving δ functions in Eq. (2.14) imply that when the electron undergoes a collision by absorbing the energy from the field, its energy can only change by an amount equal to the energy of a phonon involved in the transition. This in fact leads to electric-field-induced MPR. In the representation of Eq. (2.2), the matrix elements in Eq. (2.14) are given by

$$\left| \langle \lambda s | \gamma_{\mathbf{q}} | \lambda' s' \rangle \right|^2 = |C(\mathbf{q})|^2 K(N, N', u) \delta_{k_x, k'_x + q_x} \delta_{k_z, k'_z + q_z} \delta_{s, s'}, \tag{2.15}$$

where

$$K(N, N', u) = \frac{N_n!}{N_m!} \exp(-u) u^{N_m - N_n} [L_{N_n}^{(N_m - N_n)}(u)]^2 \tag{2.16}$$

with

$$u = (l_B^2/2) [q_y^2 + (m_t/m_s^* m_B^s)^2 (m_t q_z \sin \theta - m_l q_x \cos \theta)^2]. \tag{2.17}$$

Here $l_B^s = (\hbar/m_t\omega_s)^{1/2}$, $N_n = \min(N, N')$, $N_m = \max(N, N')$, and $L_m^{(n)}(u)$ is the associated Laguerre polynomial [15].

After some algebra, we obtain from Eqs. (2.14) and (2.15)

$$M_+ \approx M_- \approx |C(\mathbf{q})|^2 \sum_{N', \pm} K(N, N', u) \delta \left[(N' + \frac{1}{2})\hbar\omega_{s'} - (N + \frac{1}{2})\hbar\omega_s \pm \hbar\omega_{\mathbf{q}} + \hbar\Delta \right], \quad (2.18)$$

where $\hbar\Delta$ is the electric-field-dependent quantities given by

$$\hbar\Delta \equiv (m_t m_l V_d^2 / 2) (1/m_B^{s'} - 1/m_B^s) + eE(y_{\lambda'}^{s'} - y_{\lambda}^s). \quad (2.19)$$

To obtain Eq. (2.18) we used the following properties:

$$\delta(x+a) = \sum_{n=0}^{\infty} (-1)^n (a/x)^n \delta(x) \approx \delta(x) \quad (\text{for } x \gg a). \quad (2.20)$$

Then, the relaxation rate (and hence magnetoconductivity) shows, from Eqs. (2.11), (2.13), and (2.18), that the electric-field-induced MPR gives the resonance conditions at

$$(N' + 1/2)\hbar\omega_{s'} = (N + 1/2)\hbar\omega_s \mp \hbar\omega_{\mathbf{q}} - \hbar\Delta, \quad (2.21)$$

where N' and $\hbar\omega_{s'} (= \hbar eB/m_{s'}^*)$, respectively, denote the quantum number and the cyclotron energy of the Landau electron of the s' valley, as do N and $\hbar\omega_s (= \hbar eB/m_s^*)$. These peak positions strongly depend on the difference of Landau-level indices, the difference in the effective mass between the initial and final states of the intervalley scattering by phonons, the involved phonon energy, and the strength of the electric field. If we take the limit $E \rightarrow 0$ in Eq. (2.21), the last term of the right-hand side in Eq. (2.21) vanishes and the expression gives the hot-electron MPR condition, where the ICFE are not effective. These for the transverse configuration are same as the theoretical result of Futagawa et al. [12] obtained for the

longitudinal configuration. In this case, the transition of an electron from the N th excited state in the s valley to the N' th state of the s' valley, associated with the emission of the phonons, occurs at the resonance magnetic field given by

$$B_{NN'}(0) = \frac{B_{FN}}{N + \alpha_{N'}} \quad (B_{FN} = \omega_{\mathbf{q}} m_s^*/e) \quad (2.22)$$

with $\alpha_{N'} = 1/2 - (N' + 1/2)m_s^*/m_{s'}^*$. The MPR conditions for intravalley transition are given by

$$B_{NN'}(0) = B_{FP}/P \quad (B_{FP} = \omega_{\mathbf{q}} m_s^*/e, P = N - N' = 1, 2, 3, \dots) \quad (2.23)$$

if we regard the same cyclotron mass before and after the transitions. In Eq. (2.19), assuming [16] that $y_{\lambda'}^{s'} - y_{\lambda}^s < 0$ or $y_{\lambda'}^{s'} - y_{\lambda}^s > 0$, depending on whether the maximum in the magnetoconductivity appears at magnetic fields $B_{NN'}(E)$ lower or higher than $B_{NN'}(0)$ given by Eq. (2.22), we can make an approximation as $y_{\lambda'}^{s'} - y_{\lambda}^s \simeq \pm \bar{l}_{B'_0} = \pm (l_{B'_0}^{s'} + l_{B'_0}^s)/2$ with $\bar{l}_{B'_0} \approx (\sqrt{\hbar/m_t e B'_0}/2)(\sqrt{m_s^*} + \sqrt{m_{s'}^*})$ and $B'_0 = (2\omega_{\mathbf{q}}/e)(m_s^* m_{s'}^*/|m_{s'}^* - m_s^*|)$. This assumption results in double peaks around the MPR extrema without the ICFE. Eq. (2.19) can, then, be rewritten as

$$\hbar\Delta \equiv (m_t m_l V_d^2/2)(1/m_B^{s'} - 1/m_B^s) \pm eE\bar{l}_{B'_0}. \quad (2.24)$$

Note that we did not perform the calculation of the amplitude of magnetoconductivity oscillation because we are interested in the hot-electron MPR peak positions.

C. Results and Conclusions

In this section, we present the numerical results for MPR peak shifts due to the intracollisional field effect, by using Eqs. (2.21)–(2.24), and analyze these results in terms of the strength of the electric field. For n -type Ge, it is known that the

conservation of momentum allows electrons to be scattered by the phonons at Γ - and X -points [17]. As a result, the possible phonons [18] for n -type Ge are Γ -point LO-TO (37.7 meV), X_4 -point TO (34.2 meV), X_1 -point LA-LO (29.8meV), and X_3 -point TA (9.93 meV).

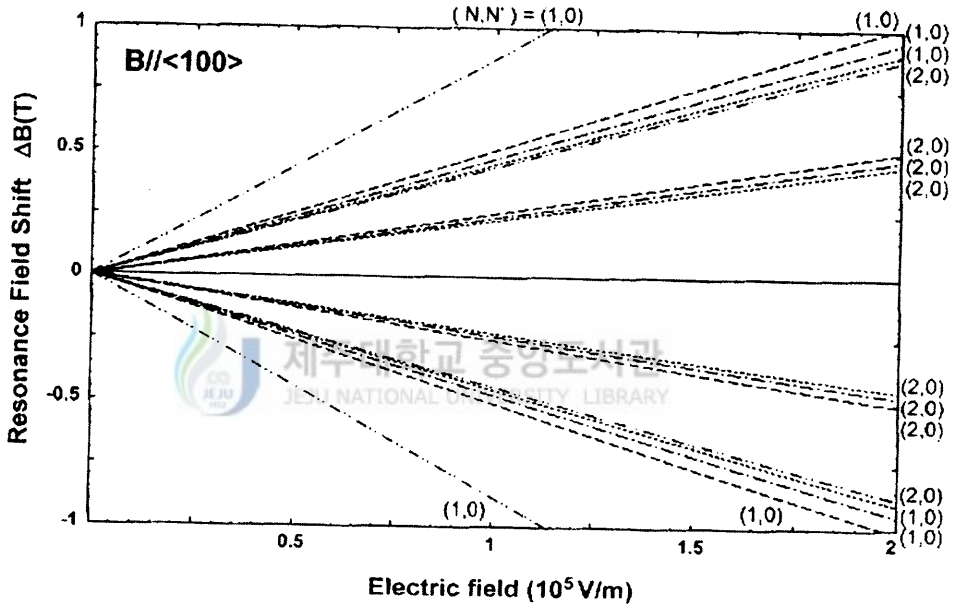


FIG. 1. Resonance field shift of n -Ge for $\mathbf{B} \parallel \langle 100 \rangle$. The quantum number of the Landau level for $m_s^* = 0.135m$ is indicated for each line. The dashed-double dotted, dashed, dashed-dotted, and dotted line are for X_3 -point, X_1 -point, X_4 -point, and Γ -point, respectively.

To visualize the resonance field shifts ΔB associated with the emission of the phonons, we plotted Figs. 1, 2, and 3 corresponding to $\mathbf{B} \parallel \langle 100 \rangle$, $\mathbf{B} \parallel \langle 110 \rangle$ and $\mathbf{B} \parallel \langle 111 \rangle$, respectively, where the dependence of the shifts on the strength of the electric field, the magnetic field direction, the possible phonon energy, and the difference of Landau-level indices is presented. The shifts $\Delta B (\equiv B_{NN'}(E) - B_{NN'}(0))$

are the difference between the field-induced resonant magnetic field $B_{NN'}(E)$ given by Eqs. (2.21) and (2.24) and the resonant field $B_{NN'}(0)$ given by Eq. (2.22) or Eq. (2.23), depending on the type of transitions.

The resonance field shifts of n -Ge in the transverse configuration are presented in Fig. 1 for $\mathbf{B} \parallel \langle 100 \rangle$. The intravalley MPR appears since all the equivalent valleys have an identical effective mass for $\mathbf{B} \parallel \langle 100 \rangle$. As shown in Fig. 1, the shifts increase with decreasing the possible phonon energy, linearly with increasing electric field, and strongly with decreasing the difference of Landau-level indices before and after the intravalley transitions. The splitting of the MPR peak positions take place, which is due to the non-vertical transition at high electric field, as pointed out by Mori et al. [16]. The upper and lower part in the figure correspond to $\Delta y > 0$ and $\Delta y < 0$, respectively. Accordingly, in the former case, the resonance peak positions are shifted to the higher magnetic-field side as electric fields are increased and as the possible phonon energy and the difference of Landau-level indices are decreased, while in the latter case, they are shifted to the lower magnetic-field side as electric fields are increased and as the possible phonon energy and the difference of Landau-level indices are decreased. Note that our results for the limit $E \rightarrow 0$ reduce to the previous results [19] which agree with the experimental values of Eaves et al. [7] and Harper et al. [9] for the transverse configuration and with the experimental values of Hamaguchi et al. [1,8] for the longitudinal configuration.

Unlike the case of $\mathbf{B} \parallel \langle 100 \rangle$, as can be seen from Figs. 2 and 3, the MPR peaks of the intervalley scattering occur at \mathbf{X} -points for $\mathbf{B} \parallel \langle 110 \rangle$ and $\mathbf{B} \parallel \langle 111 \rangle$, due to difference in effective mass between the initial and final states. As illustrated in Fig. 1, the shifts increase with decreasing the possible phonon energy, linearly with increasing electric field, and strongly with decreasing the difference of Landau-level

indices due to before and after the intervalley transitions occurring at \mathbf{X} -points and due to before and after the intravalley transitions occurring at Γ - points.

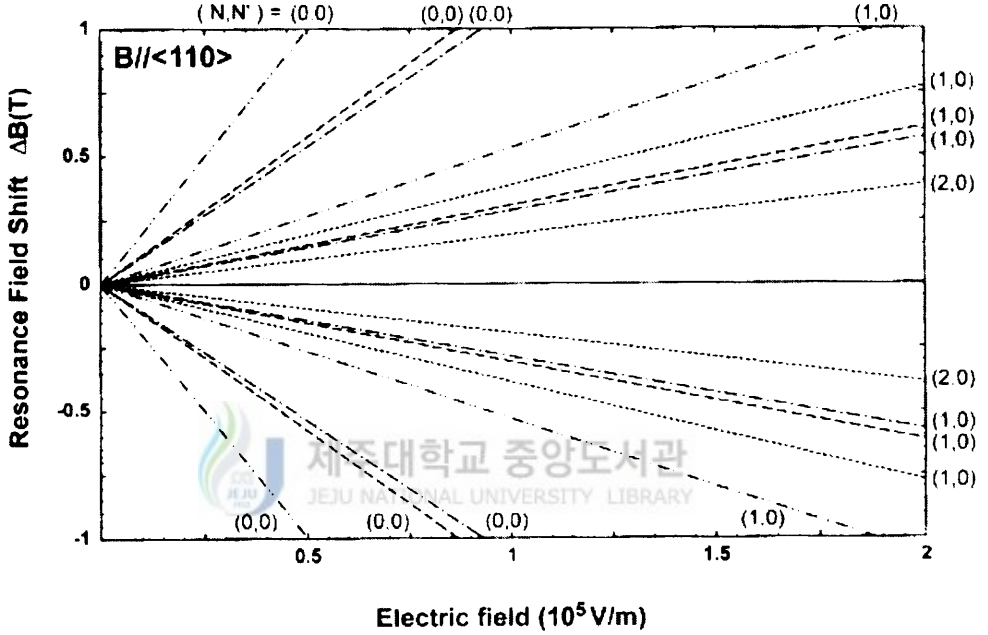


FIG. 2. Resonance field shift of n -Ge for $\mathbf{B} \parallel \langle 110 \rangle$. The quantum number of the Landau level is indicated for each line. The dashed-double dotted, dashed, dashed-dotted, and dotted line are for X_3 -point, X_1 -point, X_4 -point, and Γ -point, respectively. The dotted lines are for $m_s^* = 0.099m$ and all the lines except for the dotted lines are for $m_{si}^* = 0.099m$ and $m_{sf}^* = 0.36m$ corresponding to the initial and final state of transition, respectively.

Note that in the case of the limit $E \rightarrow 0$, our results occurring at \mathbf{X}_4 -points for $\mathbf{B} \parallel \langle 110 \rangle$ and $\mathbf{B} \parallel \langle 111 \rangle$ become the previous results [19] which are in good agreement with the experimental values of Eaves et al. [7] and Harper et al. [9] for the transverse configuration and with the experimental values of Yamada et al. [11]

and Futagawa et al. [12] for the longitudinal configuration.

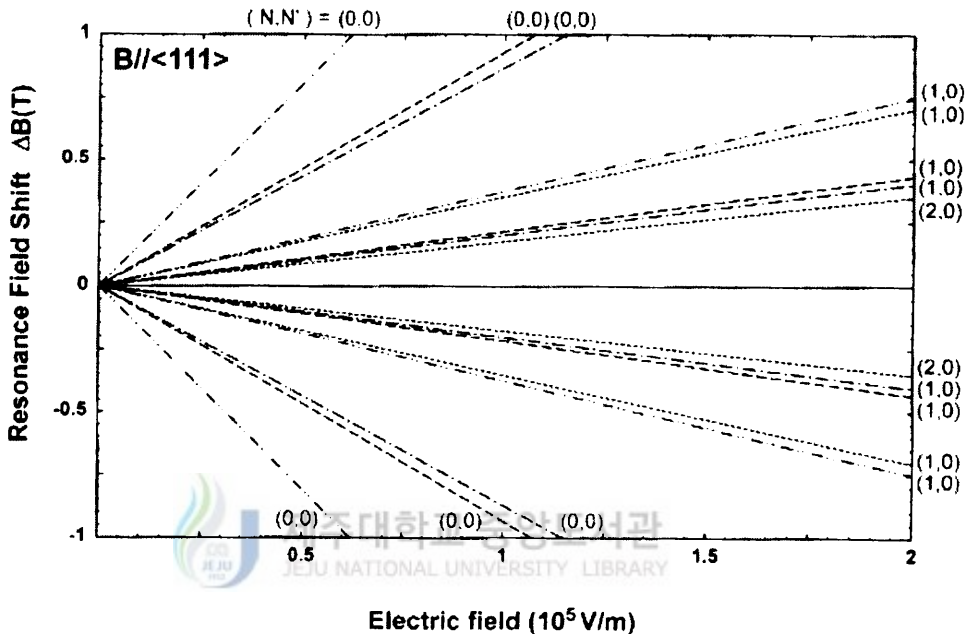


FIG. 3. Resonance field shift of n -Ge for $\mathbf{B} \parallel \langle 111 \rangle$. The quantum number of the Landau level is indicated for each line. The dashed-double dotted, dashed, dashed-dotted, and dotted line are for X_3 -point, X_1 -point, X_4 -point, and Γ -point, respectively. The dotted lines are for $m_s^* = 0.082m$ and all the lines except for the dotted lines are for $m_{s_i}^* = 0.082m$ and $m_{s_f}^* = 0.207m$ corresponding to the initial and final state of transition, respectively.

It is noted that our results for the relaxation rate and the dc magnetoconductivity are based on the following approximation as $y_{\lambda'}^s - y_{\lambda}^s \simeq \pm \bar{l}_{B_0}$ and $\delta(x+a) \approx \delta(x)$ (for $x \gg a$). Furthermore, any analytical expression for the integration over \mathbf{q} of Eq. (2.13) has not been made since we are interested only in the electric-field-induced MPR peak positions.

In conclusion, we have presented a theory of electric-field-induced MPR in n -Ge for the transverse configuration and obtained the MPR conditions given in Eqs. (2.21) and (2.24). As can be seen from Eqs. (2.21) and (2.24), MPR peak positions for the intervalley scattering by phonons strongly depend on the strength of the electric field, the possible phonon energy, the difference of Landau-level indices, and the magnetic field direction which leads to the difference in the effective mass between the initial and final states. According to the non-vertical transition due to the ICFE, double peaks take place. One of the peaks is shifted to the lower magnetic-field side and the other is shifted to the higher magnetic-field side as electric fields are increased and as the possible phonon energy and the difference of Landau-level indices are decreased.

We expect that our results help to understand qualitatively the physical characteristics of the electric-field-induced MPR effect in materials with the many-valley structure.

III. MAGNETOPHONON RESONANCE OF QUASI-TWO-DIMENSIONAL ELECTRONIC SYSTEM IN TILTED MAGNETIC FIELDS

Recently, MPR effects in low-dimensional electron gas (EG) systems have received much attention from both experimental and theoretical points of views [20–26] since the quantization of electron energies in low-dimensional EG systems under the presence of a high magnetic field is different from a bulk (3DEG) system. Moreover, a suitably directed magnetic field serves to add an extra confining potential to the initial electrostatic confinement and causes a dramatic change in the energy spectrum, leading to so-called hybrid magnetoelectric quantization. As a consequence, one would expect different behavior of the MPR effects in such system from the known MPR effects in 3DEG systems.

The purpose of the present work is to investigate the MPR effects in quasi-two-dimensional (Q2D) electron gas system to understand the qualitative behavior of the MPR effects in such low-dimensional system, based on the simple parabolic model for confinement potential. We shall derive the conductivity σ_{yy} for the Q2D electronic system subjected to a tilted magnetic field and obtain MPR conditions as a function of the field strength parameter (ω_1) of the parabolic potential, which characterize the strength of confinement of Q2D electronic system. We will examine how the MPR effects are affected by the constraint due to the directionality of applied magnetic fields. This gives an anomalous angular dependence of the field positions.

The rest of the chapter is organized as follows. In Sec. A, an exactly solvable model for Q2D electronic system is presented in an unified manner. In Sec. B, we

present the general formula of the transverse magnetoconductivity σ_{yy} for the Q2D system, which is closely related to the relaxation rate due to the collision process. In Sec. C, the relaxation rate, which is closely related to the MPR, is evaluated for bulk LO phonon scattering in the Q2D electronic system. The MPR conditions for the model system are given explicitly. Here, special attention is given to the behaviour of the MPR lineshape, such as the appearance of subsidiary MPR peaks and a reduction in MPR amplitude. Numerical results are given in Sec. D. In particular, the effects of tilted magnetic fields and the confining potential on the shift of MPR peaks are discussed.

A. Model for Q2D Electronic System in Tilted Magnetic Fields

We consider the transport of an electron gas in a quantum-well structure. The Q2D electron gas is assumed to be confined to the $x - y$ plane by an ideal parabolic potential $\frac{1}{2}m^*\omega_1^2z^2$. In the presence of a magnetic field, one-particle Hamiltonian (h_e) for such Q2D electrons is expressed in an unified manner by

$$h_e = \frac{1}{2m^*}(\mathbf{p}+e\mathbf{A})^2 + \frac{1}{2}m^*\omega_1^2z^2, \quad (3.1)$$

where \mathbf{A} is a vector potential accounting for a constant magnetic field $\mathbf{B} = \nabla \times \mathbf{A}$ and m^* is the effective mass. We shall consider the case where the magnetic field \mathbf{B} is applied in the transverse tilt direction to the plane of the system: $B = (B_x, 0, B_z) = (B \sin \theta, 0, B \cos \theta)$, with the Landau gauge $\mathbf{A} = (0, xB_z - zB_x, 0)$. Here the angle θ is measured from the z axis in the $x - z$ plane. Using the proper canonical transform, the one-particle Hamiltonian (3.1) for those confined (Q2D) electrons subjected to the transverse tilted magnetic field can be expressed in the new Cartesian coordinates as


$$h_e = \frac{1}{2m^*}P_X^2 + \frac{1}{2m^*}P_Z^2 + \frac{1}{2m^*}\omega_+^2 X^2 + \frac{1}{2m^*}\omega_-^2 Z^2, \quad (3.2)$$

where ω_+^2 and ω_-^2 are, respectively, given by

$$\omega_{\pm}^2 = \frac{1}{2}[\omega_c^2 + \omega_1^2 \pm \sqrt{(\omega_c^2 - \Omega_1^2)^2 + 4\omega_x^2\omega_z^2}] \quad (3.3)$$

with $\omega_x = eB_x/m^* = \omega_c \sin \theta$, $\omega_z = eB_z/m^* = \omega_c \cos \theta$, $\omega_c = eB/m^*$, and $\Omega_1^2 = \omega_1^2 + \omega_x^2$. The Hamiltonian (3.2) expressed in the new Cartesian coordinates is basically changed into the Hamiltonian for two independent 1D simple harmonic oscillators, one with the effective cyclotron frequency ω_+ in the X -direction and the other with the effective cyclotron frequency ω_- in the Z -direction.

The normalized eigenfunctions and eigenenergies of the one-electron Hamiltonian (3.2) are given by



$$\langle \mathbf{R} | \lambda \rangle \equiv \langle X, Y, Z | n, l, k_Y \rangle = \left(\frac{1}{L_Y}\right)^{1/2} \Psi_n(X) \Psi_l(Z) \exp(ik_Y Y) \quad (3.4)$$

and

$$E_{\lambda} \equiv E_{n,l}(k_Y) = (n + 1/2)\hbar\omega_+ + (l + 1/2)\hbar\omega_-, \quad (3.5)$$

respectively, where $n(= 0, 1, 2, \dots)$ and $l(= 0, 1, 2, \dots)$, respectively, denote the effective Landau (magnetic) level indices due to the tilted magnetic field, and $\Psi_n(X)$ and $\Psi_l(Z)$ denote 1D simple-harmonic-oscillator wave functions. The states of the Q2D system are specified by two Landau-level indices n and l , and the wave function $\exp(ik_Y Y)$ in Eq. (3.4) expresses a free motion in the y (i.e., Y) direction. The dimensions of the sample are assumed to be $V = L_x L_y L_z$. As shown in Eq. (3.5), the energy spectrum for the present Q2D system is *hybrid*-quantized due to the presence of the tilted magnetic field. The set of quantum numbers is designated by

(n, l, k_Y) . We note that the dimensional crossover can be seen in the energy spectrum by simply varying the confining potential parameter; $\omega_1 \rightarrow 0$ for the 3DEG system. It is interesting that the dependence of the energy spectrum in Eq. (3.5) on the confining potential parameter (ω_1), the direction (θ) and strength of the applied magnetic field (B) has an important effect on the MPR effects for the Q2D electronic system.

B. Magnetoconductivity Associated with Relaxation Rates

For the calculation of the transverse magnetoconductivity σ_{yy} for the model system described in the previous section, we apply the general expression for the complex nonlinear dc conductivity $\tilde{\sigma}_{kl}(E)$ ($k, l = x, y, z$) given in Ref. 4 to the quantum well modeled in the previous section by using the representation (3.4). Then, σ_{yy} can be easily obtained by the sum of the hopping parts due to the Landau-level indices n and l , which are

$$\begin{aligned} \sigma_{yy}^h = & \frac{e^2 \omega_z'^2 l_+^2}{V \hbar^2 \omega_+^3} \left(\frac{2\pi}{L_y} \right)^2 \sum_{n,l,k_Y} (n+1) [f(E_{nl}(k_Y)) - f(E_{n+1l}(k_Y))] \tilde{\Gamma}(n+1, l, k_Y; n, l, k_Y) \\ & + \frac{e^2 \omega_x'^2 l_-^2}{V \hbar^2 \omega_-^3} \left(\frac{2\pi}{L_y} \right)^2 \sum_{n,l,k_Y} (l+1) [f(E_{nl}(k_Y)) - f(E_{nl+1}(k_Y))] \tilde{\Gamma}(n, l+1, k_Y; n, l, k_Y) \end{aligned} \quad (3.6)$$

for $\hbar\omega_+, \hbar\omega_- \gg \tilde{\Gamma}$ and the shift zero in the spectral line shape, where V is the volume of the system, $l_{\pm} = \sqrt{\hbar/m^* \omega_{\pm}}$, $\omega'_z = \omega_z \cos \phi + \omega_x \sin \phi$, and $\omega'_x = \omega_x \cos \phi - \omega_z \sin \phi$. Also, $f(E_{nl}(k_Y))$ is a Fermi-Dirac distribution function associated with the eigenstate $|n, l, k_Y\rangle$ of Eq. (3.4) and the energy $E_{nl}(k_Y)$ of Eq. (3.5). The quantity $\tilde{\Gamma}$ given in Eq. (3.6), which appears in terms of the collision broadening due to the electron-phonon interaction, play the role of the relaxation rate in the

spectral line shape. Note that the first term of Eq. (3.6) is the magnetoconductivity given in terms of the electron hopping motion between the Landau level states n and $n + 1$, while the second term of Eq. (3.6) is the magnetoconductivity given in terms of the electron hopping motion between the Landau level states l and $l + 1$. To express the dc magnetoconductivity of Eq. (3.6) in simpler forms, we assume that the f 's in Eq. (3.6) are replaced by the Boltzmann distribution function for nondegenerate semiconductors, i.e., $f(E_{n,l}(k_Y)) \approx A \exp[\beta(E_F - E_{n,l}(k_Y))]$, where E_F denotes the Fermi energy. The normalization constant A is determined from $N_e = \sum_{n,l,k_Y} f(E_{n,l}(k_Y)) = (L_y/2\pi) \sum_{n,l} \int_{-m^*\omega_z L_x/2\hbar}^{m^*\omega_z L_x/2\hbar} f(E_{n,l}(k_Y)) dk_Y$, where the upper and the lower limits are obtained from the fact that the electrons should be within the crystal dimensions in the x direction, i.e., $-L_x/2 \leq x \leq L_x/2$, N_e is the total number of electrons in the system, and the constant is given by

$$A = N_e \frac{8\pi\hbar}{m^*\omega_z L_x L_y} \exp[-\beta E_F] \sinh(\beta\hbar\omega_+/2) \sinh(\beta\hbar\omega_-/2). \quad (3.7)$$

Then, we can further perform the sum over n (or l) (if n (or l) is large) by writing $\sum n \exp(-\alpha n) = -\frac{\partial}{\partial \alpha} \sum \exp(-\alpha n)$ and summing the geometric series. The transverse magnetoconductivity can be expressed by

$$\sigma_{yy}^h \approx \frac{n_e e^2}{m^*} \left(\frac{2\pi}{L_y} \right)^2 \left[\frac{\omega_z'^2}{\hbar\omega_+^4} \tilde{\Gamma}(n+1, l, k_{Y_2}; n, l, k_{Y_2}) + \frac{\omega_x'^2}{\hbar\omega_-^4} \tilde{\Gamma}(n, l+1, k_{Y_2}; n, l, k_{Y_2}) \right], \quad (3.8)$$

where the electron density is given as $n_e = N_e/V$. As shown in Eq. (3.8), the electronic transport properties (e.g., electronic relaxation processes, magnetophonon resonances, etc.) for the Q2D system can be studied by examining the behavior of $\tilde{\Gamma}$ as a function of the relevant physical parameters introduced in the theory. In the

next section, we shall analyze the relaxation rates in details in order to get insight into MPR effects in the Q2D electronic system.

C. Magnetophonon Resonances in Tilted Magnetic Fields

An analytical expression of the relaxation rate in the lowest-order approximation for the weak electron-phonon interaction and in the limit of weak electric fields can be evaluated from the general expression for the electric-field-dependent relaxation rate given by Eq. (4.39) of Ref. 4. Using the representation given by Eq. (3.4), the Q2D version of the relaxation rates associated with the electron hopping motion for optical phonon scattering can be expressed by

$$\begin{aligned} \tilde{\Gamma}(n+1, l, k_{Y_2}; n, l, k_{Y_2}) &\approx \tilde{\Gamma}(n, l+1, k_{Y_2}; n, l, k_{Y_2}) \\ &= \frac{4\pi D}{L_{Y_2}^3 l_+ l_-} \sum_{\pm} \left\{ \sum_{n' \neq n} \sum_{l'} + \sum_{l' \neq l} \sum_{n'} \right\} F_{nn'}(\Delta n) F_{ll'}(\Delta l) \\ &\quad \times (N_0 + \frac{1}{2} \pm \frac{1}{2}) \delta[(n-n')\hbar\omega_+ + (l-l')\hbar\omega_- \mp \hbar\omega_L], \end{aligned} \quad (3.9)$$

where D is constant, N_0 is the optical-phonon distribution function given by $n_{\vec{q}} = [\exp(\beta\hbar\omega_{\vec{q}}) - 1]^{-1}$ with $\omega_{\vec{q}} = \omega_L$, n' and l' indicate the intermediate localized Landau level indices, and

$$\begin{aligned} F_{n'n}(\Delta n) &= \frac{n_{<}! (1 + \Delta n)_{n_{<}} (2\Delta n + \frac{3}{2})_{n_{<}} \Gamma(\Delta n + \frac{1}{2})}{n_{>}! (n_{<}!)^2} \\ &\quad \times {}_3\Phi_2(-n_{<}, \Delta n + \frac{1}{2}, \frac{1}{2}; \Delta n + 1, \frac{1}{2} - n_{<}; 1). \end{aligned} \quad (3.10)$$

Here $n_{<} = \min\{n, n'\}$, $n_{>} = \max\{n, n'\}$, the Pochhammer's symbol $(a)_n$ is defined by $(a)_n = a(a+1)\cdots(a+n-1) = \Gamma(a+n)/\Gamma(a)$, and ${}_3\Phi_2(a, b, c; d, e; x)$ is the hypergeometric function [15]. The δ functions in Eq. (3.9) express the law of energy conservation in one-phonon collision (absorption and emission) processes.

The strict energy-conserving δ functions in Eq. (3.9) imply that when the electron undergoes a collision by absorbing energy from the field, its energy can only change by an amount equal to the energy of a phonon involved in the transitions. This in fact leads to MPR effects due to the Landau levels. We see from Eq. (3.9) that the relaxation rates shows the resonant behaviors: magnetophonon resonances at $P\hbar\omega_+ = \hbar\omega_L$ and $P\hbar\omega_+ = \hbar\omega_L \mp \Delta l\hbar\omega_-$ (P is an integer), which is due to the Landau-level index n , and at $P\hbar\omega_- = \hbar\omega_L$ and $P\hbar\omega_- = \hbar\omega_L \mp \Delta n\hbar\omega_+$, which is due to the Landau-level index l , where Δl and Δn are the difference of Landau-level index corresponding to the case where the virtual nonresonant transition takes place. Thus, it is shown that additional MPR conditions (subsidiary peaks) appear at $P\hbar\omega_+ = \hbar\omega_L \mp \Delta l\hbar\omega_-$ (or $P\hbar\omega_- = \hbar\omega_L \mp \Delta n\hbar\omega_+$) on both side of the MPR peaks at $P\hbar\omega_+ = \hbar\omega_L$ (or $P\hbar\omega_- = \hbar\omega_L$). The origin of the appearance of the subsidiary peaks in the Q2DEG system is mainly due to the confinement to the $x - y$ plane by the parabolic potential. It should be noted that the relaxation rate for optical phonon scattering diverges whenever the above conditions are satisfied. These divergences may be removed by including higher-order electron-phonon scattering terms or by inclusion of the fluctuation effects of the center-of-mass [27]. The simplest way to avoid the divergences is to replace each δ function in Eq. (3.9) by Lorentzians with a width parameter γ . Employing this collision-broadening model [23], setting $n - n', l - l' = P$ in the emission term and $n - n', l - l' = -P$ in the absorption term as some author did [20,23], applying Poisson's summation formula [28] for the \sum_p in Eq. (3.9), and taking into account the following property [15]:

$$\Psi(a, b) = 1 + 2 \sum_{s=1}^{\infty} e^{-2\pi sa} \cos(2\pi sb) = \frac{\sinh(2\pi a)}{\cosh(2\pi a) - \cos(2\pi b)}, (a > 0) \quad (3.11)$$

we then obtain

$$\begin{aligned}
\tilde{\Gamma}(n+1, l, k_{Y_2}; n, l, k_{Y_2}) &\approx \tilde{\Gamma}(n, l+1, k_{Y_2}; n, l, k_{Y_2}) \approx \frac{4\pi D}{\hbar L_y^3 l_+ l_-} \sum_{\pm} (N_0 + \frac{1}{2} \pm \frac{1}{2}) \\
&\times \left\{ \frac{1}{\omega_+} \sum_{l'} F_{l'l}(\Delta l) F_{nn'}[(\omega_L \mp \Delta l \omega_-)/\omega_+] \right. \\
&\times \Psi(\gamma/\hbar\omega_+, \frac{\varpi_L \mp \Delta l \omega_-}{\omega_+}) \\
&+ \frac{1}{\omega_-} \sum_{n'} F_{nn'}(\Delta n) F_{l'l}[(\omega_L \mp \Delta n \omega_+)/\omega_-] \\
&\left. \times \Psi(\gamma'/\hbar\omega_-, \frac{\varpi_L \mp \Delta n \omega_+}{\omega_-}) \right\} \tag{3.12}
\end{aligned}$$

for the MPR effects due to the Landau-level indices n and l . For simplicity, we assumed that $\gamma_i = \gamma$ ($i = 1, 2,$ and 3) for the collision damping terms in the quantities $\Psi(\gamma/\hbar\omega_+, \varpi_L/\omega_+)$ and $\Psi(\gamma/\hbar\omega_+, (\varpi_L \pm \Delta l \omega_-)/\omega_+)$ of Eq. (3.12) and $\gamma_i = \gamma'$ ($i = 4, 5,$ and 6) for the collision damping terms in the quantities $\Psi(\gamma/\hbar\omega_-, \varpi_L/\omega_-)$ and $\Psi(\gamma/\hbar\omega_-, (\varpi_L \pm \Delta n \omega_+)/\omega_-)$ of Eq. (3.12). Equation (3.12) gives a general description of magnetophonon oscillations in the Q2D quantum-well structure for the MPR effects due to the Landau-level indices n and l . For the MPR effect due to the Landau-level index n , Eq. (3.12) shows the oscillation under the periodic condition of $P\omega_+ = \omega_L$ and exhibits additional complexity of oscillations with the subsidiary (MPR) peaks appearing at $P\omega_+ = \omega_L \mp \Delta l \omega_-$. It is shown that the oscillation in the relaxation rate is damped by the direction and strength of the magnetic field and the confinement frequency (ω_1) since these parameters give a direct influence on the effect of collision damping. Similarly, the relaxation rates of Eq. (3.12) associated with the MPR effect due to the Landau-level index l have another oscillatory period $P\omega_- = \omega_L$ and the subsidiary (MPR) peaks appear at $P\omega_- = \omega_L \mp \Delta n \omega_+$. These MPR effects of Eq. (3.12) take place in the case where magnetic field given in the tilt direction is applied to the Q2D quantum-well system. If the direction of magnetic field is taken in a specific direction of the system ($\theta = 0^\circ$

or 90°), these effects arise from the Landau-level index n or l only.

D. Numerical Results and Discussion

In this section, we investigate the physical characteristics of the MPR effects from the magnetoconductivity formula associated with MPR obtained for the Q2D electronic system based on the model described in Sec. A. By making use of the MPR conditions due to the Landau-level indices n and l at $P\hbar\omega_+ = \hbar\omega_L$ and $P\hbar\omega_+ = \hbar\omega_L \mp \Delta l\hbar\omega_-$, and at $P\hbar\omega_- = \hbar\omega_L$ and $P\hbar\omega_- = \hbar\omega_L \mp \Delta n\hbar\omega_+$, the resonance peak positions in the Q2D system are plotted in Figs. 4 and 5 as a function of tilt angles θ of the transverse tilted magnetic field $\mathbf{B} = (B \sin \theta, 0, B \cos \theta)$ applied to the electronic plane for confinement frequency ω_1 in the z direction, where the optical phonon energy $\hbar\omega_L$ was taken as 36.6 meV and three different confinement frequencies ($0.5\omega_c$, ω_c , and $5\omega_c$) were taken into account, in order to examine the characteristics of the MPR effects according to the confinement in the z direction. For ease of discussion, we considered the case where the MPR arises from the transitions between two Landau levels ($P = 1$), together with the nonresonant virtual transition between two Landau levels (Δl or $\Delta n = 1$). As shown in Fig. 4, we can see the following features for the Q2D system: (i) there are three resonance peaks in the σ_{yy} , which arise from the conditions $\omega_+ = \omega_L$ and $\omega_+ = \omega_L \pm \omega_-$; (ii) when the confinement in the z direction is strong, the resonance magnetic fields appear in the lower magnetic-field side and their angle dependence becomes small, and (iii) the peak positions obtained from the conditions $\omega_+ = \omega_L$ and $\omega_+ = \omega_L + \omega_-$ are shifted to the lower field side whereas the peak positions obtained from the condition $\omega_+ = \omega_L - \omega_-$ are shifted to the higher field side, as

the tilt angle θ of the applied magnetic field is increased.

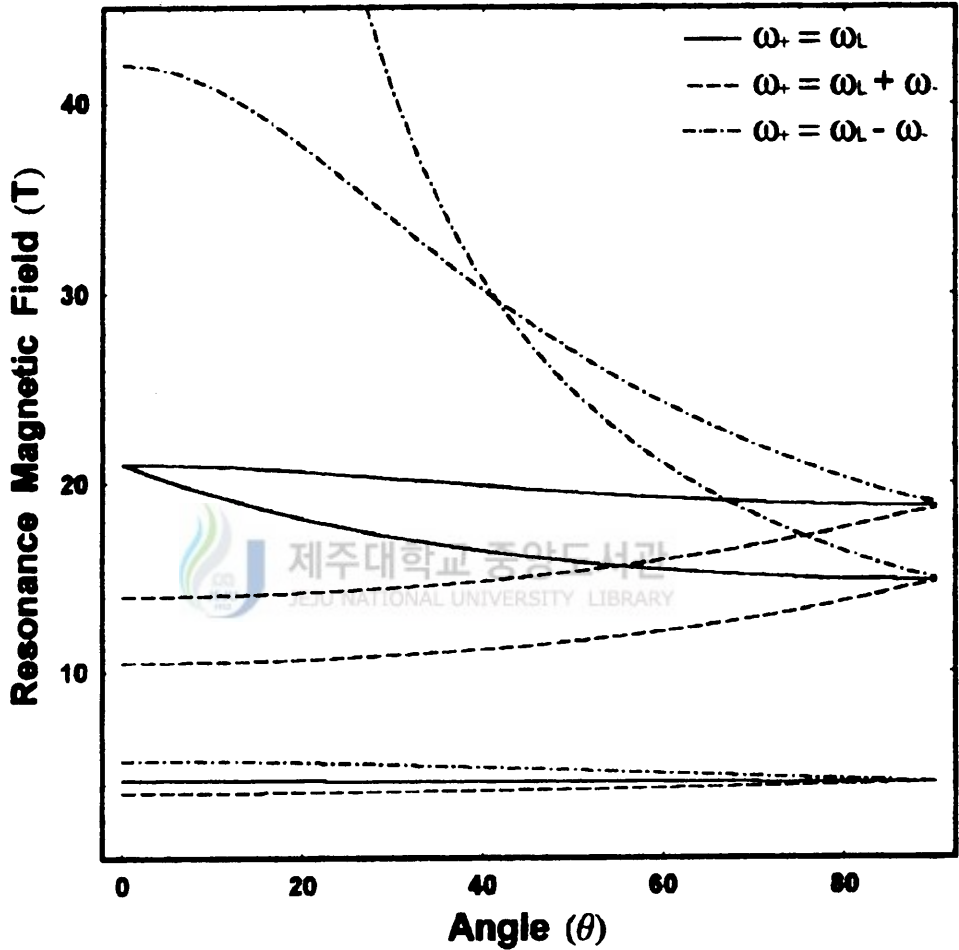


FIG. 4. Tilt angle dependence of the resonance magnetic field for three different confinement frequencies in the z direction $\omega_1 = 5\omega_c, \omega_c, 0.5\omega_c$ (from bottom on the right-hand side of the figure to top). The solid lines, the dashed-dotted lines, and the dashed lines are for the MPR conditions $\omega_+ = \omega_L, \omega_+ = \omega_L + \omega_-,$ and $\omega_+ = \omega_L - \omega_-,$ respectively.

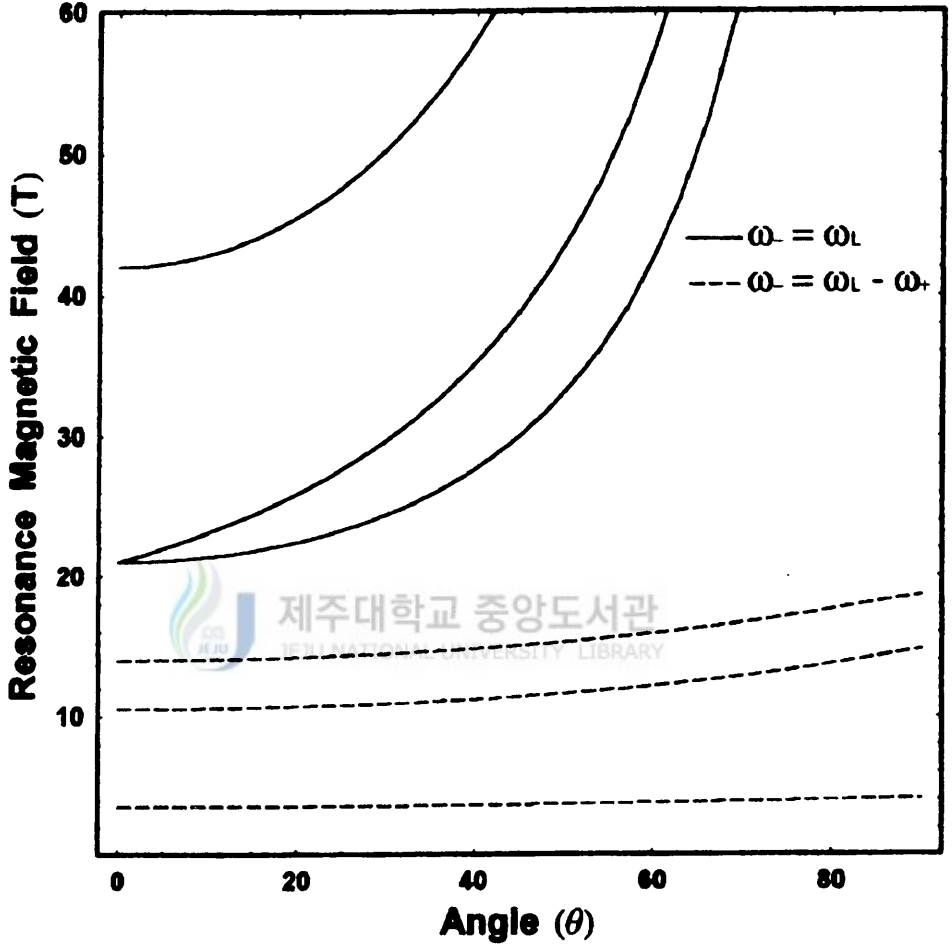


FIG. 5. Tilt angle dependence of the resonance magnetic field for three different confinement frequencies in the z direction $\omega_1=5\omega_c$, ω_c , $0.5\omega_c$ (from bottom to top). The solid lines and the dashed lines are for the MPR conditions $\omega_- = \omega_L$ and $\omega_- = \omega_L - \omega_+$, respectively.

We can also see the following features from Fig. 5: (i) there are two resonance peaks in the σ_{yy} , which arise from the conditions $\omega_- = \omega_L$ and $\omega_- = \omega_L - \omega_+$; and (ii) the resonance magnetic fields increase with the increase of the tilt angle θ .

It is interesting to note from Figs. 4 and 5 that the MPR peak positions arising from the conditions $\omega_+ = \omega_L$ shift to the lower B side whereas those arising from the conditions $\omega_- = \omega_L$ shift to the higher B side when the tilt angle of applied magnetic fields is increased.

According to the experimental results of Brumell et al. [21] for Q2D electronic systems, all of the MPR peaks shift to the higher B side when the tilt angle of applied magnetic fields is increased. Our theoretical results obtained from the conditions $\omega_- = \omega_L$, $\omega_- = \omega_L - \omega_+$, and $\omega_+ = \omega_L - \omega_-$ for the Q2D case agree qualitatively with their experimental results. However, our theoretical results obtained from the conditions $\omega_+ = \omega_L$ and $\omega_+ = \omega_L + \omega_-$ does not agree with their experimental results. This disagreement may be due to the fact that their experiment is performed under the magnetic field up to 10 tesla whereas our calculations are carried out for the magnetic fields in the region more than 15 tesla, taking into account the effective Landau and subband states, $n = 0, 1$ and $l = 0, 1$ only. If we take into account the electronic transitions up to the second excited levels ($P \geq 2$) and obtain the MPR conditions valid under the magnetic field up to 10 tesla, we might expect the present theory to reproduce their experimental results qualitatively. It should be noted that our theoretical results are based on a model of parabolic confining potential. For usual heterostructures it is well known that the confinement potential in the z -direction is far away from being parabolic and is often approximated by a triangular potential [23,25]. For direct comparison with experiments, realistic modeling with the correct confinement potential should be required. We believe however that utilizing a model with a parabolic confinement is good enough to extract essential physics of MPR effects in Q2D electronic systems in tilted magnetic fields. In other words, energy spectrum obtained from quasi-triangular potential

and parabolic potential does not alter the essential physics of MPR effects in Q2D electronic systems as far as the fundamental ($P = 1$) MPR, which we considered here, is concerned.

Despite the above shortcomings of the theory, we believe that the simple model we present captures qualitatively the essential physics on MPR in Q2D electronic system brought about by the electron confinement due to the electrostatic potentials and the magnetic confinement by tilting a magnetic field. We hope that new experiments will test the validity of our prediction.



IV. MAGNETOPHONON AND ELECTROPHONON RESONANCES IN QUANTUM WIRES

Magnetophonon resonances and electrophonon resonances in low-dimensional electron gas systems have generated considerable interest in recent years. Many studies have been made on these effects in 2DEG systems [1,3,14,20,22,29–34]. However, less work has been done on these effects of a Q1DEG [23,24,35]. It is well-known [1,3] that MPR effect arises from resonant scattering of the electrons in Landau levels by LO phonons whenever the phonon energy is equal to an integral multiple of energy separations between two Landau levels whereas EPR effect occurs when the energy difference of two electric subbands ΔE_{mn} (m and n are subband indices) equals the energy of a LO phonon $\hbar\omega_L$. These resonance effects in low-dimensional electron gas have shown that the type of material used to confine the electrons and the form of the confinement potential significantly influence the interactions between the electrons and optical phonons.

Vasilopoulos et al. [23] studied MPR effects in quantum wires assuming a parabolic confinement potential of frequency Ω , based on the Kubo formula [36] and the quantum Boltzmann equation [30], and their calculations revealed that the ordinary resonance condition $\omega_L = P\omega_c$ is modified to $\omega_L = P\tilde{\omega}_c$, where P is an integer, ω_L and ω_c are the LO phonon frequency and cyclotron frequency, respectively, and $\tilde{\omega}_c$ is the renormalized cyclotron frequency given by $\tilde{\omega}_c = (\omega_c^2 + \Omega^2)^{1/2}$. Mori et al. [24] presented a theory of MPR for the same model as treated by Vasilopoulos et al. [23], by utilizing the Kubo formula and the Green's function method [37]. A numerical analysis with respect to the magnetoconductivity has been performed for weak and strong confinement potentials by introducing the current density operator

due to the electron-phonon interaction and confinement potential. Recently, Ryu et al. [35] have presented a theory of MPR for the same model as treated by Vasilopoulos et al. [23], by taking the linear response limit of nonlinear response theory [4], in order to investigate analytically the MPR effects in quantum wires. It should be pointed out that they assumed that only the lowest subband level formed in the heterostructures is occupied. This assumption leads to neglect of effects arising from a consequence of occupation of several electric subbands such as EPR effect, the splitting of MPR peak positions, and the shift of MPR peaks. The purpose of the present paper is to study MPR and EPR effects of a Q1DEG in quantum wires, where electric subbands are considered.

A. Model for Quantum Wires

We consider a simple model for a quantum wire, in which a two-dimensional electron gas formed in heterostructures is confined by narrow gates or split gates, and electrons are free along only one direction. We assume that a heterointerface is normal to the z axis, and the confinement in the y direction is characterized by a parabolic potential of frequency Ω_y . For the confinement potentials along the z axis, we take the following potential wells: (1) the parabolic well and (2) the square well, which both have the advantage that all subbands can be included in the calculation; and (3) the triangular well, which is often used to model heterostructures. Applying a static magnetic field $\vec{B}(\parallel \hat{z})$ to the wire and considering the effective-mass approximation for conduction electrons confined in the quantum wire, the one-particle Hamiltonian (h_e) for such electrons together with its normalized eigenfunctions ($|\lambda\rangle$) and eigenvalues (E_λ), in the Landau gauge of vector potential

$\vec{A} = (-By, 0, 0)$, are respectively, given by

$$h_e = (\vec{p} - e\vec{A})^2/2m^* + m^*\Omega_y^2 y^2/2 + h(z), \quad (4.1)$$

$$|\lambda \rangle \equiv |N, n, k_x \rangle = \phi_N(y - y_\lambda) \exp(ik_x x) \Psi_n(z) / \sqrt{L_x}, \quad (4.2)$$

$$E_\lambda \equiv E_{N,n,k_x} = (N + 1/2)\hbar\tilde{\omega}_c + \hbar^2 k_x^2 / 2\tilde{m} + \varepsilon_n, \quad (4.3)$$

$$\phi_N(y) = (1/2^N \pi^{1/2} \tilde{l}_B N!)^{1/2} \exp(-y^2/2\tilde{l}_B^2) H_N(y/\tilde{l}_B), \quad (4.4)$$

where \vec{p} is the momentum operator of a conduction electron, $N (= 0, 1, 2, \dots)$ and n denote the Landau-level index and the subband-level index, respectively, and $\tilde{\omega}_c = (\omega_c^2 + \Omega_y^2)^{1/2}$ and $\tilde{m} = m^* \tilde{\omega}_c^2 / \Omega_y^2$ are the renormalized cyclotron frequency with respect to the cyclotron frequency $\omega_c = eB/m^*$ and the renormalized mass with respect to the effective mass m^* associated with the characteristic frequency of the confinement potential Ω_y , respectively. Also $H_N(x)$ are the Hermite polynomials and $\phi_N(y - y_\lambda)$ represents harmonic-oscillator wave functions, centered at $y = y_\lambda = -\tilde{b}\tilde{l}_B^2 k_x$. Here k_x is the wave vector in the x direction, $\tilde{b} = \omega_c/\tilde{\omega}_c$, and $\tilde{l}_B = (\hbar/m^* \tilde{\omega}_c)^{1/2}$ is the effective radius of the ground-state electron orbit in the (x, y) plane. The dimensions of the sample are assumed to be $V = L_x L_y L_z$. In zero magnetic-field case, the Landau levels become the subband levels in the y direction, the renormalized cyclotron frequency $\tilde{\omega}_c$ and the renormalized mass \tilde{m} in Eq. (4.3) reduce to the confining frequency Ω_y and the effective mass m^* , respectively, and the center of harmonic-oscillator wave functions in Eq. (4.2) becomes zero.

For a parabolic well given by $h(z) = m^* \Omega_z^2 z^2 / 2$ with the the characteristic frequency of the confinement potential Ω_z , the eigenfunctions $\Psi_n(z)$ and the corresponding eigenvalues ε_n are, respectively, given by

$$\Psi_n(z) = (1/2^n \pi^{1/2} l_B n!)^{1/2} \exp(-z^2/2l_B^2) H_n(z/l_B), \quad (4.5)$$

$$\varepsilon_n = (n + \frac{1}{2}) \hbar \Omega_z, \quad n = 0, 1, 2, \dots, \quad (4.6)$$

where $l_B = (\hbar/m^* \Omega_z)^{1/2}$.

For a square well of infinite height, the eigenfunctions and eigenvalues, respectively, are known to be

$$\Psi_n(z) = \sqrt{\frac{2}{L_z}} \sin\left(\frac{n\pi}{L_z} z\right), \quad (4.7)$$

$$\varepsilon_n = n^2 \varepsilon_0, \quad n = 1, 2, 3, \dots, \quad (4.8)$$

where $\varepsilon_0 = \hbar^2 \pi^2 / 2m^* L_z^2$.

For the half-triangular-well case given by $h(z) = eF_s z$ ($z > 0$), ∞ ($z < 0$), the eigenfunctions are given by *Airy functions* [38] as

$$\Psi_n(z) = Ai \left[\left(\frac{2m^* e F_s}{\hbar^2} \right)^{1/3} \left(z - \frac{\varepsilon_n}{e F_s} \right) \right], \quad (4-9)$$

where the eigenvalues are approximately given by

$$\varepsilon_n = \left(\frac{\hbar^2 e^2 F_s^2}{2m^*} \right)^{1/3} \left[3\pi \left(n + \frac{3}{4} \right) / 2 \right]^{2/3}, \quad n = 0, 1, 2, \dots \quad (4.10)$$

Here F_s is an applied bias field in the z direction of the heterostructure. In practical calculation one is often forced to approximate Eq. (4.9) through variational wave functions in order to keep the numerical calculations tractable. For the lowest subband ($n = 0$) and the first excited subband ($n = 1$), the wave functions [39,40] are, respectively,

$$\Psi_0(z) = (b_0^3/2)^{1/2} z \exp(-b_0 z/2), \quad (4.11)$$

and

$$\Psi_1(z) = A(2/b_0^3)^{1/2} z(1 - Bz) \exp(-b_1 z/2) \quad (4.12)$$

with $b_0 = 2(3eF_s m^* / 2\hbar)^{1/3}$, $b_1 \simeq 0.754b_0$, $A \simeq 0.47b_0^3$, and $B \simeq 0.292b_0$.

B. Magnetophonon and Electrophonon Resonances

The transverse magnetoconductivity σ_{xx} for Q1D version can be evaluated from the linear-response limit with respect to Eq. (4.38) of Ref. 4 given in the nonlinear-response theory, which is expressed by the sum of the hopping part σ_{xx}^h and the nonhopping part σ_{xx}^{nh} as [35]

$$\sigma_{xx}^h \approx (e^2 \tilde{b}^2 \tilde{l}_B^2 N_s^{1D} / \hbar^2 \tilde{\omega}_c V) \tilde{\Gamma}_{0\lambda+1\lambda}, \quad (4.13)$$

$$\sigma_{xx}^{nh} \approx (\hbar e^2 \tilde{\omega}_c^2 N_s^{1D} / m^* \Omega_y^2 V) [\tilde{\Gamma}_{0\lambda\lambda}]^{-1}, \quad (4.14)$$

where $N_s^{1D} = \sqrt{\tilde{m} L_x^2 / 8\pi \hbar^2 \beta} \sum_n \exp[\beta(E_F - \varepsilon_n)] / \sinh(\beta \hbar \tilde{\omega}_c / 2)$ with E_F being the Fermi energy, $\beta = 1/k_B T$ with k_B being Boltzmann's constant, $X_{\lambda\lambda'} \equiv \langle \lambda | X | \lambda' \rangle$ for any operator X , and $\tilde{\Gamma}_{0\lambda_2\lambda_1}$ is the relaxation rate associated with the states λ_1 and λ_2 . To obtain the above equations we have performed the sum over the λ state with the use of Eq. (4.2). Using Eqs. (4.2) and (4.3), the Q1D version of the relaxation rate for the weak-coupling case of an electron-phonon system, associated with the electronic transition between the state $|\lambda_1\rangle$ and $|\lambda_2\rangle$, is given, from Eq. (16) of Ref. [35], as

$$\begin{aligned} \tilde{\Gamma}_{0\lambda_2\lambda_1} = & \pi(N_0 + 1/2 \pm 1/2) \sum_{\vec{q}} |C(q)|^2 \left\{ \sum_{\lambda' \neq \lambda_2} |J_{N_2 N'}(u)|^2 |J_{n n'}(q_z)|^2 \right. \\ & \times \delta[(N_1 - N') \hbar \tilde{\omega}_c + (\varepsilon_{n_1} - \varepsilon_{n'}) + S_1^\mp(q_x) \mp \hbar \omega_L] \\ & + \sum_{\lambda' \neq \lambda_1} |J_{N' N_1}(u)|^2 |J_{n n'}(q_z)|^2 \delta[(N' - N_2) \hbar \tilde{\omega}_c + (\varepsilon_{n'} - \varepsilon_{n_2}) + S_2^\mp(q_x) \pm \hbar \omega_L] \left. \right\}, \end{aligned} \quad (4.15)$$

where we have assumed that the phonons are dispersionless (i.e., $\hbar \omega_{\vec{q}} \approx \hbar \omega_L \approx \text{constant}$, where ω_L is the LO-phonon frequency) and the system is of bulk (i.e.,

three-dimensional). $C(q)$ is the interaction potential for LO-phonon scattering, N' indicates intermediate localized Landau states, and N_0 is the LO-phonon distribution function given by $N_{\vec{q}} = [\exp(\beta\hbar\omega_{\vec{q}}) - 1]^{-1}$ with $\omega_{\vec{q}} = \omega_L$. In Eq. (4.15)

$$S_1^\mp(q_x) = \{\hbar^2 k_{1x}^2 - \hbar^2(k_{2x} \mp q_x)^2\}/2\tilde{m}, \quad (4.16)$$

$$S_2^\mp(q_x) = \{\hbar^2(k_{1x} \mp q_x)^2 - \hbar^2 k_{2x}^2\}/2\tilde{m}, \quad (4.17)$$

$$|J_{nn'}(\pm q_z)|^2 = \left| \int_{-\infty}^{\infty} \Psi_n^*(z) \exp(\pm i q_z z) \Psi_{n'}(z) dz \right|^2, \quad (4.18)$$

$$|J_{NN'}(u)|^2 = \frac{N_n!}{N_m!} e^{-u} u^{N_m - N_n} [L_{N_n}^{N_m - N_n}(u)]^2 \quad (4.19)$$

with $N_n = \min\{N, N'\}$, $N_m = \max\{N, N'\}$, $u = \tilde{l}_B^2(\tilde{b}^2 q_x^2 + q_y^2)/2$, and $L_N^M(u)$ being an associated Laguerre polynomial [15]. The energy-conserving δ functions in Eq. (4.15) imply that when the electron undergoes a collision by absorbing energy from the field, its energy can change only by an amount equal to the energy of a phonon involved in the transition. This in fact leads to the MPR and/or EPR effects, for which $\hbar\tilde{\omega}_c$ and $\Delta\varepsilon_n \gg \tilde{\Gamma}_0$. Proceeding as in Vasilopoulos et al. [23] with respect to \vec{q} in the δ functions in Eq. (4.15), making an approximation $N' \pm 1 \approx N'$ for very large N' , the relaxation rates $\tilde{\Gamma}_{0\lambda+1\lambda}$ and $\tilde{\Gamma}_{0\lambda\lambda}$ can be written in a simple form:

$$\begin{aligned} \tilde{\Gamma}_{0\lambda+1,\lambda} &\approx \tilde{\Gamma}_{0\lambda,\lambda} \approx 2\pi(N_0 + 1/2 \pm 1/2) \sum_{\vec{q}} |C(q)|^2 \\ &\times \sum_{\lambda' \neq \lambda} |J_{NN'}(u)|^2 |J_{nn'}(q_z)|^2 \delta[(N' - N)\hbar\tilde{\omega}_c + \hbar\omega_{n'n} \pm \hbar\omega_L], \end{aligned} \quad (4.20)$$

where $\omega_{n'n} = (\varepsilon_{n'} - \varepsilon_n)/\hbar$ and the selection rule $\lambda' \neq \lambda$ in the summation of Eq. (4.20) means $(N', n') \neq (N, n)$, which contains the following conditions: (1) $N' \neq N$ and $n' = n$, (2) $N' = N$ and $n' \neq n$, and (3) $N' \neq N$ and $n' \neq n$. From

these conditions, we can expect three possible transitions in quantum wires: (1) the transition due to the Landau levels for the y direction, (2) the transition due to the subband levels for the z direction, and (3) the transition due to both the Landau levels for the y direction and the subband levels for the z direction.

Setting $N' - N = -P$ in the emission term and $N' - N = P$ in the absorption term [23] and considering Eqs. (4.13), (4.14), and (4.20), we see from the above condition that the transverse magnetoconductivity shows resonant behaviors: MPR at $P\tilde{\omega}_c = \omega_L$ and at $P\tilde{\omega}_c = \omega_L^\pm$ (P is an integer) with $\omega_L^\pm = \omega_L \pm \omega_{n'n}$. Those resonances involving the terms $\omega_{n'n}$ reflect the subband structure in the z direction and the terms $\omega_{n'n}$ give rise to the splitting of the MPR effects whenever the interelectric virtual (nonresonant) subband transitions take place for a relevant energy separation between two subbands for the z direction. The MPR condition at $P\tilde{\omega}_c = \omega_L$ is identical with those indicated by Vasilopoulos et al. [23]. Furthermore, we see from the above condition that the conductivity shows another resonant behaviors: EPR due to the subband in the z direction at $\omega_{n'n} = \omega_L$. Note that, in zero magnetic-field case, the relaxation rate (and hence the electric conductivity) obtained by replacing $\tilde{\omega}_c$ in Eq. (4.20) by Ω_y shows resonant behaviors: EPR due to the subband level in the y direction at $P\Omega_y = \omega_L$ and at $P\Omega_y = \omega_L^\pm$ (P is an integer), and EPR due to the subband in the z direction at $\omega_{n'n} = \omega_L$ and at $\omega_{n'n} = \omega_L \pm P\Omega_y$. In this case, we also see that the subband level for the y or z direction leads to the splitting of EPR whenever virtual interelectric subband transitions take place.

Employing the collision-broadening [14,23] model and applying Poisson's summation formula [28] for the \sum_P in Eq. (4.20) we then obtain the relaxation rate for three different confinement potentials as

$$\begin{aligned}\tilde{\Gamma}_{0\lambda+1,\lambda} &\approx \tilde{\Gamma}_{0\lambda,\lambda} \approx \sqrt{\frac{2\pi\tilde{m}L_x^2}{\beta\hbar^3\tilde{\omega}_c}}(N_0 + 1/2 \pm 1/2) \sum_{n'} \text{Re}\{F_{nn'}(\frac{i\gamma_1}{\hbar\tilde{\omega}_c} + \frac{\omega_L^\pm}{\tilde{\omega}_c})\} \Psi(\frac{\gamma_1}{\hbar\tilde{\omega}_c}, \frac{\omega_L^\pm}{\tilde{\omega}_c}) \\ &+ \sqrt{\frac{2\pi\tilde{m}L_x^2}{\beta\hbar^2}}(2N_0 + 1)S^{osc}(n; n'),\end{aligned}\quad (4.21)$$

where

$$S^{osc}(n; n') = \begin{cases} \frac{1}{\hbar\Omega_z} \text{Re}\{F_q(N, N'; \frac{i\gamma_2}{\hbar\Omega_z} + \frac{\omega_L}{\Omega_z})\} \Psi(\frac{\gamma_2}{\hbar\Omega_z}, \frac{\omega_L}{\Omega_z}) & \text{(parabolic well)} \\ \frac{1}{2\varepsilon_0(n+x_1)} \text{Re}\{F_q(N, N'; \frac{i\gamma_3}{\varepsilon_0} + x_1)\} \Psi(\frac{\gamma_3}{\varepsilon_0}, x_1) & \text{(square well)} \\ \frac{3(x_2+n+\frac{3}{4})}{2F_s} \text{Re}\{F_q(N, N'; \frac{i\gamma_4}{F_s} + x_2)\} \Psi(\frac{\gamma_4}{F_s}, x_2), & \text{(triangular well)} \end{cases}\quad (4.22)$$

$$F_{nn'}(P) \equiv \sum_{\bar{q}} |C(q)|^2 |J_{NN+P}(u)|^2 |J_{nn'}(q_z)|^2, \quad (4.23)$$

$$F_{NN}(n') \equiv \sum_{\bar{q}} |C(q)|^2 |J_{NN}(u)|^2 |J_{nn'}(q_z)|^2, \quad (4.24)$$

$$\Psi(a, b) = 1 + 2 \sum_{s=1}^{\infty} e^{-2\pi sa} \cos(2\pi sb) = \frac{\sinh(2\pi a)}{\cosh(2\pi a) - \cos(2\pi b)}, \quad (a > 0) \quad (4.25)$$

with $x_1 = \sqrt{n^2 + \omega_L/\varepsilon_0} - n$, $x_2 = \sqrt{\{(n + 3/4)^{2/3} + \omega_L/F_s\}^3} - (n + 3/4)$, and $\gamma_i (i = 1, 2, 3, 4)$ being the damping parameters.

C. Numerical Results

To visualize the series of resonance positions associated with MPR and EPR effects in the quantum wires, we showed the plots in Figs. 6, 7 and 8, where the optical phonon energy has been taken as $\hbar\omega_L = 36.6\text{meV}$ for GaAs.

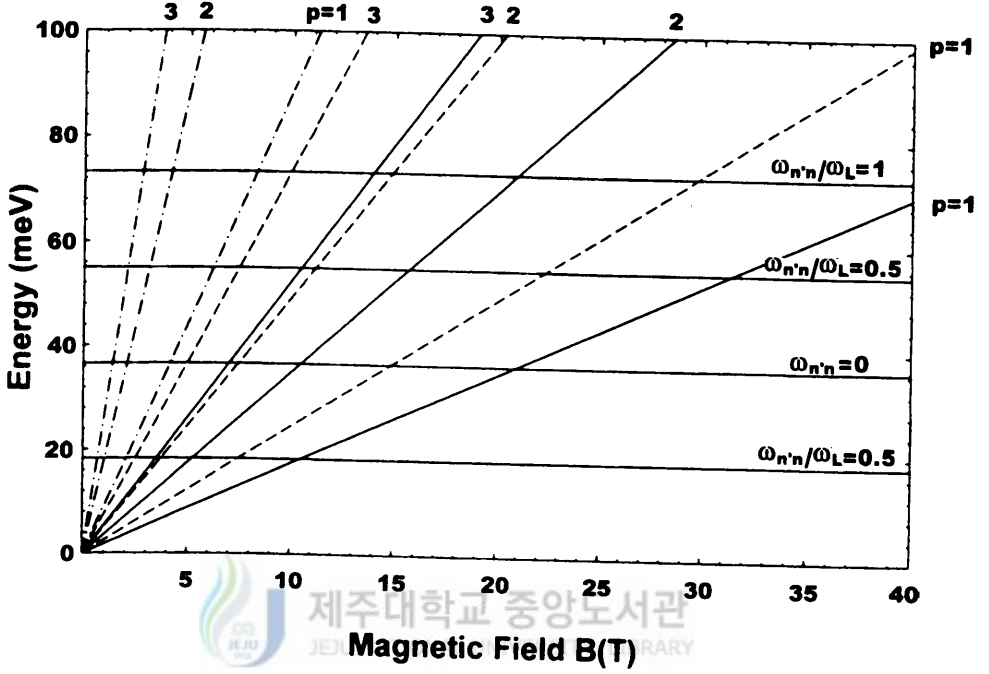


FIG. 6. Energy diagram is plotted as a function of magnetic field depending on the values of the both characteristic frequency of the y -directional confinement and energy separation of the subbands for the z direction. The difference of the quantum number of the Landau level ($P = N' - N$) is indicated for each line. The solid, dotted, and dashed-dotted lines are for $\Omega_y = 0.1\omega_c$, $\Omega_y = \omega_c$, and $\Omega_y = 5\omega_c$, respectively.

Figure 6 shows the energy diagram of the MPR at $P\tilde{\omega}_c = \omega_L$ and at $P\tilde{\omega}_c = \omega_L^\pm$, as a function of magnetic field. The quantum number of the Landau level is indicated for each line, depending on the value of Ω_y . The crossing points give the resonance magnetic fields, which depend on the strength of confinement in the z direction. We notice that the resonance magnetic field decreases as Ω_y increases. In the case where only intraelectric-virtual-subband transitions ($n \rightarrow n' = n$) take place, i.e., $\omega_{n'n} = 0$, there is no splitting of the MPR. However, we can see that whenever the interelectric

(nonresonant)-virtual-subband transitions take place for a relevant energy separation between subbands for the z direction, the splitting of the MPR peak positions occurs. The shift of the peak positions increases as the energy separation between two subband levels for the z direction increases. Figures 7(a)–7(c) show the energy diagram of the EPR at $\hbar\omega_{n'n} = \hbar\omega_L$ for three different confinement potentials for the z direction: a parabolic well, a square well and a triangular well, respectively. The quantum number of the subband level in the z direction is indicated for each line, where the initial and final states are represented by n and n' , respectively. Any changes in the confinement frequency Ω_z , the well width L_z , and the bias field F_z lead to changes of the energy separation between electric subbands, which allow us to have the energy levels in resonance with the optical-phonon energy. The crossing points given in Figs. 7(a)–7(c) indicate the resonance confinement frequency, the resonance well width, and the resonance bias field, respectively. As can be seen from Fig. 7(a), no EPR takes place for $\Omega_z > 5.56 \times 10^{13} \text{ sec}^{-1}$ since the energy separation between adjacent subband levels is larger than the optical phonon energy ($\hbar\omega_L = 36.6 \text{ meV}$ for GaAs). As Ω_z decreases (i.e., the well in z direction becomes wider), the energy separation between subbands n and n' becomes closer. Therefore, various resonance transitions from n to any n' are allowed to take place due to the LO phonons. Note that the reason for having the identical resonance frequencies for adjacent subband resonance transition is due to the fact that the energy separation between adjacent subband levels is all same. Unlike the parabolic well case, for the square well case given in Fig. 7(b), the resonance well-widths for adjacent subband resonance transition have different values, which is due to the fact that every energy separation between adjacent subband levels is not the same because the subband energy spectrum ε_n is proportional to n^2 and is not equidistant.

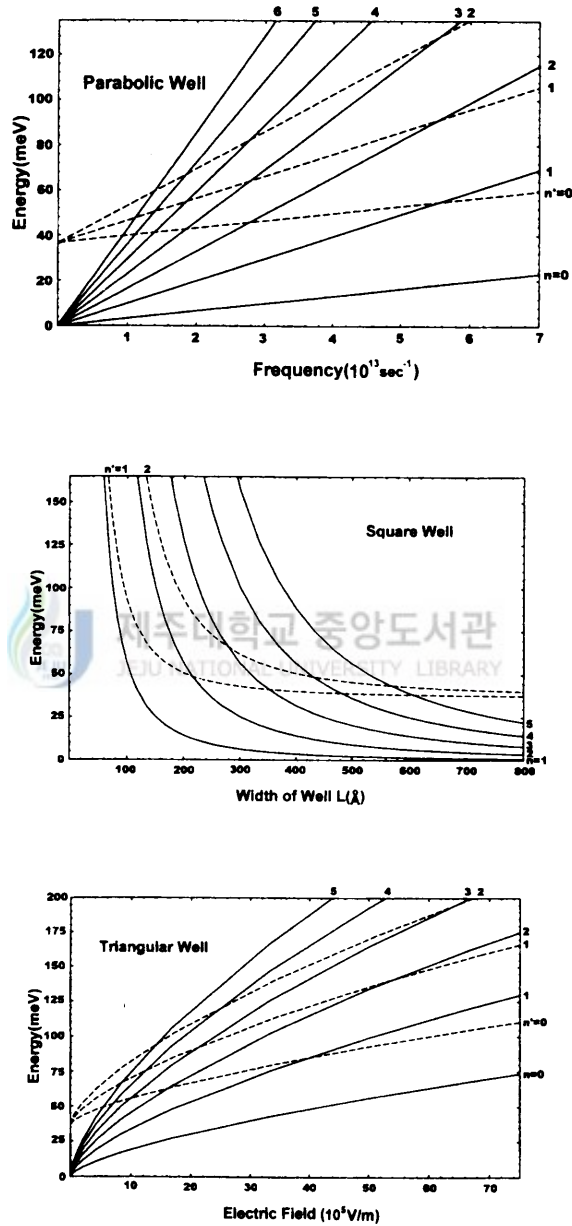


FIG. 7. Energy diagram is plotted as a function of (a) Ω_y , the characteristic frequency of the y -directional confinement for the parabolic-well case; (b) L_z , the width of the well for the square-well case; (c) F_s , the electric field for the triangular-well case. The quantum number of the subband level is indicated for each line.

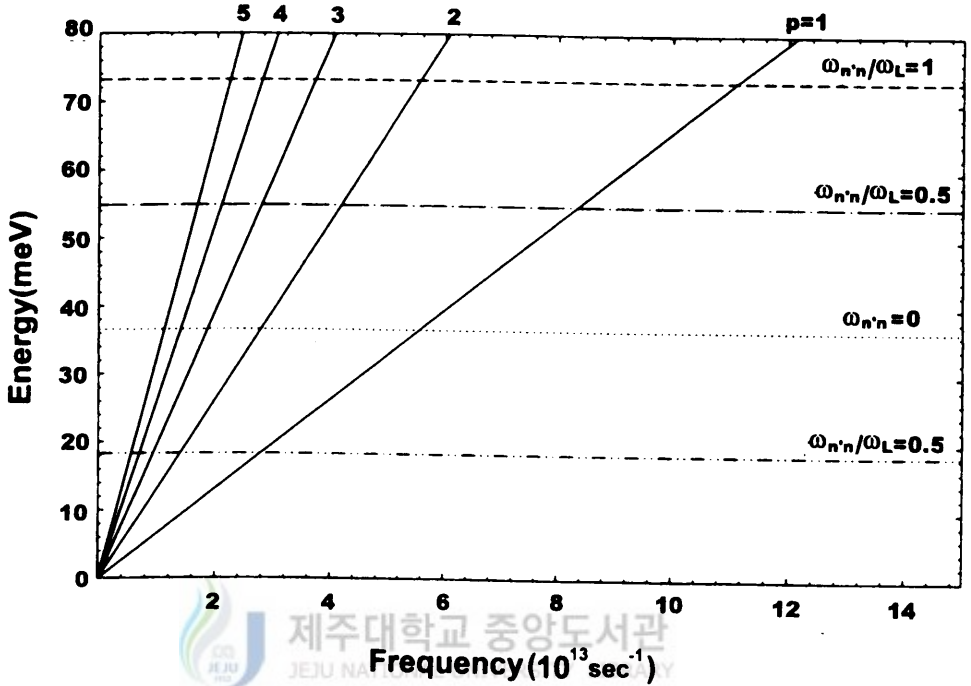


FIG. 8. Energy diagram is plotted as a function of characteristic frequency of the y -directional confinement depending on the values of the energy separation of the subbands for the z direction. The difference of the subbands ($P = N' - N$) for the y direction is indicated for each line.

We can see that as the thickness of the well increases, various resonance transitions from the subband level n to any n' take place. The results for increasing the well width $L_z \sim 1/\sqrt{\Omega_z}$ is similar to those for decreasing the confinement frequency Ω_z in the parabolic potential case. For the triangular well case given in Fig. 7(c), the energy separation between adjacent subband levels is altered by changing the bias field F_z . As the bias field is increased the well width in the z direction is decreased. As a result, the energy separation between adjacent subband levels becomes larger. This is similar to the parabolic potential case because increasing the confinement

frequency Ω_z is identical with decreasing the well width. Figure 8 shows the energy diagram of the EPR at $P\Omega_y = \omega_{LO}$ and $P\Omega_y = \omega_{LO}^\pm$, as a function of Ω_y for zero magnetic-field case. The quantum number of the subband level due to the confinement in the y direction is indicated for each line. The crossing points give the resonance confinement frequencies, which strongly depend on the strength of confinement in the z direction. We can see that, as in the MPR case, the splitting and shift of the peak positions increases as the energy separation between adjacent subband levels in the z direction increases.

D. Conclusions

So far, we have studied the MPR and EPR effect for a Q1D quantum-wire structure in the presence and absence of any magnetic field, in which a Q1DEG is confined by a parabolic well in the y direction and three kinds of confinement potentials in the z direction, including the parabolic well, the square well, and the triangular well. The transverse magnetoconductivity is directly related to the energy relaxation rate. The relaxation rate of Q1DEG formed in the quantum-wire structure was evaluated within the lowest-order approximation of the collision processes for optical phonon scatterings and its behavior was discussed in connection with the MPR and EPR effects. We see that the relaxation rate (and hence the transverse magnetoconductivity) shows resonant behaviors: MPR at $P\tilde{\omega}_c = \omega_L$ and at $P\tilde{\omega}_c = \omega_L \pm \omega_{n'n}$. In this case, change in $\omega_{n'n}$ gives rise to the splitting of the MPR effects whenever the virtual interelectric subband transitions take place for a relevant energy separation between two subbands in the z direction. Furthermore, the conductivity shows another resonant behavior: EPR due to the subband in

the z direction at $\omega_{n'n} = \omega_L$, which strongly depends on the subband structure in the z direction. The MPR condition at $P\tilde{\omega}_c = \omega_L$ is identical with those of Vasilopoulos et al. [23], assuming that only the lowest subband level formed in heterostructures is occupied. Occupation of several electric subbands gives rise to the additional oscillatory behavior of MPR effect and EPR effect. It should be noted that the MPR and EPR peak positions are strongly sensitive to the strength of the magnetic field, the optical phonon energy, the characteristic frequency of the y -directional confinement Ω_y , and the type of the confinement potential well in the z direction. In zero magnetic-field case, the relaxation rates (and hence the electric conductivity) show resonant behaviors due to the subband levels given in two different directions: EPR due to the subband level for the y direction at $P\Omega_y = \omega_L$ and at $P\Omega_y = \omega_L \pm \omega_{n'n}$, and EPR due to the subband for the z direction at $\omega_{n'n} = \omega_L$ and at $\omega_{n'n} = \omega_L \pm P\Omega_y$.

In present calculation for the conductivity, we considered the most simple situation of linear transport and a nondegenerate electron gas. The nonlinear MPR and EPR effects will be studied in a separate paper.

V. MAGNETOPHONON RESONANCES IN QUASI-ONE-DIMENSIONAL ELECTRONIC SYSTEMS IN TILTED MAGNETIC FIELDS

Over the past few decades, MPR effects in low-dimensional electron-gas systems have received much attention from both experimental and theoretical points of view since they can be used as an alternative magnetotransport tool for the measurement of the effective mass of quasi-two-dimensional electrons [41] and for the determination of the energy difference between adjacent quasi-one-dimensional sub-bands [42]. Many studies of MPR effects in such low-dimensional electronic systems have been reported [14,20–25,30,31,35,41–46]. However, most of the MPR theories presented so far are mainly restricted to the case where the magnetic field is applied normal to the interface layer of the system. Less work has been done [25] in the case where a magnetic field is applied to the Q2D electronic plane at an arbitrary angle. In this case, it is known that a suitably directed magnetic field serves to add an extra confining potential to the initial electrostatic confinement and causes a dramatic change in the energy spectrum, leading to so-called *hybrid* magnetoelectric quantization. As a consequence, one would expect different behavior of the MPR effects in such systems from the known MPR effects in three-dimensional EG systems.

Recently, Ryu, Hu, and O'Connell [25] presented the MPR conditions of Q1D systems in tilted magnetic fields, based on a simple model of parabolic confining potentials. In their study, they neglected the coupling Hamiltonian term $\sim B_x B_z xz$, since its contribution to the total electron energy is minor. This is valid for the case where the initial electrostatic confinements are stronger than the magnetic confinement. More recently, Suzuki and Ogawa [26] investigated in detail qualitative features of the MPR effects, their physical origin, and the dimensional crossover

between Q2D and Q1D systems in tilted magnetic fields, based on the same model as Ryu et al. [25]. However, their studies are confined to the weak confinement case where the electrostatic confining parameters are smaller than the cyclotron resonance frequency. Therefore, a theory of MPR effects which is valid for the weak confinement case and the strong confinement case is needed and it is necessary to investigate various qualitative features of the MPR effects in Q1D systems, according to the strength of electrostatic potentials and the tilt angle of the applied magnetic field.

The purpose of the present work is to extend the previous results [25] by including the coupling Hamiltonian term $\sim B_x B_z xz$, to understand various qualitative behaviors of the MPR effects in Q1D electronic systems according to the strength of electrostatic potentials and the tilt angle of the applied magnetic field, and to compare our present results with the results presented by other authors. For this purpose, we shall review the conductivity σ_{yy} for Q1D electronic systems subjected to a tilted magnetic field, on the basis of the simple parabolic model for confinement potential, and obtain MPR conditions as a function of the strength parameters (ω_1 and ω_2) of the parabolic potentials, which characterize the strength of confinement of Q1DEG. We will investigate how the MPR effects are affected by the tilt angle of applied magnetic fields and by the strengths of the confining potentials.

The rest of the chapter is organized as follows. In Sec. A, we review an exactly solvable model for Q1D electronic systems. General formulae of the transverse magnetoconductivity σ_{yy} for the Q1D systems are presented in Sec. B, where the conductivity consists of the usual Drude term arising from the drift motion of electrons and hopping terms associated with MPR. The relaxation rate, which is closely related to the MPR, is evaluated for the quantum limit condition, assuming that the

interaction with bulk LO phonon is the dominant scattering mechanism. Numerical results of magnetoconductivity for the Q1D systems are presented in Sec. C. In particular, the MPR conditions for the model system are given explicitly and the effects of tilted magnetic fields and the confining potential on the MPR are discussed. Here, special attention is given to the behavior of the MPR lineshape, such as the appearance of subsidiary MPR peaks, the shift of these MPR peaks and a change in MPR amplitude and width. Concluding remarks will be given in last section.

A. Model for Q1D Electronic Systems in Tilted Magnetic Fields

We consider the transport of an electron gas in a quantum-wire structure as treated by Ihm et al. [47]. The Q2D electron gas is assumed to be confined to the $x - y$ plane by an ideal parabolic potential $\frac{1}{2}m^*\omega_2^2z^2$, whereas the Q1D electron gas is assumed to be further confined in the x -direction by an additional parabolic potential $\frac{1}{2}m^*\omega_1^2x^2$, thus restricting free motion to the y -axis alone. In the presence of a magnetic field, one-particle Hamiltonian (h_e) for such Q1D electrons is expressed in a unified manner by

$$h_e = \frac{1}{2m^*}(\mathbf{p}+e\mathbf{A})^2 + \frac{1}{2}m^*\omega_1^2x^2 + \frac{1}{2}m^*\omega_2^2z^2, \quad (5.1)$$

where \mathbf{A} is a vector potential accounting for a constant magnetic field $\mathbf{B} = \nabla \times \mathbf{A}$ and m^* is the effective mass. We can see the dimensional crossover between the Q2D and the Q1D electronic systems (i.e., $\omega_1 \rightarrow 0$ or $\omega_2 \rightarrow 0$ for the Q2D electronic system) as well as the difference in the strength of each confinement by varying the confining potential parameters (ω_1 and ω_2) in Eq. (5.1) for the Q1D systems. We shall consider the case where the magnetic field \mathbf{B} is applied in the transverse tilt direction to the wire of the system: $B = (B_x, 0, B_z) = (B \sin \theta, 0, B \cos \theta)$, with the

Landau gauge $\mathbf{A} = (0, xB_z - zB_x, 0)$. Here the angle θ is measured from the z axis in the $x - z$ plane. Then, the one-particle Hamiltonian (5.1) for those confined (Q1D) electrons subject to the transverse tilted magnetic field can be represented in the new Cartesian coordinates (x', y', z') as

$$h_e = \frac{P_{x'}^2}{2m^*} + \frac{P_{z'}^2}{2m^*} + \frac{1}{2}m^*\Omega_1^2 x'^2 + \frac{1}{2}m^*\Omega_2^2 z'^2 - m^*\omega_x\omega_z x'z' + \frac{P_{y'}^2}{2\tilde{m}^*}, \quad (5.2)$$

which represents two coupled harmonic oscillators, where $\omega_x = \omega_c \sin \theta$, $\omega_z = \omega_c \cos \theta$, $\omega_c = eB/m^*$, $\tilde{m}^* = m^*(\Omega_1^2\Omega_2^2 - \omega_x^2\omega_z^2)/\omega_1^2\omega_2^2$, $\Omega_1^2 = \omega_1^2 + \omega_z^2$, and $\Omega_2^2 = \omega_2^2 + \omega_x^2$. To obtain Eq. (5.2), we performed the following unitary transformation: $x'_i = U_1 x_i U_1^{-1}$ and $P_{x'_i} = U_1 P_{x_i} U_1^{-1}$ for an arbitrary x_i ($x_i = x, y$, and z for $i = 1, 2$ and 3 , respectively). Here $U_1 = \exp[iG_1/\hbar]$ is a unitary operator with $G_1 = \omega_z P_y P_x / (\tilde{m}^* \omega_1^2) - \omega_x P_z P_y / (\tilde{m}^* \omega_2^2)$.

For the purpose of diagonalizing the one-particle Hamiltonian given by Eq. (5.2), we take into account another unitary transformation: $X_i = U_2 x'_i U_2^{-1}$ and $P_{X_i} = U_2 P_{x'_i} U_2^{-1}$ for an arbitrary x'_i ($x'_i = x', y'$, and z' for $i = 1, 2$ and 3 , respectively), where $U_2 = \exp[iG_2/\hbar]$ is a unitary operator having $G_2 = \{x' P_{z'} - z' P_{x'}\} \phi$ with $\phi = \arctan\{\Omega_2^2 - \omega_-^2 / (\Omega_1^2 - \omega_-^2)\}$. Here ω_- is the effective cyclotron frequency in the Z -direction. Then, Eq. (5.2) can be expressed in the simplified manner as

$$h_e = \frac{1}{2m^*} P_X^2 + \frac{1}{2m^*} P_Z^2 + \frac{1}{2m^*} \omega_+^2 X^2 + \frac{1}{2m^*} \omega_-^2 Z^2 + \frac{1}{2\tilde{m}^*} P_Y^2, \quad (5.3)$$

where ω_+^2 and ω_-^2 are respectively given by $\omega_{\pm}^2 = \frac{1}{2}[\Omega_1^2 + \Omega_2^2 \pm \sqrt{(\Omega_1^2 - \Omega_2^2)^2 + 4\omega_x^2\omega_z^2}]$. The Hamiltonian (5.3) represented in the new Cartesian coordinates is basically changed into the Hamiltonian for two independent 1D simple harmonic oscillators, one with the effective cyclotron frequency ω_+ in the X -direction and the other with the effective cyclotron frequency ω_- in the Z -direction. The last term in Eq. (5.3) denotes the y -component kinetic energy of a confined electron with a field-dependent

renormalized mass \tilde{m}^* with respect to the effective mass m^* . In particular, the effective mass \tilde{m}^* is influenced by a factor $(\Omega_1^2\Omega_2^2 - \omega_x^2\omega_z^2) / \omega_1^2\omega_2^2$, which depends on a tilt angle θ , the cyclotron frequency ω_c , and the confining potential parameters (ω_1, ω_2) characterizing the dimensionality of the system. The momentum component $P_y (= P_Y)$ is a constant of motion and can be written as $P_Y = \hbar k_Y$, where k_Y is the quasi-continuous wave vector of motion parallel to the interfaces (viz., wire in the $y (= Y)$ direction).

The normalized eigenfunctions and eigenenergies of the one-electron Hamiltonian (5.3) are given by

$$\langle \mathbf{R} | \lambda \rangle \equiv \langle X, Y, Z | n, l, k_y \rangle = \left(\frac{1}{L_y} \right)^{1/2} \Psi_n(X) \Psi_l(Z) \exp(ik_y Y) \quad (5.4)$$

and

$$E_\lambda \equiv E_{n,l}(k_y) = (n + 1/2)\hbar\omega_+ + (l + 1/2)\hbar\omega_- + \frac{(\hbar k_y)^2}{2\tilde{m}^*}, \quad n, l = 0, 1, 2, \dots, \quad (5.5)$$

respectively. In Eq. (5.4), $\Psi_n(X)$ and $\Psi_l(Z)$ denote 1D simple-harmonic-oscillator wave functions. The state of the Q1D system are specified by two Landau level indices n, l and the wave function $\exp(ik_y y)$ in Eq. (5.4) expresses a free motion in the y (i.e., Y) direction. As shown in Eq. (5.5), the energy spectrum for the present Q1D system is *hybrid*-quantized due to the presence of the tilted magnetic field. The set of quantum numbers is designated by (n, l, k_y) , where n and l denote the effective Landau (magnetic) level indices. We note that the dimensional crossover can be seen in the energy spectrum by simply varying the confining potential parameters; ω_1 or $\omega_2 \rightarrow 0$ for the Q2DEG system and ω_1 and $\omega_2 \rightarrow 0$ for the 3DEG system.

B. Magnetoconductivity Associated with Relaxation Rates

In this section, we want to evaluate an analytical expression of the transverse magnetoconductivity σ_{yy} for the Q1D systems previously described, by taking the real part of a general expression for the complex nonlinear dc conductivity $\tilde{\sigma}_{kl}(E)$ ($k, l = x, y, z$) given in Ref. 4 and the linear response limit, i.e., $\lim_{E \rightarrow 0} \text{Re}\{\tilde{\sigma}_{kl}(E)\} \equiv \sigma_{kl}$. The dc linear conductivity for weak electric fields is obtained by the sum of the non-hopping part σ_{yy}^{nh} and the hopping part σ_{yy}^h , which are

$$\sigma_{yy}^{nh} = \frac{\hbar^3 \beta e^2}{\tilde{m}^* 2V} \sum_{n,l,k_y} k_y^2 f(E_{nl}(k_y)) [1 - f(E_{nl}(k_y))] / \tilde{\Gamma}(n, l, k_y; n, l, k_y), \quad (5.6)$$

$$\begin{aligned} \sigma_{yy}^h = & \frac{e^2 \omega_z^2 l_+^2}{V \omega_+} \sum_{n,l,k_y} (n+1) [f(E_{nl}(k_y)) - f(E_{n+1l}(k_y))] \frac{\tilde{\Gamma}(n+1, l, k_y; n, l, k_y)}{(\hbar \omega_+)^2 + \tilde{\Gamma}^2(n+1, l, k_y; n, l, k_y)} \\ & + \frac{e^2 \omega_x^2 l_-^2}{V \omega_-} \sum_{n,l,k_y} (l+1) [f(E_{nl}(k_y)) - f(E_{nl+1}(k_y))] \frac{\tilde{\Gamma}(n, l+1, k_y; n, l, k_y)}{(\hbar \omega_-)^2 + \tilde{\Gamma}^2(n, l+1, k_y; n, l, k_y)} \end{aligned} \quad (5.7)$$

for the shift zero in the spectral line shape, where $V = L_x L_y L_z$ is the volume of the system and $\beta = 1/k_B T$ with k_B being the Boltzmann constant and T temperature. Also, $l_{\pm} = \sqrt{\hbar/m^* \omega_{\pm}}$, \hbar is the Plank constant divided by 2π , $f(E_{nl}(k_y))$ is a Fermi-Dirac distribution function for electrons with the eigenstate $|n, l, k_y\rangle$ of Eq. (5.4) and the energy $E_{nl}(k_y)$ of Eq. (5.5), and $-e (< 0)$ is the electron charge. The quantity $\tilde{\Gamma}$ given in Eqs. (5.6) and (5.7), which appears in terms of the collision broadening due to the electron-background (phonon or impurity) interaction, play the role of the relaxation rate in the spectral line shape. To obtain Eqs. (5.6) and (5.7), we used the matrix elements $|\langle k_y, l, n | j_Y | k'_y, l', n' \rangle|^2$ given by

$$\begin{aligned}
| \langle k_y, l, n | j_Y | k'_y, l', n' \rangle |^2 &= (e\hbar k_y / \tilde{m}^*)^2 \delta_{nn'} \delta_{ll'} \delta_{k_y k'_y}, \\
&+ (e\omega_z l_+ / \sqrt{2})^2 [n \delta_{n'n-1} + (n+1) \delta_{n'n+1}] \delta_{ll'} \delta_{k_y k'_y}, \\
&+ (e\omega_x l_- / \sqrt{2})^2 [l \delta_{l'l-1} + (l+1) \delta_{l'l+1}] \delta_{nn'} \delta_{k_y k'_y}, \quad (5.8)
\end{aligned}$$

where the Kronecker symbols ($\delta_{n'n}, \delta_{l'l}, \delta_{k_y k'_y}$) denote the selection rules, which arise during the integration of the matrix elements with respect to each direction. Equation (5.6) expresses the Drude term arising from the drift (non-hopping) motion of electrons within the localized states through the electron-phonon interaction. In contrast, Eq. (5.7) expresses the hopping terms, which are associated with electron hopping motion between the localized (effective Landau- and/or sub-band-) states by absorbing and/or emitting a phonon with an energy $\hbar\omega_{\mathbf{q}}$ in the scattering events. In fact, these terms are related to the oscillatory behavior of MPR effects. Accordingly, hereafter we shall denote the transverse magnetoconductivity associated with these hopping terms as σ_{yy}^{MPR} . As shown in Eq. (5.7), the electronic transport properties (e.g., electronic relaxation processes, magnetophonon resonances, etc.) in the Q1D systems can be studied by examining the behavior of $\tilde{\Gamma}$ as a function of the relevant physical parameters introduced in the theory.

An analytical expression of the relaxation rate in the lowest-order approximation for the weak electron-phonon interaction and in the limit of weak electric fields can be evaluated from the general expression of the electric-field dependent relaxation rate given by Eq. (4.39) of Ref. 4. The Q1D version of the relaxation rate associated with the electronic transition between the states $| n_1, l_1, k_{1y} \rangle$ and $| n, l, k_y \rangle$ is expressed by

$$\begin{aligned}
\tilde{\Gamma}(n_1, l_1, k_{1y}; n, l, k_y) &= \frac{D'}{4\pi^2 l_+ l_-} \sum_{(n', l') \neq (n_1, l_1)} F_{n_1 n'}(\Delta n) F_{l_1 l'}(\Delta l) \int_{-\infty}^{\infty} dq_Y \\
&\times \{ (N_0 + 1) \delta[(n - n')\hbar\omega_+ + (l - l')\hbar\omega_- + S(k_y, k'_y) - \hbar\omega_L]
\end{aligned}$$

$$\begin{aligned}
& + N_0 \delta[(n - n')\hbar\omega_+ + (l - l')\hbar\omega_- + S(k_y, k'_y) + \hbar\omega_L] \} \\
& + \frac{D'}{4\pi^2 l_+ l_-} \sum_{(n', l') \neq (n, l)} F_{n'n}(\Delta n) F_{l'l}(\Delta l) \int_{-\infty}^{\infty} dq_y \\
& \times \{ (N_0 + 1) \delta[(n' - n_1)\hbar\omega_+ + (l' - l_1)\hbar\omega_- + S(k'_y, k_{1y}) + \hbar\omega_L] \\
& + N_0 \delta[(n' - n_1)\hbar\omega_+ + (l' - l_1)\hbar\omega_- + S(k'_y, k_{1y}) - \hbar\omega_L] \} \quad (5.9)
\end{aligned}$$

with $S(k_y, k'_y) = \hbar^2(k_y^2 - k'_y{}^2)/2\tilde{m}^*$ and $S(k'_y, k_{1y}) = \hbar^2(k'_y{}^2 - k_{1y}^2)/2\tilde{m}^*$, where N_0 is the optical-phonon distribution function given by $N_{\mathbf{q}} = [\exp(\beta\hbar\omega_{\mathbf{q}}) - 1]^{-1}$ with $\omega_{\mathbf{q}} = \omega_L$ and n' and l' indicate the intermediate localized Landau level indices. In order to obtain the relaxation rates $\tilde{\Gamma}$ of Eq. (5.9) for a specific electron-phonon interaction, we considered the Fourier component of the interaction potential [20,25,26] for optical phonon scattering given by D'/V with $D' = \hbar D^2/2\rho\omega_L \approx \text{const}$, D being a constant, and ρ being the density, where the assumption was made that the phonons are dispersionless (i.e., $\hbar\omega_{\vec{q}} \approx \hbar\omega_L \approx \text{constant}$, where ω_L is the optical phonon frequency) and bulk (i.e., three-dimensional). We also took into account the following matrix element in the representation (5.4):

$$|\langle n, l, k_y | U \exp(\pm i\vec{q} \cdot \vec{r}) U^{-1} | n', l', k'_y \rangle|^2 = |J_{nn'}(u_+)|^2 |J_{ll'}(u_-)|^2 \delta_{k'_y, k_y \mp q_y}, \quad (5.10)$$

$$|J_{nn'}(u)|^2 = \frac{n_{<}!}{n_{>}!} e^{-u} u^{\Delta n} [L_{n_{>}}^{\Delta n}(u)]^2, \quad (5.11)$$

where $n_{<} = \min\{n, n'\}$, $n_{>} = \max\{n, n'\}$, $u_+ = l_+^2 q_X^2/2$, $u_- = l_-^2 q_Z^2/2$, and $L_{n_{<}}^{\Delta n}(u)$ is an associated Laguerre polynomial [15] with $\Delta n = n_{>} - n_{<}$. In addition, we utilized the following relation in doing the integral over q_X and q_Z :

$$\begin{aligned}
F_{n'n}(\Delta n) & \equiv \int_0^{\infty} \frac{1}{\sqrt{u}} |J_{n'n}(u)|^2 du \\
& = \frac{n_{<}! (1 + \Delta n)_{n_{<}} (2\Delta n + \frac{3}{2})_{n_{<}} \Gamma(\Delta n + \frac{1}{2})}{n_{>}! (n_{<}!)^2}
\end{aligned}$$

$$\times {}_3\Phi_2(-n_<, \Delta n + \frac{1}{2}, \frac{1}{2}; \Delta n + 1, \frac{1}{2} - n_<; 1). \quad (5.12)$$

Here ${}_3\Phi_2(a, b, c; d, e; x)$ is the hypergeometric function [15]

$${}_3\Phi_2(a, b, c; d, e; x) = \sum_{n=0}^{\infty} \frac{(a)_n (b)_n (c)_n x^n}{(d)_n (e)_n n!} \quad (5.13)$$

with the Pochhammer's symbol $(a)_n$ defined by $(a)_n = a(a+1)\cdots(a+n-1) = \Gamma(a+n)/\Gamma(a)$. It should be noted that the Landau level indices n_1 and l_1 given in Eq. (5.9) are, respectively, replaced by $n+1$ and l or n and $l+1$ for the electron hopping motion, depending on the type of the transitions associated with the Landau-level index, and that the summations of Eq. (5.9) over the Landau level can be, respectively, divided into two possible cases: (i) $\sum_{n' \neq n_1} \sum_{l'}$ and $\sum_{n' \neq n, \sum_{l'}}$, and (ii) $\sum_{n'} \sum_{l' \neq l_1}$ and $\sum_{n'} \sum_{l' \neq l}$ since the condition $(n', l') \neq (n_1, l_1)$ in the summation of Eq. (5.9) contains three types of contributions: (i) $n' \neq n_1, l' \neq l_1$, (ii) $n' \neq n_1, l' = l_1$, and (iii) $n' = n_1, l' \neq l_1$. The δ functions in Eq. (5.9) express the law of energy conservation in one-phonon collision (absorption and emission) processes. The strict energy-conserving δ functions in Eq. (5.9) imply that when the electron undergoes a collision by absorbing energy from the field, its energy can only change by an amount equal to the energy of a phonon involved in the transitions. This in fact leads to MPR effects due to the Landau levels.

Now, let us consider the case where the non-degenerate limit and the quantum limit ($\hbar\omega_+, \hbar\omega_- \gg k_B T$) are satisfied so that the electrons can be in the lowest Landau levels (viz., $n = 0$ and $l = 0$). Then, the transverse magnetoconductivity of Eq. (5.7) for the electron hopping motion due to the Landau-level indices n and l can be expressed by

$$\sigma_{yy}^{MPR} \approx n_e e^2 \sqrt{\frac{\beta^3 \hbar^6}{2\tilde{m}^* 3\pi}} \frac{\omega_z^2 l_+^2}{\omega_+} \{1 - \exp[-\beta \hbar \omega_+]\}$$

$$\begin{aligned}
& \times \int dk_y \exp[-\beta \frac{(\hbar k_y)^2}{2\tilde{m}^*}] \frac{\tilde{\Gamma}(1, 0, k_y; 0, 0, k_y)}{(\hbar\omega_+)^2 + \tilde{\Gamma}^2(1, 0, k_y; 0, 0, k_y)} \\
& + n_e e^2 \sqrt{\frac{\beta^3 \hbar^6}{2\tilde{m}^*{}^3 \pi} \frac{\omega_x^2 l^2}{\omega_-}} \{1 - \exp[-\beta \hbar\omega_-]\} \\
& \times \int dk_y \exp[-\beta \frac{(\hbar k_y)^2}{2\tilde{m}^*}] \frac{\tilde{\Gamma}(0, 1, k_y; 0, 0, k_y)}{(\hbar\omega_-)^2 + \tilde{\Gamma}^2(0, 1, k_y; 0, 0, k_y)}, \tag{5.14}
\end{aligned}$$

where $n_e = N_e/V$ is the electron density with $N_e = \sqrt{2\tilde{m}^* L_y^2 / \beta \pi \hbar^2} \exp[\beta\{E_F - \hbar(\omega_+ + \omega_-)/2\}]$. To obtain the dc magnetoconductivity of Eq. (5.14) in simpler form, we assumed that the f 's in Eq. (5.7) are replaced by the Boltzmann distribution function for non-degenerate semiconductors [23,25,26,35], i.e., $f(E_{n,l}(k_y)) \approx \exp[\beta(E_F - E_{nl}(k_y))]$, where E_F denotes the Fermi energy. We also replaced one summation with respect to k_y in \sum_{n,l,k_y} by the following relation [23,25,26,35]: $\sum_{k_y}(\dots) \rightarrow (L_y/2\pi) \int_{-\infty}^{\infty} dk_y(\dots)$. In the case where the quantum limit ($\hbar\omega_+, \hbar\omega_- \gg k_B T$) are satisfied, only one or two Landau levels are customarily occupied. Accordingly, it may be sufficient for us to consider the electronic transitions between the states specified by $n_i = 0, 1$ and $l_i = 0, 1$ ($i = 1, 2$) in Eq. (5.9) for the fundamental MPR. Then, the relaxation rates of Eq. (5.9) for the electron hopping motion due to the Landau-level indices n and l are respectively given, after the q_Y integration, by

$$\begin{aligned}
\tilde{\Gamma}(1, 0, k_y; 0, 0, k_y) = N_0 \Lambda \{ & \frac{1}{\sqrt{|2\tilde{m}^* \{\hbar\omega_- - \hbar\omega_L\} / \hbar^2 - k_y^2|}} \\
& + \frac{(3/4)}{\sqrt{|2\tilde{m}^* \{\hbar\omega_+ + \hbar\omega_- - \hbar\omega_L\} / \hbar^2 - k_y^2|}} \\
& + \frac{1}{\sqrt{|2\tilde{m}^* \{\hbar\omega_- - \hbar\omega_+ - \hbar\omega_L\} / \hbar^2 - k_y^2|}} \}, \tag{5.15}
\end{aligned}$$

$$\tilde{\Gamma}(0, 1, k_y; 0, 0, k_y) = N_0 \Lambda \left\{ \frac{1}{\sqrt{|2\tilde{m}^* \{\hbar\omega_+ - \hbar\omega_L\} / \hbar^2 - k_y^2|}} \right\}$$

$$\begin{aligned}
& + \frac{(3/4)}{\sqrt{|2\tilde{m}^*\{\hbar\omega_+ + \hbar\omega_- - \hbar\omega_L\}/\hbar^2 - k_y^2|}} \\
& + \frac{1}{\sqrt{|2\tilde{m}^*\{\hbar\omega_+ - \hbar\omega_- - \hbar\omega_L\}/\hbar^2 - k_y^2|}}, \quad (5.16)
\end{aligned}$$

where $\Lambda = D'\tilde{m}^*/4\pi l_+ l_- \hbar^2$. Note that we considered only the phonon absorption process since we are interested in the physical properties of MPR in a specific process. As can be seen from Eqs. (5.14) – (5.16), the relaxation rates play an important role to determine the height and width of the MPR peaks as well as their peak positions. Equation. (5.14), supplemented by Eqs. (5.15) and (5.16), is the basic equation for the MPR spectral lineshape arising from the electron hopping motion between the effective Landau states by absorbing a phonon with an energy $\hbar\omega_q$ in the scattering events, which enables us to analyze MPR effects in the Q1D electronic systems under tilted magnetic fields.

C. Numerical Results and Discussion

In this section we present the numerical results of the magnetoconductivity formula σ_{yy}^{MPR} in Eq. (5.14), which is related to the MPR for the Q1D electronic systems based on the model described in Sec. A. Here, special attention is given to the behavior of the MPR lineshape, such as the appearance of subsidiary MPR peaks, the shift of these MPR peaks, and a change in MPR amplitude and width. For our numerical results of Eq. (5.14), we consider the Q1D electronic systems with effective mass $m^* = 0.067 m_0$ with m_0 being the electron rest mass and LO-phonon energy $\hbar\omega_L = 36.6$ meV as an example. The sample temperature is assumed to be 50 K in this calculation. The quantities n_e and D' in Eqs. (5.14)–(5.16) are respectively taken by $\sqrt{2m^*\pi^3\hbar^2/D'^2e^4\beta^3}$ and $4\sqrt{2} \times 10^{-25}\pi\hbar^3/\sqrt{\beta m^*3N_0^2}$ for simplicity.

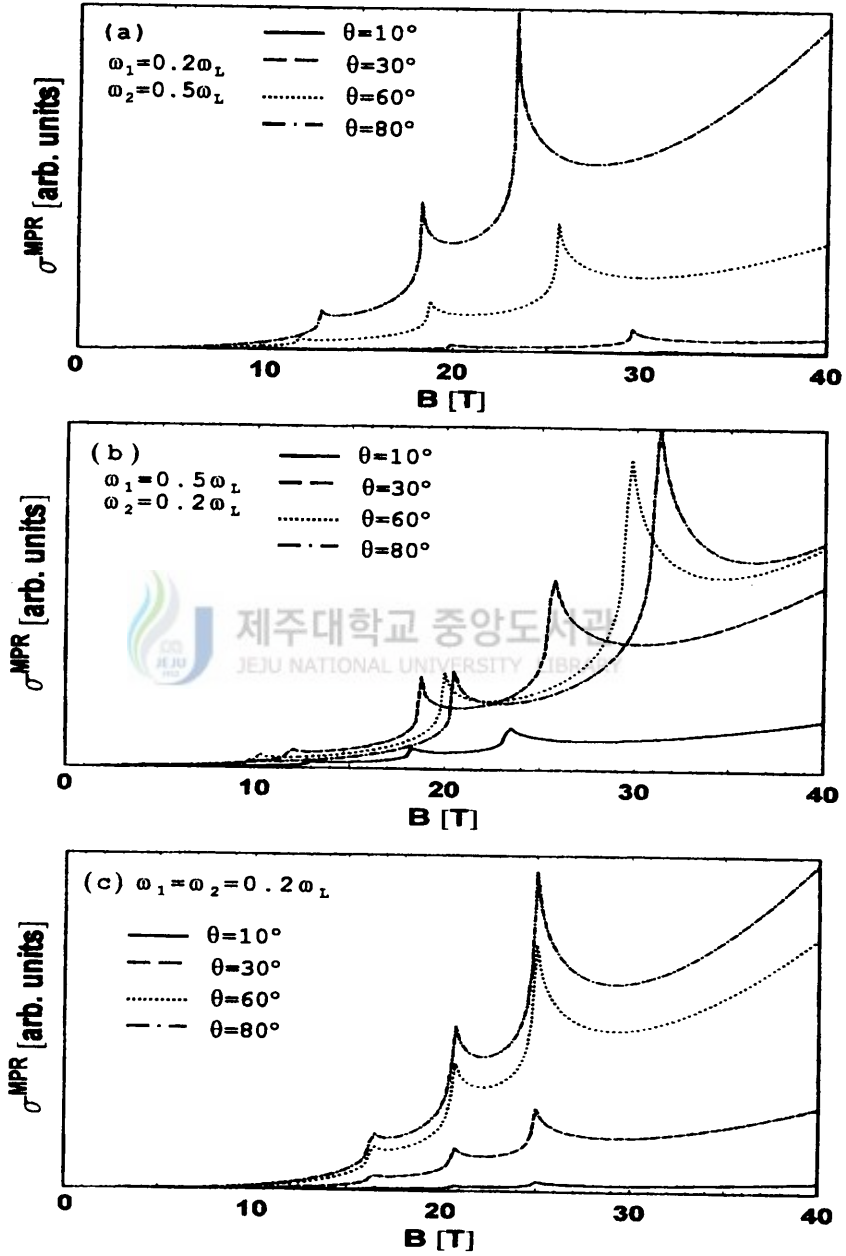


FIG. 9. Magnetic field (B) dependence of the magnetoconductivity (σ_{yy}^{MPR}) for different tilt angles (θ 's): (a) $\omega_1 = 0.2\omega_L$, $\omega_2 = 0.5\omega_L$, (b) $\omega_1 = 0.5\omega_L$, $\omega_2 = 0.2\omega_L$, and (c) $\omega_1 = \omega_2 = 0.2\omega_L$.

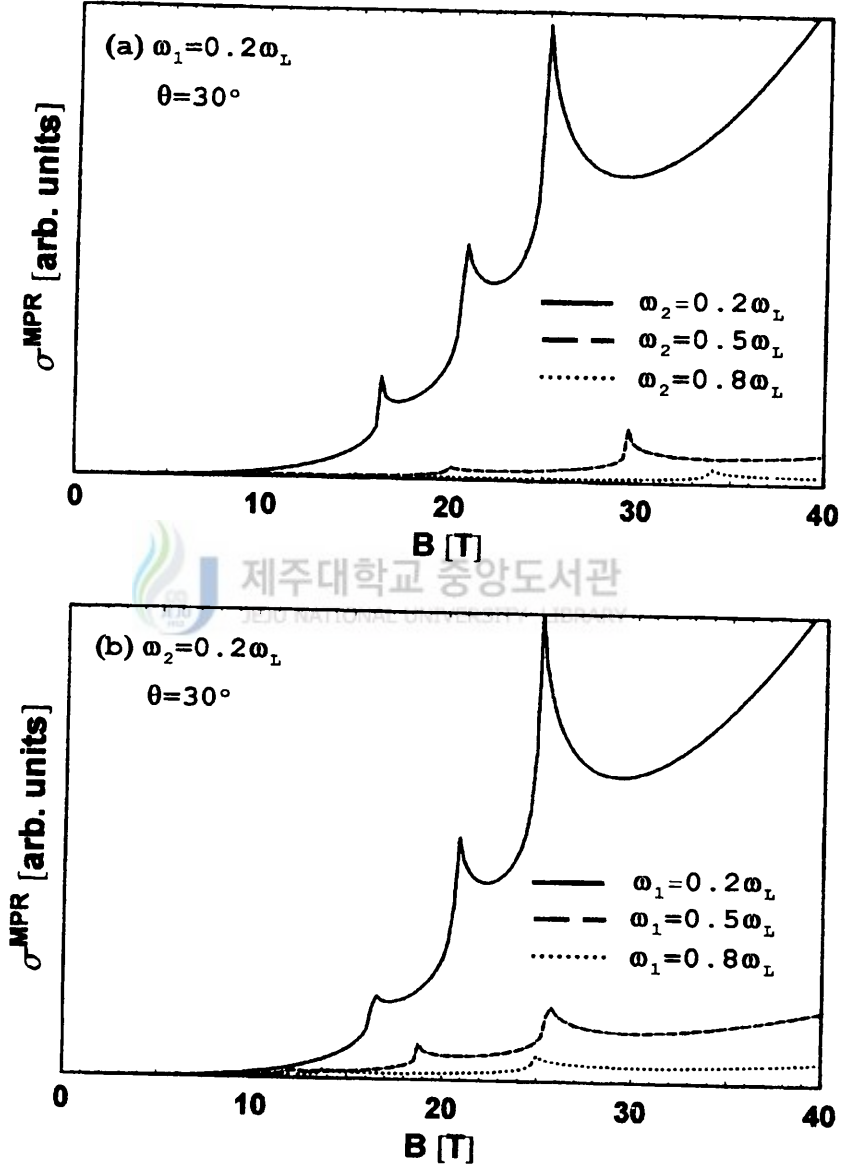


FIG. 10. Magnetic field (B) dependence of the magnetoconductivity (σ_{yy}^{MPR}) for (a) the change of the confining potential strength ω_2 in the z direction and (b) the change of the confining potential strength ω_1 in the x direction.

Figure 9 shows the spectral lineshapes of σ_{yy}^{MPR} for the Q1D system as a function of magnetic field B for various tilt angles θ of the transverse tilted magnetic field $B = (B \sin \theta, 0, \cos \theta)$ applied to the electronic wire, where we considered three cases for confinement frequencies ω_1 and ω_2 in the x and z direction: (a) $\omega_1 = 0.2\omega_L$ and $\omega_2 = 0.5\omega_L$, (b) $\omega_1 = 0.5\omega_L$ and $\omega_2 = 0.2\omega_L$, and (c) $\omega_1 = \omega_2 = 0.2\omega_L$, as an example, in order to see the effect of tilted magnetic fields, viz., θ dependency of MPR depending on the condition of the confining potential parameters. Moreover, to understand the effect of electrostatic confining potentials (characterized by ω_1 , ω_2) on MPR, we plotted the spectral lineshapes of σ_{yy}^{MPR} for the Q1D system in Fig. 10, as a function of magnetic field B for various confining potential parameters at a fixed angles θ , where the tilt angle was taken as 30° as a matter of convenience. In these figures, we can see the following features for the Q1D system: (i) there are three peaks in the σ_{yy}^{MPR} under the magnetic field up to 40 Tesla; (ii) the shift of the resonant peaks in the conductivity for $\omega_1 \neq \omega_2$ corresponding to an asymmetric quantum wire is very sensitive to the tilt angle θ of applied magnetic field and the relative strength of the confining potential parameters ω_1 and ω_2 in the x and z direction, while for $\omega_1 = \omega_2$ corresponding to a symmetric quantum wire, it does not depend on the tilt angle, and (iii) the height of these peaks and their resonance widths are closely related to the tilt angle θ and the confining potential parameters ω_1 and ω_2 .

Let us first examine feature (i). Since MPR is a phenomenon which occurs in the electronic system subjected to quantizing magnetic fields, the resonant transition in the Q1D electronic structure under tilted magnetic fields takes place in terms of the Landau-level-indices n and l , whereby $\hbar\omega_+$, $\hbar\omega_- \gg \tilde{\Gamma}$ are satisfied. In this case, the abrupt change of the relaxation time (and hence magnetoconductivity) is expected

to occur at the resonant magnetic field when we vary the strength and/or the tilt angle θ of the applied magnetic field. As can be seen from Eqs. (5.14)–(5.16), there are four possible cases which change $\tilde{\Gamma}$ abruptly under the condition that the density of states is maximum (i.e., at $k = 0$): $\hbar\omega_- = \hbar\omega_L$, $\hbar\omega_+ + \hbar\omega_- = \hbar\omega_L$, $\hbar\omega_+ = \hbar\omega_L$, and $\hbar\omega_+ - \hbar\omega_- = \hbar\omega_L$, which are the conditions for MPR giving the peak positions (i.e., resonant magnetic fields) in the spectral lineshape, because the condition $\hbar\omega_- - \hbar\omega_+ = \hbar\omega_L$ is obviously impossible from the definition of the effective frequencies ω_+ and ω_- . For given ω_1 and ω_2 in Figs. 9 and 10, however, the resonant behaviors are actually given by the following three cases:

$$\hbar\omega_+ + \hbar\omega_- = \hbar\omega_L, \quad \hbar\omega_+ = \hbar\omega_L, \quad \hbar\omega_+ - \hbar\omega_- = \hbar\omega_L \quad (5.17)$$

under the magnetic field up to 40 Tesla, which are reduced to the MPR conditions of the Q2D system in tilted magnetic fields, if ω_1 or $\omega_2 \rightarrow 0$ is taken in Eq. (5.17). In the course of scattering events, the electrons in the effective Landau and sub-band levels specified by the level indices (n, l) could make transitions to one of the effective Landau and sub-band levels (n', l') by absorbing a LO-phonon energy $\hbar\omega_L$ when the conditions (5.17) are satisfied. The first condition indicates a process corresponding to the electronic transition from $(n, l) = (0, 0)$ to $(1, 1)$, where quasi-electrons having respective energy of $\hbar\omega_+$ and $\hbar\omega_-$ are created by absorbing a LO-phonon with energy $\hbar\omega_L$. The second condition indicates a process corresponding to the electronic transition either from $(0, 0)$ to $(1, 0)$ or from $(0, 1)$ to $(1, 1)$, where only a quasi-electron with energy $\hbar\omega_+$ is created by absorbing the same phonon energy. The third condition indicates a process corresponding to the electronic transition from $(0, 1)$ to $(1, 0)$, where, by absorbing a LO phonon with the same energy, a quasi-electron with $\hbar\omega_+$ is created and a quasi-electron with energy $\hbar\omega_-$ is however annihilated. It is shown from Eq. (5.17) that additional MPR conditions (subsidiary

peaks) appear at $\hbar\omega_+ \pm \hbar\omega_- = \hbar\omega_L$ on both sides of the MPR peaks at $\hbar\omega_+ = \hbar\omega_L$. The origin of the appearance of the subsidiary peaks in the Q2D/Q1D systems is mainly due to the presence of the effective confining potential $m\omega_-^2 Z^2/2$, i.e., ω_- in Eq. (5.17), which is unlike the MPR in a 3D electronic system (where only one resonant peak appears at $\hbar\omega_+ = \hbar\omega_c = \hbar\omega_L$ when $P = 1$. Here P is the difference of Landau-level index.) [2,50-52]. Thus, the appearance of these subsidiary peaks in the MPR lineshape seems to be a characteristic feature in Q2D and Q1D electronic systems. If the frequencies ω_+ and ω_- in Eq. (5.17) are replaced by Ω_1 and Ω_2 , respectively, Eq. (5.17) is reduced to our previous result [25] for a Q1D quantum-wire structure modeled by the same potential wells, which is valid for the strong confinement potentials with respect to the cyclotron resonance frequency. Moreover, if the frequencies ω_+ and ω_- in Eq. (5.17) are replaced by $\sqrt{\omega_1^2 \cos^2 \theta + \omega_2^2 \sin^2 \theta + \omega_c^2}$ and $\sqrt{\omega_1^2 \sin^2 \theta + \omega_2^2 \cos^2 \theta}$, respectively, Eq. (5.17) is reduced to the result of Suzuki et al. [26] for a Q1D quantum-wire structure modeled by the same potential wells, which is valid for weak confinement potentials.

Next, let us pay attention to the shift of the resonant peaks in the conductivity seen in Figs. 9 and 10, which is related to feature (ii). Their shift in the conductivity can be understood in terms of the behaviors of $\hbar\omega_+$ and $\hbar\omega_+ \pm \hbar\omega_-$ in Eq. (5.17) since the quantities $\hbar\omega_+$ and $\hbar\omega_+ \pm \hbar\omega_-$ intercept $\hbar\omega_L$ at the resonant magnetic field values. The quantities $\hbar\omega_+$ and $\hbar\omega_+ \pm \hbar\omega_-$ are mainly influenced by the tilt angle of the applied magnetic field and the strength of the confining potential parameters (ω_1, ω_2) . Therefore, we will concentrate on how MPR peaks change according to these factors.

Figure 11 shows the shift of resonant peaks in the conductivity seen in Fig. 9 as a function of tilt angle θ depending on the confinement conditions given in Fig. 9.

As can be seen from the figure, in the case of $\omega_1 < \omega_2$, the resonant point for

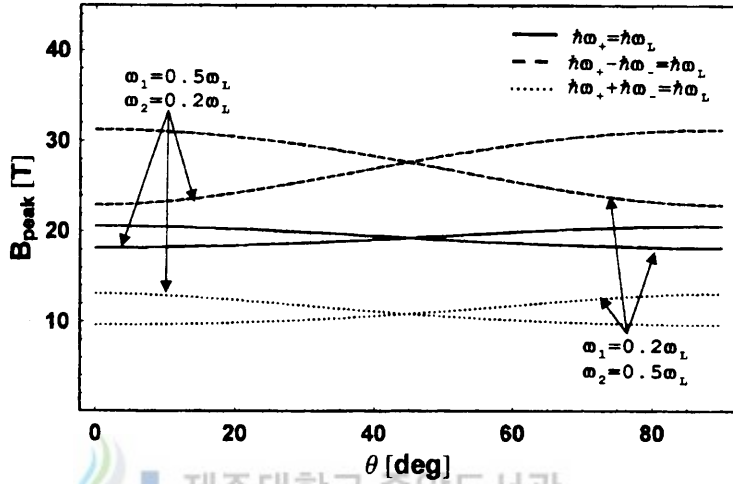


FIG. 11. Tilt angle dependence of the resonant magnetic fields (B_{peak}), viz., the MPR peak positions for $\omega_1 = 0.2\omega_L$, $\omega_2 = 0.5\omega_L$ and $\omega_1 = 0.5\omega_L$, $\omega_2 = 0.2\omega_L$. The solid, dashed, and dotted lines correspond to $\hbar\omega_+ = \hbar\omega_L$, $\hbar\omega_+ - \hbar\omega_- = \hbar\omega_L$, and $\hbar\omega_+ + \hbar\omega_- = \hbar\omega_L$, respectively.

the subsidiary peak in the low field side determined from the condition $\hbar\omega_+ + \hbar\omega_- = \hbar\omega_L$ shifts to the corresponding point in the higher field side. Those resonant points for the central peak given by $\hbar\omega_+ = \hbar\omega_L$ and for the subsidiary peak in the high field side given by $\hbar\omega_+ - \hbar\omega_- = \hbar\omega_L$ shift to the corresponding points in the lower field side, respectively, as the tilt angle is increased, which has an identical behavior as reported by Suzuki et al. [26]. However, the shift of the resonant peaks for $\omega_1 > \omega_2$ is the contrary to that for $\omega_1 < \omega_2$. In other words, for $\omega_1 > \omega_2$, the peak in the low field side of the magnetic field shifts to the lower field side whereas the peaks in the middle and the high field side of the field shift to the higher field side, as the

tilt angle θ of the applied magnetic field is increased. It is noted that our present results do not agree with the experimental results of Brummell et al. [44] for Q2D electronic systems, indicating that all of the MPR peaks shift to the higher B side. As mentioned by Suzuki et al. [26], this disagreement may be due to the fact that their experiment was performed under the magnetic fields up to 10 Tesla whereas our calculations were carried out for the magnetic fields in the region more than 15 Tesla, taking into account two different effective Landau states, $n = 0, 1$ and $l = 0, 1$ only. Since the MPR peak on the lower B side shifts to the higher n or l side even in the present calculations, we might expect the present theory to reproduce their experimental results qualitatively if we take into account the electronic transitions up to the second excited levels and obtain the MPR conditions valid under the magnetic fields up to 10 Tesla. The shift of the MPR peaks in the conductivity seen in Fig. 10 is represented in Fig. 12, as a function of the relative strength of the confining potential parameters for a fixed tilt angle θ . It is shown in the figure that, for a fixed value of ω_1 at a specific angle, the peaks in the low field and the middle field side of the magnetic field shift to the lower field side whereas the peak in the high field side of the magnetic field shifts to the higher field side, as the relative confining potential parameter ω_2/ω_1 is increased, while for a fixed value of ω_2 , all three MPR peaks shift to the low field side of the magnetic field as the relative confining potential parameter ω_1/ω_2 is increased. Our present results for the latter case agree qualitatively with those of Suzuki et al. [26]. Other interesting features of the shift of the MPR peaks are expected according to the relative strength of the electron confinement due to the electrostatic potentials with respect to the magnetic confinement by an applied magnetic field. Their shifts for strong and weak confinement potentials are plotted in Fig. 13, as a function of tilt angle θ , using the

MPR conditions given by Eq. (5.17).

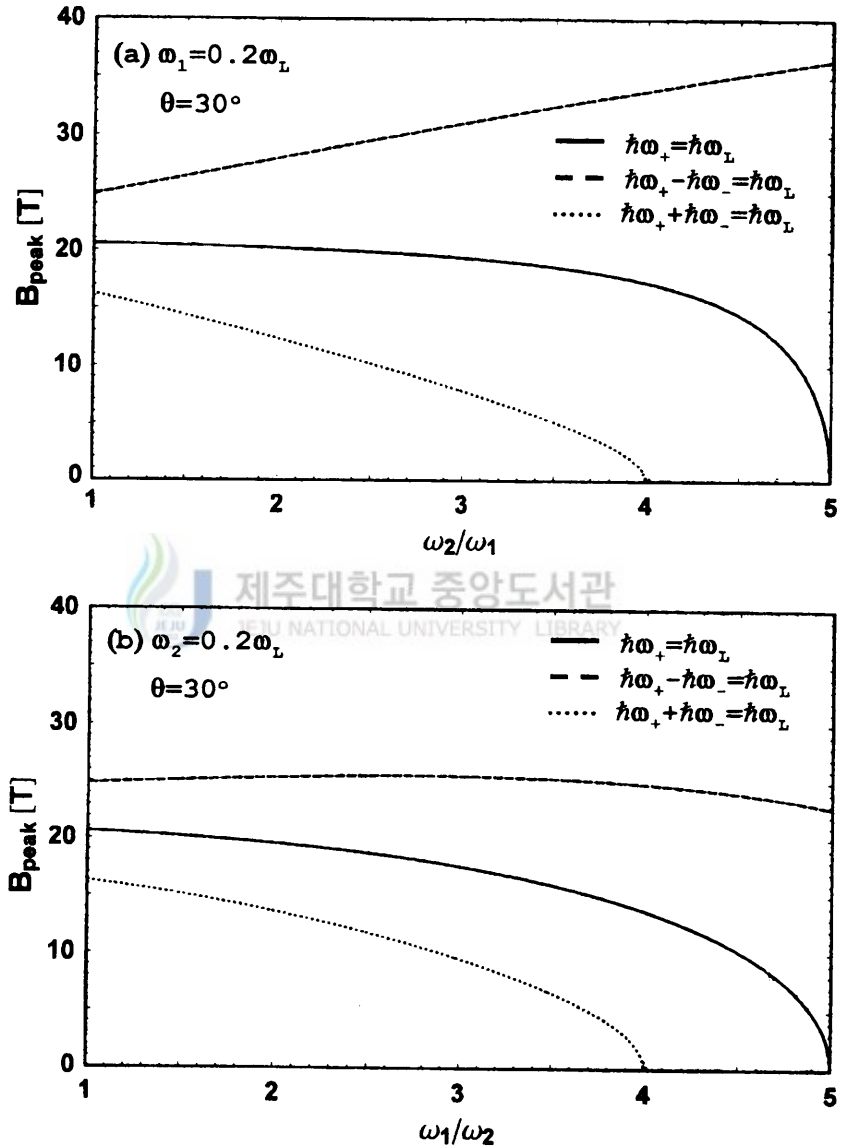


FIG. 12. Relative confining potential strength dependence of the resonant magnetic fields (B_{peak}) at a fixed angle $\theta = 30^\circ$: (a) $\omega_1 = 0.2\omega_L$ and (b) $\omega_2 = 0.2\omega_L$. The solid, dashed, and dotted lines indicate $\hbar\omega_+ = \hbar\omega_L$, $\hbar\omega_+ - \hbar\omega_- = \hbar\omega_L$, and $\hbar\omega_+ + \hbar\omega_- = \hbar\omega_L$, respectively.

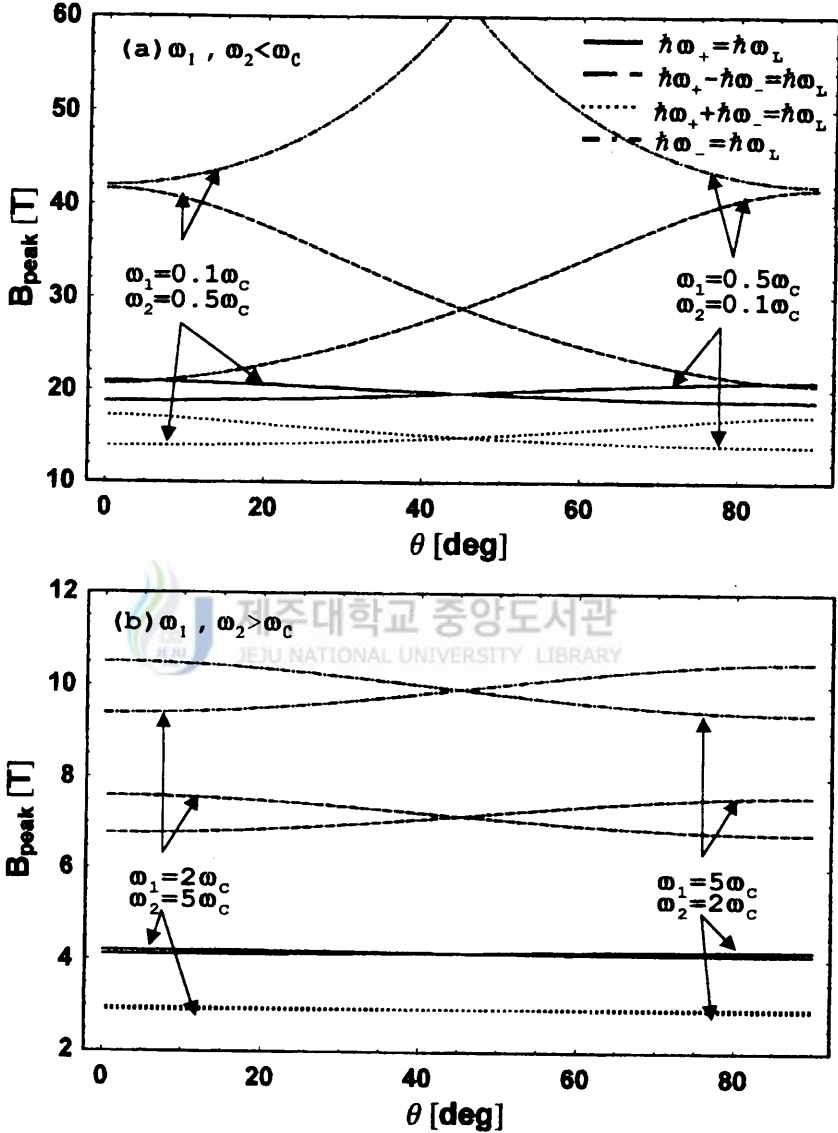


FIG. 13. Tilt angle dependence of the resonant magnetic fields (B_{peak}): (a) $\omega_1, \omega_2 < \omega_c$ and (b) $\omega_1, \omega_2 > \omega_c$, where ω_1 and ω_2 have been taken as $0.1\omega_c$ or $0.5\omega_c$ for weak confinements and as $2\omega_c$ or $5\omega_c$ for strong confinements. The solid, dashed, dotted, and dashed-dotted lines correspond to $\hbar\omega_+ = \hbar\omega_L$, $\hbar\omega_+ - \hbar\omega_- = \hbar\omega_L$, $\hbar\omega_+ + \hbar\omega_- = \hbar\omega_L$, and $\hbar\omega_- = \hbar\omega_L$, respectively.

It is clearly seen in this figure that the resonant peaks for strong confinement appear in the low field side and their angle dependence is small whereas those for weak confinement appear in the high field side and their angle dependence is larger than that for strong confinement. Moreover, the MPR peaks exhibit the similar angle dependence of the shift, as in Fig. 11. Note that, in addition to the MPR conditions in Fig. 11, the shift of resonant peaks given by $\hbar\omega_- = \hbar\omega_L$ appears in terms of given confining potential parameters ω_1 and ω_2 . For direct comparison of the MPR conditions presented by some authors, the shift of resonant peaks given by $\hbar\omega_+ = \hbar\omega_L$ as an example is represented in Fig. 14, as a function of tilt angle according to the confinement strength, where the confining potential parameters were respectively taken as $0.1\omega_c$ and $0.5\omega_c$ for weak confinement and $2\omega_c$ and $5\omega_c$ for strong confinement as a matter of convenience. As shown in Fig. 14, the present results of the angle dependence of the MPR peaks for weak confinement agree well with those of Suzuki et al. [26] for a Q1D quantum-wire structure modeled by the same potential wells, but they do not agree with our previous results [25] whereas the present results for strong confinement agree qualitatively with those of our previous results, but they do not agree with that of Suzuki et al. The difference between the present result and their results [25,26] is due to the neglect of the coupling Hamiltonian term $\sim B_x B_z xz$ in Eq. (5.1) or Eq. (5.2). Let us turn to feature (iii) for the height and width of the MPR peaks seen in Figs. 9 and 10. The height and width of the MPR peaks seen in Figs. 9 and 10 can be explained by Eq. (5.14). The height of MPR peaks are influenced by amplitude factors ($\sqrt{m^*\omega_-/\tilde{m}^*\omega_+\omega_z^2}/\omega_+^3\{1 - \exp[-\beta\hbar\omega_+]\}$) and/or ($\sqrt{m^*\omega_+/\tilde{m}^*\omega_-\omega_z^2}/\omega_-^3\{1 - \exp[-\beta\hbar\omega_-]\}$), in addition to the Lorentzian spectrum function.

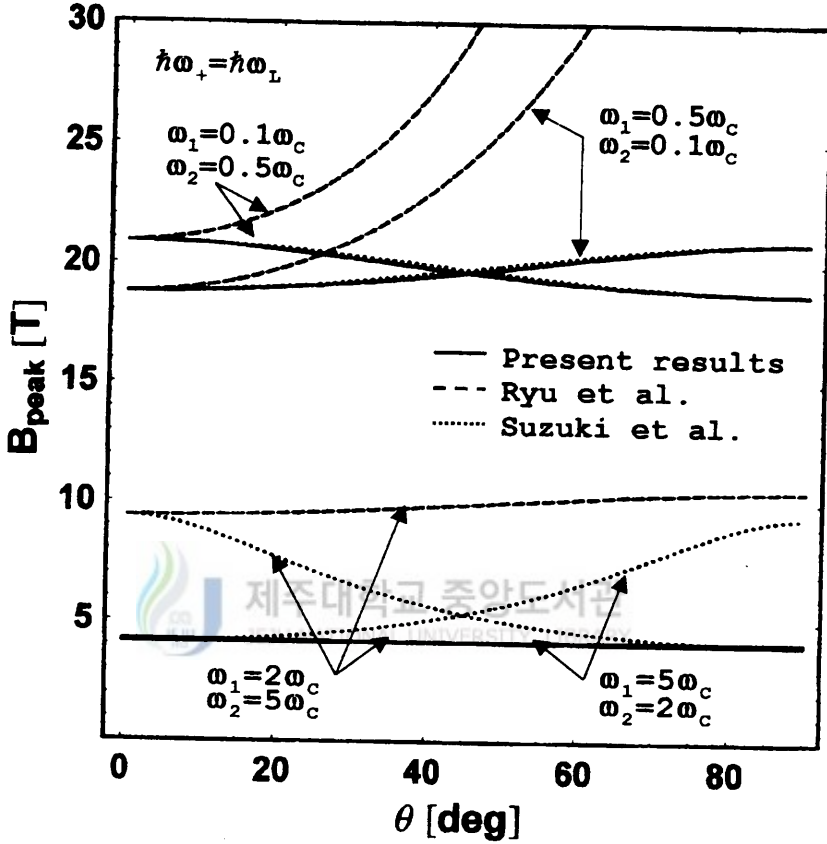


FIG. 14. Comparison with the existing theories for the tilt angle dependence of the resonant magnetic fields (B_{peak}), where ω_1 and ω_2 have been taken as $0.1\omega_c$ or $0.5\omega_c$ for weak confinements and as $2\omega_c$ or $5\omega_c$ for strong confinements. The solid, dashed, and dotted lines indicate the present result for $\hbar\omega_+ = \hbar\omega_L$, Ryu et al.'s theoretical results, and Suzuki et al.'s theoretical results, respectively.

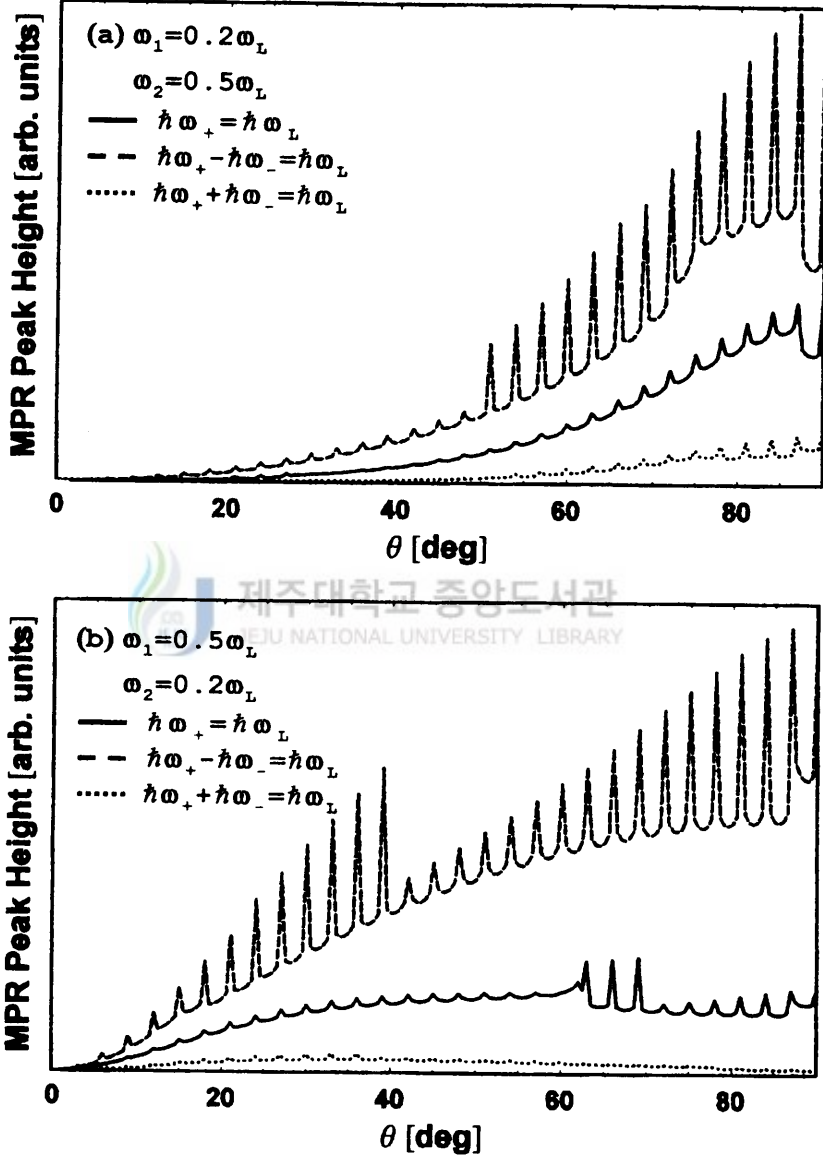


FIG. 15. Tilt angle dependence of the MPR peak heights: (a) $\omega_1 = 0.2\omega_L$, $\omega_2 = 0.5\omega_L$ and (b) $\omega_1 = 0.5\omega_L$, $\omega_2 = 0.2\omega_L$. The solid, dashed, and dotted lines indicate $\hbar\omega_+ = \hbar\omega_L$, $\hbar\omega_+ - \hbar\omega_- = \hbar\omega_L$, and $\hbar\omega_+ + \hbar\omega_- = \hbar\omega_L$, respectively.

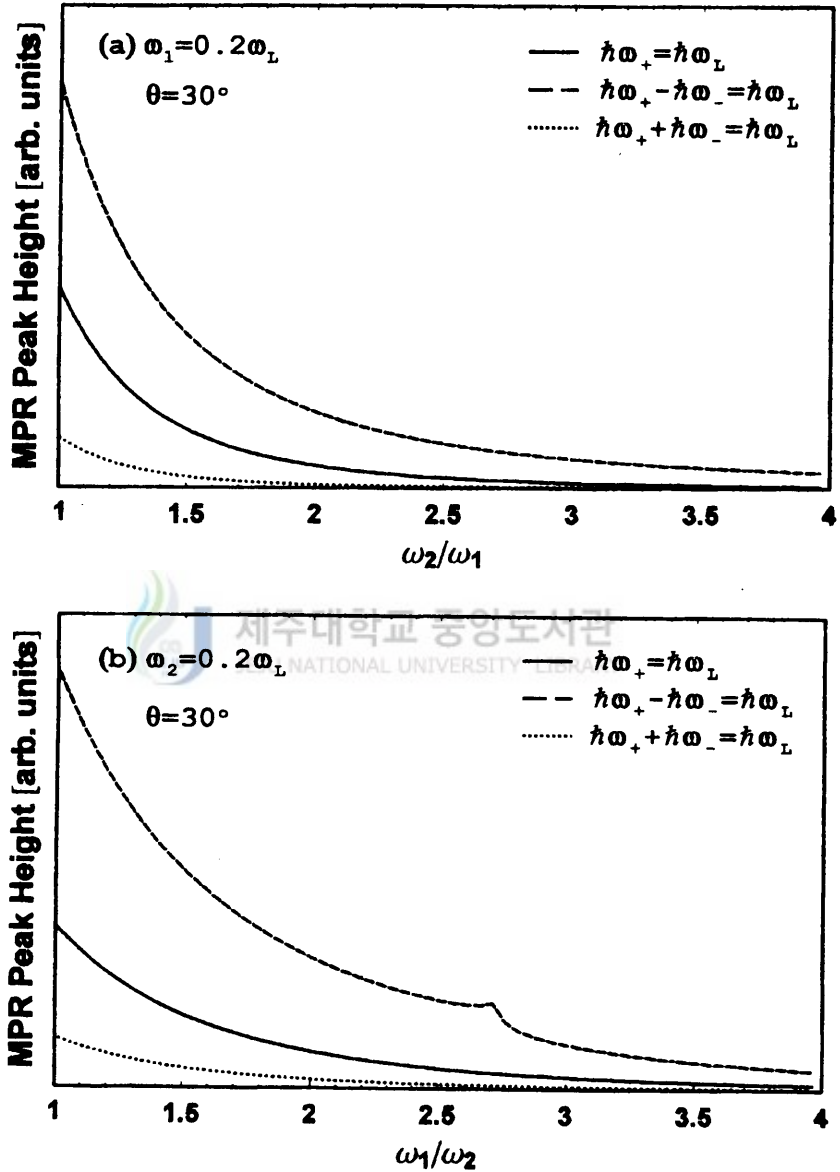


FIG. 16. Relative confining potential strength dependence of the MPR peak heights at a fixed angle $\theta = 30^\circ$: (a) $\omega_1 = 0.2\omega_L$ and (b) $\omega_2 = 0.2\omega_L$. The solid, dashed, and dotted lines indicate $\hbar\omega_+ = \hbar\omega_L$, $\hbar\omega_+ - \hbar\omega_- = \hbar\omega_L$, and $\hbar\omega_+ + \hbar\omega_- = \hbar\omega_L$, respectively.

Figure 15 shows the variation of the heights of MPR peaks in Fig. 9 as a function

of the tilt angle of applied magnetic field. It is seen clearly in this figure that their heights increase as the tilt angle increases. The increase is given in terms of the amplitude factors and it is understood that the spikes on the curve arise from the Lorentzian spectrum function.

The variation of the heights of MPR peaks in Fig. 10 is presented in Fig. 16, as a function of the relative strength of confining potential parameters. The changes of their heights in this figure can be understood by the amplitude factors, as in Fig. 15. When the relative strengths of the confining potential parameters increase, the heights of all three MPR peaks decrease, which agree qualitatively with the experimental results of Brummell et al. [44] for Q2D electronic systems and with the theoretical results of Suzuki et al. [26].

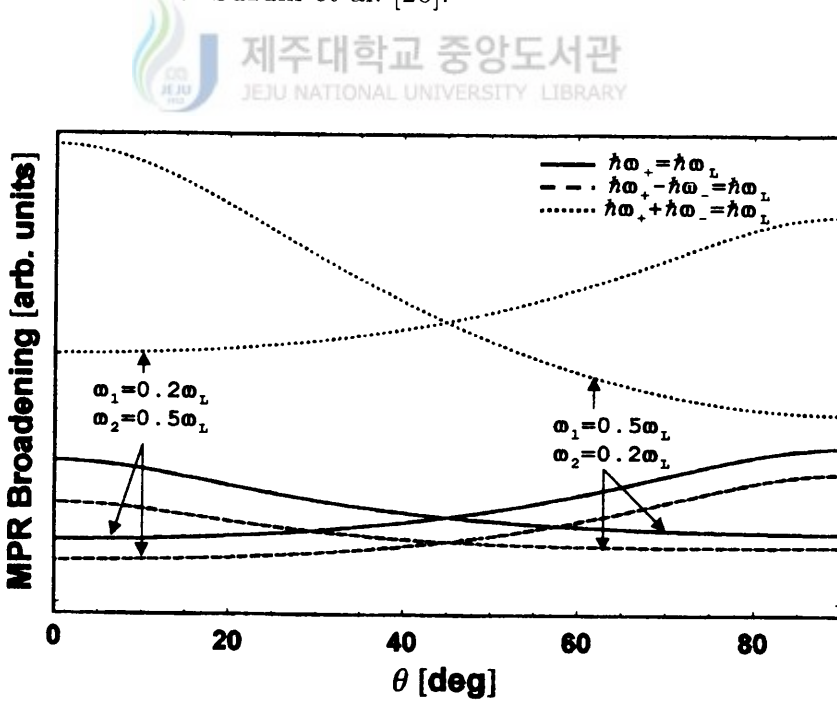


FIG. 17. Tilt angle dependence of the MPR widths for $\omega_1 = 0.2\omega_L$, $\omega_2 = 0.5\omega_L$ and $\omega_1 = 0.5\omega_L$, $\omega_2 = 0.2\omega_L$. The solid, dashed, and dotted lines indicate $\hbar\omega_+ = \hbar\omega_L$, $\hbar\omega_+ - \hbar\omega_- = \hbar\omega_L$, and $\hbar\omega_+ + \hbar\omega_- = \hbar\omega_L$, respectively.

The width of MPR peaks is mainly determined by the Lorentzian spectrum function in Eq. (5.14) through the behavior of $\tilde{\Gamma}$ which appears in terms of the collision broadening due to the electron-phonon interaction and plays the role of the width in the spectral lineshape [53]. Therefore, the width broadening of MPR peaks shown in Figs. 9 and 10 can be understood by the terms including $(\hbar\omega_{\pm})^2$ in Eq. (5.14). Figure 17 shows the variation of the width of MPR peaks as a function of tilt angle. It can be seen from the figure that, as the tilt angle increases, the widths increase for $\omega_1 < \omega_2$, but they decrease for $\omega_1 > \omega_2$. This means that, as the tilt angle increases, the effective confinements for $\omega_1 < \omega_2$ are tighter and electrons are further confined in the narrow region, while for $\omega_1 > \omega_2$ the effective confinements are looser and electrons are confined in the wide region. As a result, for $\omega_1 < \omega_2$, the frequency of collisions between electrons and LO phonons increases and the relaxation time becomes shorter due to the collision (scattering), while for $\omega_1 > \omega_2$, the frequency of collisions decreases and the relaxation time becomes longer. Our theoretical results for the angle dependence of MPR width for $\omega_1 < \omega_2$ agree qualitatively with the experimental results of Brummell et al. [44] for Q2D electronic systems and with the theoretical results of Suzuki et al. [26], which is unlike the case of $\omega_1 > \omega_2$. The variation of the widths of MPR peaks in Fig. 10 is presented in Fig. 18, as a function of the relative strength of confining potential parameters. In this figure, we can see that the width broadening is increasing with increasing one of the confining potential parameters. This means that, as one of the confining potentials increases, the effective confinements are tighter and electrons are further confined in the narrow region, as in the angle dependence of width for $\omega_1 < \omega_2$. Our theoretical results for the strength dependence of confining potential parameters of MPR width agree qualitatively with the experimental results of Brummell et al. [44] for Q2D

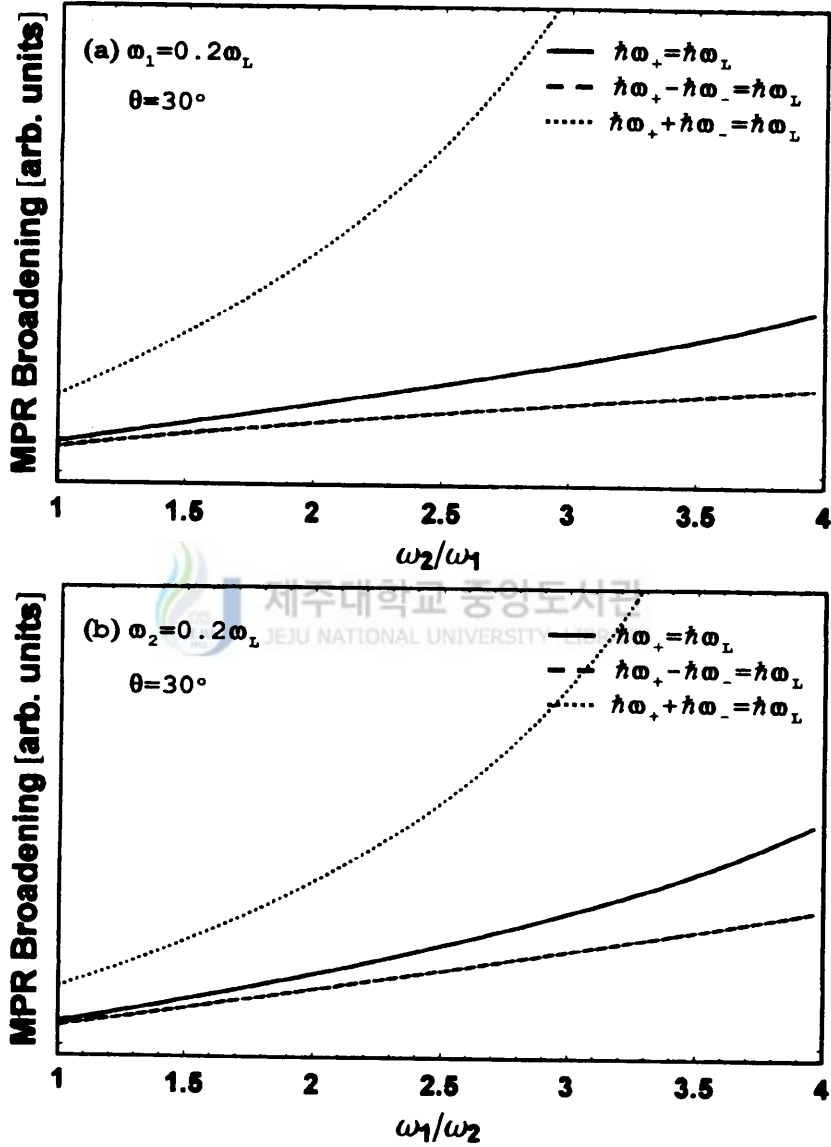


FIG. 18. Relative confining potential strength dependence of the MPR widths at a fixed angle $\theta=30^\circ$: (a) $\omega_1 = 0.2\omega_L$ and (b) $\omega_2 = 0.2\omega_L$. The solid, dashed, and dotted lines indicate $\hbar\omega_+ = \hbar\omega_L$, $\hbar\omega_+ - \hbar\omega_- = \hbar\omega_L$, and $\hbar\omega_+ + \hbar\omega_- = \hbar\omega_L$, respectively.

electronic systems and with the theoretical results of Suzuki et al. [26] for Q1D systems.

Through all figures presented here, we can summarize the physical characteristics of MPR lineshape as follows: for the symmetric quantum wire, there are no shifts in MPR peaks as the tilt angle is increased, while for the asymmetric quantum wire, the shift of MPR peaks and the change of their amplitude and width are sensitive to the tilt angle. The angular dependences of the shift of MPR peaks and of the change of their width for $\omega_1 > \omega_2$ are contrary to those for $\omega_1 < \omega_2$. As one of the confining potential parameters (ω_1 and ω_2) is increased, the MPR peaks in the low field and the middle field side of the magnetic field shift to the lower field side whereas the peak in the high field side of the magnetic field shifts to the higher field side. In addition, the widths of MPR peaks are increased, but their peak heights decrease.

D. Conclusions

In conclusion, we have derived the conductivity σ_{yy} for Q1D electronic systems subjected to crossed electric ($\mathbf{E}||\hat{y}$) and magnetic fields $\mathbf{B} = (B_x, 0, B_z)$, based on a simple model of parabolic confining potentials and obtained the MPR conditions in the quantum limit condition, as a function of the strength (B) and tilt angle (θ) of the applied magnetic field (\mathbf{B}) as well as the strength of the parabolic potential parameters (ω_1 and/or ω_2). With the MPR conditions, we have investigated the physical characteristics of the MPR effects, according to the tilt angle of the applied magnetic field and the relative strength of the confining potential parameters, in such low dimensional systems. In particular, we have studied the qualitative

features of the MPR effects, their physical origin, and the dimensional crossover between Q2D and Q1D systems associated with the confining potential in tilted magnetic fields and compared with the existing theoretical results because we are not aware of any relevant experimental work on MPR on the dependence of the tilted magnetic field on the σ_{yy} for Q1D electronic systems. Some comments related to this work should be made as follows: (i) our theoretical results are based on a model of parabolic confining potential. For usual heterostructures it is well known that the confinement potential in the z -direction is far from being parabolic and is often approximated by a triangular potential [23,35]. For direct comparison with experiments, realistic modeling with the correct confinement potential should be required. We believe however that utilizing a model with a parabolic confinement is good enough to extract the essential physics of MPR effects in Q1D electronic systems in tilted magnetic fields; (ii) the single-particle picture has been used throughout this work, and thus the electron-electron interactions have been ignored. The effect of electron-electron interaction can be taken into account approximately by replacing the electron-phonon interaction included in Eq. (5.9) by a screened electron-phonon interaction $iD\hbar^{1/2}/(2\rho\omega_L V)^{1/2}(1 + \lambda^2(\mathbf{q})/q^2)$ [26], since the inverse screening length $\lambda(\mathbf{q})$ depends on the electron density n_e , which in general depends on temperature T and the magnetic field \mathbf{B} . Therefore, we would expect the screening to be significant only if the electron density n_e exceeds a critical value $n_{cr}(T, \mathbf{B})$. In this case, the effects of electron-electron scattering would be significant, and the relaxation rate will be changed and the MPR lineshape as well as the MPR linewidth would be affected by electron-electron scattering; (iii) any modification of the electron-phonon interaction brought about by the confinement of phonons (we used the interaction for bulk phonons) has not been taken into consideration. A possible influence of the

modification can be included [54] in the electron-phonon interaction in Eq. (5.9). Although such modifications would be expected to affect the MPR lineshape considerably, as in the electron-electron scattering case, they are not expected to change the physical characteristics of MPR effects, such as the appearance of subsidiary MPR peaks and the shift of these MPR peaks.

Despite the above shortcomings of the theory, we believe that the simple model we present captures qualitatively the essential physics on MPR in Q1D electronic systems brought about by the electron confinement due to the electrostatic potentials and the magnetic confinement by tilting a magnetic field. We hope that new experiments will test the validity of our prediction.



VI. MAGNETOPHONON RESONANCES IN THE MINIBAND TRANSPORT IN SEMICONDUCTOR SUPERLATTICES

Since initially predicted by Gurevich and Firsov [2], the MPR effect has been widely studied in bulk semiconductors. The oscillations in the magnetoresistance, caused by resonant scattering of electrons between Landau levels involving an interaction with optical phonons, has been used in order to investigate the electron properties and the lattice vibrations in many polar semiconductor materials. Growth techniques such as molecular-beam epitaxy make it possible to realize high-quality low-dimensional electron gas systems and superlattices. MPR effects in low-dimensional electron-gas systems have received much attention from both experimental and theoretical points of views. Many studies of MPR effects in such low-dimensional electronic systems have been reported [14,20,21,23-26,30,31,35,43,45,55]. However, less work has been done in short-period superlattices. The work related to the MPR in semiconductor superlattices was performed by Noguchi et al. [56] in 1992. They have presented their experimental results of longitudinal magnetoresistance in GaAs/Al_xGa_{1-x}As superlattices under high magnetic fields normal to the interfaces and parallel to the electronic fields. Recently, Gassot et al. [57] have observed the strong oscillations of MPR on the background of the longitudinal magnetoconductance in short-period GaAs/AlAs superlattices resulting from electron interactions with both GaAs and AlAs LO phonons and reported the miniband, electric-field, temperature, and pressure dependences of MPR in superlattices. Although the main physics in the longitudinal magnetic field configuration is clear, many details have not yet been explored and a systematic theoretical treatment is still lacking [58].

The purpose of the present chapter is to present a systematic theoretical analysis of miniband transport of electrons in a GaAs-based superlattice under the influence of a quantized magnetic field normal to the layer plane and to compare our present results with the experimental and theoretical results presented by some authors [56–58]. The investigations are based on the linear response limit of a general expression for the nonlinear dc conductivity developed previously [4], which have been applied to low-dimensional electronic system [25,35] to check the validity of the theory. The longitudinal magnetoconductivities for polar- and nonpolar-optical-phonon scatterings are calculated for superlattices having miniband widths $\Delta = 2.0, 3.6, 5.7, 7.7,$ and 13.64 meV, where the conductivity is inversely proportional to the relaxation rates closely related to the MPR effect. From the relaxation rates, we obtain the MPR condition and the energy range in which the relaxation rates are allowed. As many as 21 Landau levels are included in the calculation of the longitudinal magnetoconductivity. At higher temperature when optical phonon scattering dominates, strong oscillations of the longitudinal magnetoconductivity appear due to the resonant scatterings of electrons between Landau levels by the longitudinal optical (LO) phonons. Our calculated results related to the MPR effects in superlattices are in good qualitative agreement with the experimental and theoretical results presented by some authors [56–58].

The rest of the chapter is organized as follows. In Sec. A, we review a model for superlattices. General formulae of the longitudinal magnetoconductivity σ_{zz} for the superlattice is presented in Sec. B, where the conductivity consists of the usual Drude term arising from the drift motion of electrons. The relaxation rate, which is closely related to the MPR, is evaluated for polar- and nonpolar-optical-phonon scatterings, assuming that the interaction with bulk LO phonon is the dominant

scattering mechanism. Numerical results of magnetoconductivity for the superlattices having various miniband widths are presented in Sec. C. In particular, the MPR conditions for the model systems are given explicitly and the effects of miniband width and the temperature on the MPR are discussed. Here, special attention is given to the behavior of the MPR lineshape, such as the appearance of the plateau scattering between the two MPR peaks, the disappearance of MPR peaks, and a change in MPR amplitude. Concluding remarks will be given in the last section.

A. Electronic Model

We consider a system consisting of N electrons in a superlattice with periodical potential wells of period d_{SL} along the z direction under the influence of longitudinal magnetic field B (in the z direction). The electron energy spectrum of the superlattice still forms minibands in the longitudinal direction due to the superlattice periodic potential. In the superlattice layer ($x - y$ plane), however, it is quantized into Landau levels due to the magnetic field. Considering only the lowest miniband the electron state can be described, in the Landau representation, by the quantum number n of the Landau level, the wave vectors k_x and k_z ($-\pi/d < k_z \leq \pi/d$), and the spin index σ . The electron energy can be written as (we neglect the spin-related energy for simplicity)

$$\varepsilon_n(k_z) = (n + 1/2)\hbar\omega_c + \varepsilon_{\text{SL}}(k_z), \quad n = 0, 1, 2, \dots, \quad (6.1)$$

where n denote the Landau level index resulting from the magnetic confinement, $\omega_c = eB/m^*$ is the cyclotron frequency, m^* is the electron band effective mass in the $x - y$ plane, and $\varepsilon_{\text{SL}}(k_z)$ means the energy dispersion of the lowest superlattice

miniband, which is approximated by cosine shape, under the tight-binding approximation, as

$$\varepsilon_{SL}(k_z) = \frac{\Delta}{2} (1 - \cos k_z d_{SL}), \quad (6.2)$$

where Δ is the miniband width and d_{SL} denotes the periodicity of the potential.

Then, the density of states (DOS) is expressed as

$$D(\varepsilon) = \frac{m^* \omega_c L_x L_y L_z}{\pi^2 \hbar d_{SL}} \sum_n \frac{1}{\sqrt{(\varepsilon - \varepsilon_n)(\varepsilon_n + \Delta - \varepsilon)}} \theta(\varepsilon - \varepsilon_n) \theta(\varepsilon_n + \Delta - \varepsilon). \quad (6.3)$$

This indicates that the DOS has singular points at the top ($\varepsilon = \varepsilon_n + \Delta$) and the bottom ($\varepsilon = \varepsilon_n$) of each miniband as shown in Fig. 19

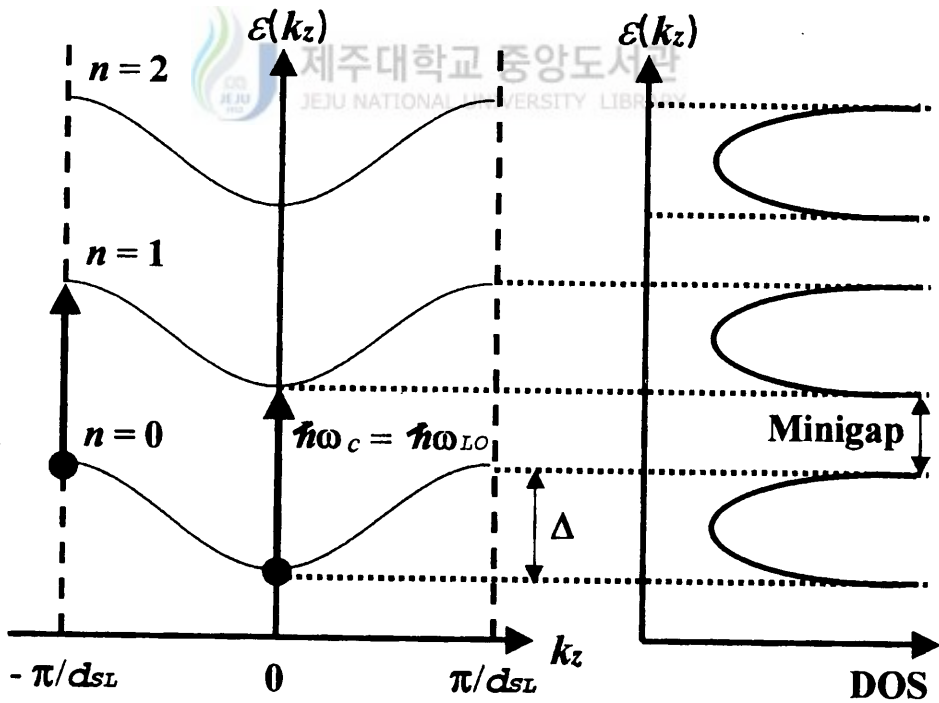


FIG. 19. Dispersion relation and density of states of a superlattice under high magnetic fields and the resonant excitation of electrons by optical phonons. The number n on each miniband is the Landau index.

The electron wave function can be expressed by

$$\langle \mathbf{r} | \lambda \rangle \equiv \langle x, y, z | n, k_x, k_z \rangle = \frac{1}{\sqrt{L_x}} \exp[ik_x x] \chi_{n, k_x}(y) \xi_{k_z}(z), \quad (6.4)$$

where

$$\chi_{n, k_x}(y) = \left(\frac{1}{2^n n! \sqrt{\pi} l_{B+}} \right)^{1/2} \exp \left[-\frac{(y - y_0)^2}{2l_B^2} \right] H_n \left(\frac{y - y_0}{l_B} \right) \quad (6.5)$$

with $l_B = \sqrt{\hbar/m^* \omega_c}$, $y_0 = l_B^2 k_x$, $H_n(x)$ is the harmonic function, and $\xi_{k_z}(z)$ stands for the tight-binding Bloch function in the z direction.

B. Magnetoconductivity Associated with Relaxation Rates

In this section, we want to evaluate an analytical expression of the longitudinal magnetoconductivity σ_{zz} for the model systems described in the previous section, by taking the real part of a general expression for the complex nonlinear dc conductivity $\tilde{\sigma}_{kl}(E)$ ($k, l = x, y, z$) given in Ref. 4 and the linear response limit, i.e., $\lim_{E \rightarrow 0} \text{Re}\{\tilde{\sigma}_{kl}(E)\} \equiv \sigma_{kl}$, the dc linear conductivity σ_{zz} for weak electric fields is given by

$$\begin{aligned} \sigma_{zz} = & \frac{\beta e^2 \Delta^2 d_{\text{SL}}^2 l_B^2}{16\pi^2 \hbar} \sum_n \int_{-\pi/d_{\text{SL}}}^{\pi/d_{\text{SL}}} dk_z \sin^2(k_z d_{\text{SL}}) \\ & \times f(\varepsilon_n(k_z)) [1 - f(\varepsilon_n(k_z))] \tilde{\Gamma}^{-1}(n, k_x, k_z; n, k_x, k_z) \end{aligned} \quad (6.6)$$

for the shift zero in the spectral line shape, where $\beta = 1/k_B T$ with k_B being Boltzmann constant and T temperature. Also, n indicates the quantum state, \hbar is Plank constant divided by 2π , $f(\varepsilon_n(k_z))$ is a Fermi–Dirac distribution function associated with the eigenstate $|n, k_x, k_z\rangle$ of Eq. (6.4) and the energy $\varepsilon_n(k_z)$ of Eq. (6.1), and $-e (< 0)$ is the electron charge. The quantity $\tilde{\Gamma}$ given in Eq. (6.6), which appears

in terms of the collision broadening due to the electron–background (phonon or impurity) interaction, play the role of the relaxation rate in the spectral line shape. To obtain the longitudinal magnetoconductivity σ_{zz} of Eq. (6.6) for the model systems, we used the matrix elements of the z -component single-electron current operator $|\langle k_z, k_x, n | j_z | n', k'_x, k'_z \rangle|^2$ to be

$$|\langle k_z, k_x, n | j_z | n', k'_x, k'_z \rangle|^2 = (e\Delta d_{\text{SL}} \sin(k_z d_{\text{SL}})/2\hbar)^2 \delta_{nn'} \delta_{k_x k'_x} \delta_{k_z k'_z}, \quad (6.7)$$

since the matrix element with respect to the current operator in Eq. (6.7) is directly proportional to the dc magnetoconductivity, where the Kronecker symbols ($\delta_{n'n}$, $\delta_{k_x k'_x}$, $\delta_{k_z k'_z}$) denote the selection rules, which arise during the integration of the matrix elements with respect to each direction. We also replaced summations with respect to k_x and k_z in \sum_{n, k_x, k_z} by the following relation [23,26]:

$$\sum_{k_x, k_z} (\dots) \rightarrow (L_x L_z / 4\pi^2) \int_{-m^* \omega_c L_y / 2\hbar}^{m^* \omega_c L_y / 2\hbar} dk_x \int_{-\pi/d_{\text{SL}}}^{\pi/d_{\text{SL}}} dk_z (\dots). \quad (6.8)$$

In addition, to express the dc magnetoconductivity of Eq. (6.6) in simpler forms, we assume that the f 's in Eq. (6.6) are replaced by the Boltzmann distribution function for nondegenerate semiconductors [23,26], i.e., $f(\varepsilon_n(k_z)) \approx \exp[\beta(E_F - \varepsilon_n(k_z))]$, where E_F denotes the Fermi energy given by $E_F = (1/\beta) \ln \{4\pi \hbar n_e d_{\text{SL}} \sinh(\beta \hbar \omega_c / 2) / [m^* \omega_c \exp(-\beta \Delta / 2) I_0(\beta \Delta / 2)]\}$. Here $n_e = N_e / V$ denotes the electron density and $I_0(x)$ denotes the modified Bessel function [15]. As shown in Eq. (6.6), the electronic transport properties (e.g., electronic relaxation processes, magnetophonon resonances, etc.) in the superlattice can be studied by examining the behavior of $\tilde{\Gamma}$ as a function of the relevant physical parameters introduced in the theory. In the following, we shall analyze the relaxation rates in details in order to get insight into MPR effects in the model system of the superlattices.

An analytical expression of the relaxation rate in the lowest-order approximation for the weak electron-phonon interaction and in the limit of weak electric fields can be evaluated from the general expression of the electric-field dependent relaxation rate given by Eq. (4.39) of Ref. 4 as follows:

$$\begin{aligned}
\tilde{\Gamma}(n, k_x, k_z; n, k_x, k_z) = & \pi \sum_{\mathbf{q}} \sum_{n' \neq n} |C(\mathbf{q})|^2 |J_{nn'}(u)|^2 \{(n_{\mathbf{q}} + 1) \\
& \times \delta[(n - n')\hbar\omega_c - \frac{\Delta}{2}(\cos k_z d_{\text{SL}} - \cos(k_z - q_z) d_{\text{SL}}) - \hbar\omega_{\mathbf{q}}] \\
& + n_{\mathbf{q}} \delta[(n - n')\hbar\omega_c - \frac{\Delta}{2}(\cos k_z d_{\text{SL}} - \cos(k_z + q_z) d_{\text{SL}}) + \hbar\omega_{\mathbf{q}}]\} \\
& + \pi \sum_{\mathbf{q}} \sum_{n' \neq n} |C(\mathbf{q})|^2 |J_{nn'}(u)|^2 \{(n_{\mathbf{q}} + 1) \\
& \times \delta[(n' - n)\hbar\omega_c - \frac{\Delta}{2}(\cos(k_z + q_z) d_{\text{SL}} - \cos k_z d_{\text{SL}}) + \hbar\omega_{\mathbf{q}}] \\
& + n_{\mathbf{q}} \delta[(n' - n)\hbar\omega_c - \frac{\Delta}{2}(\cos(k_z - q_z) d_{\text{SL}} - \cos k_z d_{\text{SL}}) - \hbar\omega_{\mathbf{q}}]\},
\end{aligned} \tag{6.9}$$

where n' indicates the intermediate localized Landau level indices, $n_{\mathbf{q}}$ is the optical phonon distribution function given by $n_{\mathbf{q}} = [\exp(\beta\hbar\omega_{\mathbf{q}}) - 1]^{-1}$, $C(\mathbf{q})$ is the Fourier transform of the electron-phonon interaction potential, and

$$|J_{nn'}(u)|^2 = \frac{n_{<}!}{n_{>}!} e^{-u} u^{\Delta n} [L_{n_{>}}^{\Delta n}(u)]^2. \tag{6.10}$$

Here $n_{<} = \min\{n, n'\}$, $n_{>} = \max\{n, n'\}$, $u = l_B^2 q_{\perp}^2 / 2$ with $q_{\perp}^2 = q_x^2 + q_y^2$, and $L_{n_{<}}^{\Delta n}(u)$ is an associated Laguerre polynomial [15] with $\Delta n = n_{>} - n_{<}$. The δ functions in Eq. (6.9) express the law of energy conservation in one-phonon collision (absorption and emission) processes. The strict energy-conserving δ functions in Eq. (6.9) imply that when the electron undergoes a collision by absorbing energy from the field, its energy can only change by an amount equal to the energy of a phonon involved in the transitions. This in fact leads to MPR effects due to the Landau levels.

To calculate the relaxation rates $\tilde{\Gamma}$ of Eq. (6.9) for electron-phonon interactions, we consider the Fourier component of the interaction potentials [20,25,26,55] for non-polar optical phonon scattering given by $|C(q)|^2 = D/V$ with D being the constant of the nonpolar interaction and for polar-LO-phonon scattering given by $|C(q)|^2 = D'/Vq^2$ with D' being the constant of the polar interaction, where the assumption that the phonons are dispersionless (i.e., $\hbar\omega_{\bar{q}} \approx \hbar\omega_L \approx \text{constant}$, where ω_L is the optical phonon frequency) and bulk (i.e., three-dimensional) was made. Then, the relaxation rates associated with the electronic transition between the states $|n, k_x, k_z\rangle$ and $|n, k_x, k_z\rangle$ can be expressed for non-polar and polar optical phonon scatterings, respectively, by

$$\tilde{\Gamma}(n, k_x, k_z; n, k_x, k_z) = \frac{2D}{\pi l_B^2 \Delta d_{\text{SL}}} \sum_{n' \neq n} \sum_{\pm} (n_0 + 1/2 \pm 1/2) \frac{\theta(1 - 4\Theta_{\pm}^2(k_z)/\Delta^2)}{\sqrt{1 - 4\Theta_{\pm}^2(k_z)/\Delta^2}}, \quad (6.11a)$$

$$\begin{aligned} \tilde{\Gamma}(n, k_x, k_z; n, k_x, k_z) &= \frac{2D'}{\pi \Delta d_{\text{SL}}} \sum_{n' \neq n} \sum_{\pm} ((n_0 + 1/2 \pm 1/2) \\ &\times \frac{K_{\pm}(n, n'; k_z)}{\sqrt{1 - \frac{4}{\Delta^2} \Theta_{\pm}^2(k_z)}} \theta\left(1 - \frac{4}{\Delta^2} \Theta_{\pm}^2(k_z)\right), \end{aligned} \quad (6.11b)$$

where n_0 is the optical-phonon distribution function given by $n_{\mathbf{q}} = [\exp(\beta\hbar\omega_{\mathbf{q}}) - 1]^{-1}$ with $\omega_{\mathbf{q}} = \omega_{LO}$, the symbol \pm in the summation indicates the phonon emission and absorption processes, respectively, $\theta(x)$ is the Heaviside step function defined by $\theta(x) = 1$ for $x \geq 0$ and 0 for $x < 0$,

$$\Theta_{\pm}(k_z) = (n' - n)\hbar\omega_c + \frac{\Delta}{2} \cos k_z d_{\text{SL}} \pm \hbar\omega_{LO}, \quad (6.12)$$

and

$$K_{\pm}(n, n'; t) = \frac{1}{2} \int_0^{\infty} du_{\perp} |J_{n, n'}(u_{\perp})|^2 \frac{1}{u_{\perp} + a_{\pm}^2}$$

$$\begin{aligned}
&= \frac{e^{a^2}}{2(\alpha + n_{<})!} \sum_{k=0}^{\infty} \sum_{m=0}^{2k} \frac{(2n_{<} - 2k)!(2k)!}{(n_{<} - k)!} \\
&\quad \times \frac{(-1)^m 2^m (2k + 2\alpha)!(\alpha + m)!}{(2k - m)!(2\alpha + m)!m!} \Gamma(-\alpha - m, a_{\pm}^2). \quad (6.13)
\end{aligned}$$

Here $a_{\pm}^2 = l_B^2 (k_z - \cos^{-1}(2\Theta_{\pm}(t)/\Delta)/d_{\text{SL}})^2/2$ with $t = k_z d_{\text{SL}}$, $\alpha = n_{>} - n_{<}$, and $\Gamma(a, x)$ is the incomplete gamma function [15] defined by $\Gamma(a, x) = \int_x^{\infty} e^{-t} t^{a-1} dt$. In order to obtain Eq. (6.11), we transformed the sum over \mathbf{q} in Eq. (6.9) into an integral form in the usual way as $\sum_{\mathbf{q}} \rightarrow \frac{V}{(2\pi)^3} \int_{-\infty}^{\infty} \int_{-\infty}^{\infty} \int_{-\pi/d}^{\pi/d} dq_x dq_y dq_z$ and used the following property of Dirac delta function: $\delta[f(x)] = \sum_i \delta[x - x_i]/|f'(x_i)|$ with x_i being the roots of $f(x)$. In addition, we utilized the following relation in doing the integral over q_x and q_y : $\int_0^{\infty} \sqrt{u} |J_{n'n}(u)|^2 du = 1/l_B^2$, to obtain Eq. (6.11a). It is clearly seen from Eq. (6.11) that the relaxation rates diverge whenever the conditions $1 - 4\Theta_{\pm}^2(k_z)/\Delta^2 = 0$ and the arguments $a_{\pm}^2 = 0$ in the incomplete gamma function $\Gamma(-\alpha - m, a_{\pm}^2)$ (or $K_{\pm}(n, n'; t)$) are satisfied. From these conditions, the relaxation rates (and hence, the longitudinal magnetoconductivities σ_{zz}) for both non-polar-LO-phonon and polar-LO-phonon scattering show the same resonant behaviors at $N\hbar\omega_c = \hbar\omega_{LO}$ ($N \equiv n' - n = 1, 2, 3, \dots$). When the MPR conditions are satisfied, in the course of scattering events, the electrons in the Landau levels specified by the level index (n) could make transitions to one of the Landau levels (n') by absorbing a LO-phonon energy $\hbar\omega_{LO}$. In addition, from the fact that $1 - 4\Theta_{\pm}^2(k_z)/\Delta^2$ are real and positive, we can obtain an energy range in which the relaxation rates are allowed under the following condition:

$$\hbar\omega_{LO} - \Delta < N\hbar\omega_c < \hbar\omega_{LO} + \Delta, \quad (6.14)$$

which is identical with the results of Noguchi et al. [56] and Gassot et al. [57] obtained from the dispersion relation and the density of states of a superlattice under high

magnetic fields and from the resonant excitation of electrons by optical phonons. It is to be noted that scatterings with optical modes is possible only within the energy range and the condition is closely related to the miniband dependence of the MPR spectra and the plateau feature, and that the energy range in which scatterings with optical modes are possible is very sensitive to the miniband width and the strength of applied magnetic fields. Equation (6.6), together with Eq. (6.11), is the basic equation for the MPR spectral lineshape of superlattices, which enables us to analyze MPR effects in the superlattices under magnetic fields.

C. Numerical Results and Discussion

In this section we present the numerical results of the longitudinal magnetoconductivity formula σ_{zz} in Eq. (6.6), together with Eq. (6.11), which is related to the MPR for the superlattices based on the model described in Sec. A. Here, special attention is given to the behavior of the MPR lineshape, such as the appearance of the plateau scattering between the two MPR peaks, the disappearance of MPR peaks, and a change in MPR amplitude. For our numerical results of Eq. (6.6), we consider the electronic systems in the superlattice with effective mass $m^* = 0.067 m_0$ with m_0 being the electron rest mass and LO-phonon energy $\hbar\omega_{LO} = 36.6$ meV. The electron density and the period of superlattice are, respectively, taken to be $4.2 \times 10^{-16} \text{cm}^{-3}$ and 9.93 nm in this calculation. In addition, as many as 21 Landau levels are included in the calculation of the longitudinal magnetoconductivity.

Figure 20 shows the miniband dependence of the longitudinal magnetoconductivities σ_{zz} as a function of magnetic field B at $T = 240$ K, where various miniband widths ranging from 2.0 meV to 13.64 meV are taken, in order to investigate the

MPR effect depending on the miniband parameters. The inset indicates the enlarged part of the magnetoconductivity for low magnetic-field side. In these figures, we can see the following features for superlattices: (i) as the difference of Landau level indices is increased, the MPR peak positions are shifted to lower magnetic field side, (ii) the number of peaks vary with the miniband width, and (iii) the plateaulike features and the heights between neighboring MPR peaks are very sensitive to the miniband width Δ . Feature (i) can be readily understood from the conditions for MPR giving the peak positions (i.e., resonant magnetic fields) in the spectral line-shape, which is mainly determined by the conditions $1 - 4\Theta_{\pm}^2(k_z)/\Delta^2 = 0$ and the arguments $a_{\pm}^2 = 0$ in Eqs. (6.11) and (6.13). The resonant behaviors are actually given by $N\hbar\omega_c = \hbar\omega_{LO}$ ($N \equiv n' - n = 1, 2, 3, \dots$). Therefore, the resonant magnetic field is decreased since the $N\omega_c$ is constant if the difference of the Landau level indices is increased. The MPR peak positions for the $N = 1$ and $N = 2$ resonances shown in Fig. 20, which are given by 10.50 and 21 T, respectively, are in good agreement with Noguchi et al.'s prediction [56]. According to their experimental results, two large peaks are observed at 12 and 22 T in the superlattice having the miniband width $\Delta = 20.2$ meV. Let us pay attention to the number of the resonant peaks in the conductivity seen in Fig. 20, which is related to feature (ii). The change of the number of the resonant peaks in the conductivity depending on the miniband width can be understood in terms of the dispersion relation and the density of states of a superlattice shown in Fig. 19, together with Eq. (6.14). In the case where the miniband width and the applied magnetic field are large enough and the minigap between two minibands exists, DOS in each miniband is not overlapped each other. However, if the strength of applied magnetic field is decreased, the energy separation between two Landau levels will be decreased. As a consequence, the minigap

between two neighboring minibands will disappear and DOS in each miniband can be overlapped.

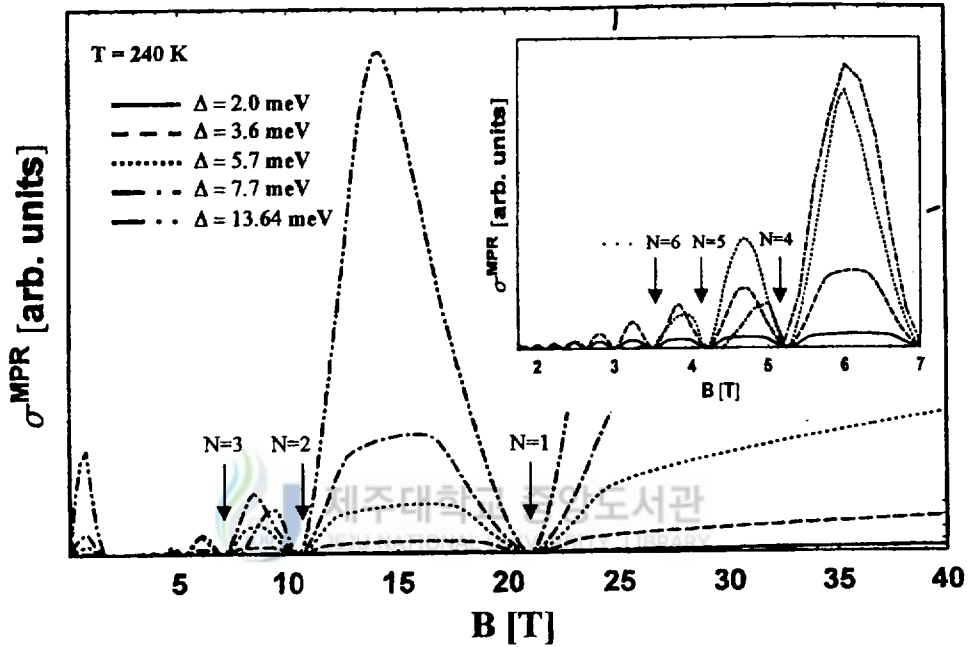


FIG. 20. Miniband dependence of the magnetoconductivity (σ_{zz}) as a function of applied magnetic field at $T=240$ K. The inset indicates the enlarged part of the magnetoconductivity for low magnetic fields. The solid, dashed, dotted, dashed-dotted, and dashed-double dotted lines are for $\Delta=2.0$ meV, 3.6 meV, 5.7 meV, 7.7 meV, and 13.64 meV, respectively.

When DOS in each miniband are overlapped, a lot of electron-LO phonon interactions are expected under the condition of Eq. (6.14). Actually, the magnetoconductivity will be disappeared as shown in the figure. On the contrary, if the width of the miniband is sufficiently small, the minigap between two neighboring minibands is very large under the high magnetic fields. In this case, the minigap between two

minibands is very large and DOS in each miniband will be never overlapped each other. The remarkable thing is that DOS in each miniband begins to be overlapped in lower magnetic fields, compared to the large miniband case. Thus, when the miniband width is small, a lot of peaks appear, whereas the number of peaks decrease with increasing the miniband width, as shown in Fig. 20. This feature that the width of the MPR is better resolved as the miniband width decreases can be also explained by Eq. (6.14), as Noguchi et al. [56] and Gassot et al. [57] did in details. All these features are in good qualitative agreement with the experimental results of Noguchi et al. [56] and Gassot et al. [57] and the theoretical results of Shu et al. [58].

Next, let us turn to feature (iii) for the appearance of the plateau and the heights between neighboring MPR peaks according to the miniband width. The appearance of the plateau between the $N = 1$ and $N = 2$ resonance peaks shown in Fig. 20 has been well explained by Noguchi et al. [56], by using the dispersion relation and the density of states of a superlattice shown in Fig. 19. As pointed out by Noguchi et al., if a SL with sufficiently narrow miniband is placed in high magnetic fields ($\hbar\omega_c > \Delta$), the real minigap will be formed between the adjacent minibands. Particularly when the condition

$$\frac{\hbar\omega_{LO} + \Delta}{2} < \hbar\omega_c < \hbar\omega_{LO} - \Delta \quad (6.15)$$

is satisfied, final states are completely inside the minigap and the optical phonon scattering in this region is effectively inhibited. This explains why the plateau scattering appears between the two peaks. The plateau features appear at lower miniband width as the value of N increases, i.e., the resonance magnetic field decreases, which can be understood in terms of Eq. (6.15).

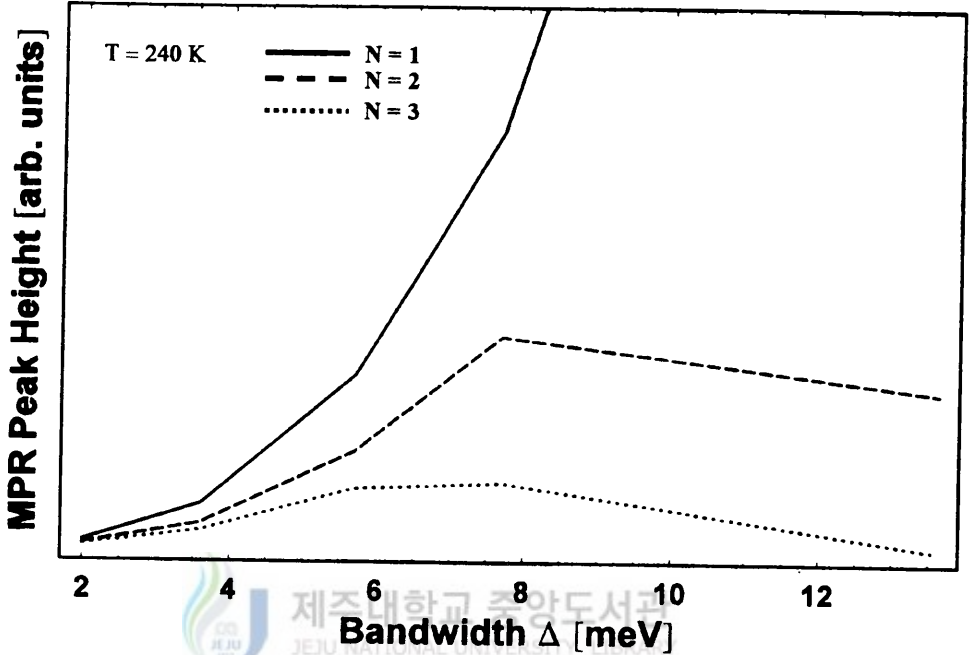


FIG. 21. Miniband dependence of the height of MPR peaks at $T=240$ K. The solid, dashed, and dotted lines indicate the $N = 1$, $N = 2$, and $N = 3$ resonance peaks, respectively.

The variation of the height of MPR peaks are shown in Fig. 21, as a function of the miniband width at $T = 240$ K. The $N = 1$ resonance peak increases with increasing the miniband width, whereas the $N = 2$ and $N = 3$ resonance peaks show complicate behaviors: they increase with the increase of the miniband width and then they decrease at a specific miniband width. Our results for the $N = 1$ and $N = 2$ resonance peaks are in good qualitative agreement with the experimental results of Noguchi et al. [56] and Gassot et al. [57]. For the $N = 3$ resonance peak, our result is somewhat different from Gassot et al.'s experimental result in which the $N = 3$ resonance peak decreases. Our results are also in good qualitative agreement

with Shu et al.'s theoretical results [58] for the $N = 2$ and $N = 3$ resonance peaks, unlike the $N = 1$ resonance peak case. The amplitude of the $N = 2$ resonance peak as compared to the $N = 1$ peak get smaller with increasing miniband width. This can be understood by considering the relaxation rate, as pointed out by Noguchi et al.; when the miniband is wide (~ 20 meV) and the Landau energy $\hbar\omega_c$ is small (≤ 20 meV at 12 T), the minigap shown in Fig. 19 disappears. In such a condition the resonant feature of the relaxation rate becomes weak since the DOS of each miniband broadens and overlaps, resulting in the reduction of its peaked feature. Hence, the discrete features of DOS are essential to observe clear resonance peaks. These features are in good qualitative agreement with the experimental results of Noguchi et al. [56] and the theoretical results of Shu et al. [58], but they is different from Gassot et al.'s experimental results [57].

To understand the effect of temperature on MPR, we plotted the spectral line-shapes of σ_{zz} for a superlattice in Fig. 22, as a function of magnetic field B for temperatures ranging from 140 K to 390 K at a fixed miniband width Δ of 3.6 meV. This figure has two important features. One is that when the sample temperature increases, the magnetoconductivity decreases, which is in good qualitative agreement with the experimental results of Noguchi et al. and Gassot et al. and the theoretical results of Shu et al. The other is that when the temperature increases, the heights of MPR peaks in magnetoconductivity decreases. The temperature dependence of the heights of MPR peaks between two neighboring MPR peak positions is shown in Fig. 23 for three different positions at the miniband width $\Delta = 3.6$ meV. It is clearly seen from the figures that our results for temperatures ranging from 140 K to 390 K are in good qualitative agreement with the experimental results of Gassot et al. for above 125 K. The reason why the amplitude of these oscillations decreases at

high temperature was explained by Gassot et al., which is due to three factors: the increase of the linewidth of the Landau levels due to thermal broadening, the shift of the electron distribution towards the center of the Brillouin zone, and intraminiband scattering of the distribution function around the quasi Fermi level. However, it is reported that there exist some discrepancy between two experimental results [56,57] on the temperature dependence of the heights of MPR peaks.

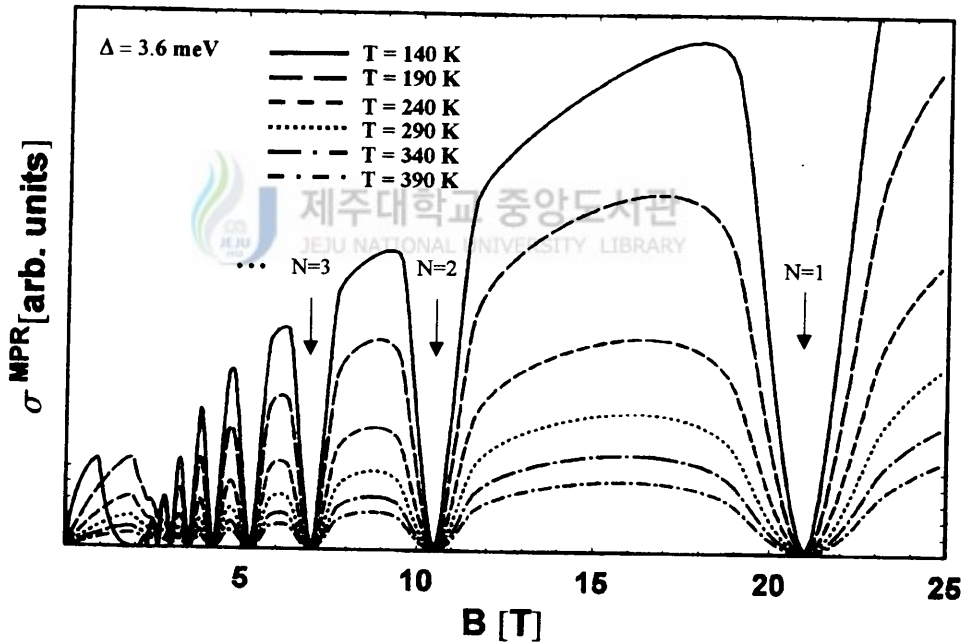


FIG. 22. Temperature dependence of the magnetoconductivity (σ_{zz}) as a function of applied magnetic field at a fixed miniband width of $\Delta=3.6$ meV. The solid, long dashed, short dashed, dotted, long dashed-dotted, and short dashed-dotted lines are for $T=140$ K, 190 K, 240 K, 290 K, 340 K, and 390 K, respectively.

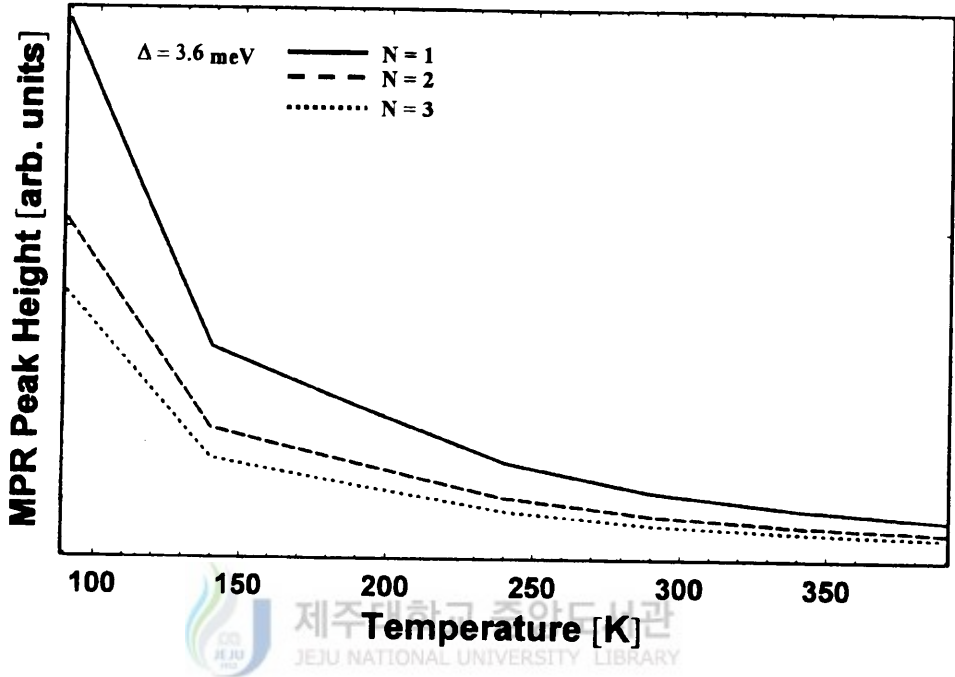


FIG. 23. Temperature dependence of the height of MPR peaks at a fixed miniband of $\Delta=3.6$ meV. The solid, dashed, and dotted lines indicate the $N = 1$, $N = 2$, and $N = 3$ resonance peaks, respectively.

According to the Gassot et al.'s experimental results [57], the height increases as the sample temperature increases until 125 K and then decreases, whereas Noguchi et al. observed a monotonic increase in amplitude of the MPR in the magnetoresistivity with increasing temperature and Shu et al. presented the theoretical results which is in qualitative agreement with Noguchi et al.'s experimental results although there is discrepancy between Noguchi et al.'s experimental results [56] and Shu et al.'s theoretical results [58] below 155 K. Actually, our results contrast with Noguchi et al.'s and Shu et al.'s results, reporting that the amplitude of the MPR in the magnetoresistivity monotonically increase with increasing temperature, and Gassot

et al.'s experimental results ranging from 4.2 K to 125 K. The reason is not clear at this moment. This discrepancy may be ascribed to the acoustic-phonon-scattering, the electron-impurity scattering, and the electron-electron scattering processes. This point needs further investigation.

D. Conclusions

In conclusion, we have derived the longitudinal magnetoconductivity σ_{zz} for a simple model of superlattices and obtained the MPR conditions and an energy range in which the relaxation rates are allowed. With the MPR conditions and the obtained energy range, we have investigated the physical characteristics of the MPR effects in such superlattice systems. In particular, we have studied the qualitative features of the MPR effects, according to the miniband width and the temperature parameters and compared with the existing experimental [56,57] and theoretical [58] results. Some comments related to this work should be made as follows: the single-particle picture has been used throughout this work, and thus the electron-electron interactions have been ignored. The effect of electron-electron interaction can be taken into account approximately by replacing the electron-phonon interaction $C(\mathbf{q})$ by a screened electron-phonon interaction $C(\mathbf{q}) = iD\hbar^{1/2}/(2\rho\omega_L V)^{1/2}(1 + \lambda^2(\mathbf{q})/q^2)$ [26], since the inverse screening length $\lambda(\mathbf{q})$ depends on the electron density n_e , which in general depends on temperature T and the magnetic field \mathbf{B} . Therefore, we would expect the screening to be significant only if the electron density n_e exceeds a critical value $n_{cr}(T, \mathbf{B})$. In this case, the effects of electron-electron scattering would be significant, and the relaxation rate will be changed and the temperature dependence of the height of MPR peaks would be affected by electron-electron scattering.

Despite the above shortcomings of the theory, we believe that our results presented here make it possible to understand qualitatively the essential physics on MPR in superlattices.



VII. EXACT SOLUTION OF THE ELECTROSTATIC PROBLEM FOR A SINGLE ELECTRON DUAL-JUNCTION-ARRAY TRAP

Since Likharev's report [59] on single electron tunneling devices whose fundamental operation principle is based on the Coulomb blockade effect, a lot of work have been made [5,6,60–68] on the physics of SET phenomena and on the wide variety of SET device applications. One of the most significant SET systems is the single-electron “trap”, which is comprised of a junction array and a capacitor as shown in Fig.24(a). It serves as a memory cell by holding an electron or a hole on the trap, i.e., “0” state for no extra charge on the trap and “1” state for an extra charge on the trap. Numerous papers have already published [6,62–65,68] on this subject. Recently, Amakawa, Fujishima, and Hoh [66] presented a more complicate single electron memory circuit, single electron dual-junction-array trap, which is composed of two capacitively-coupled normal traps as shown in Fig. 24(b). In particular, they studied the charge transport in this system by using computer simulation taking into account cotunneling, based on the tunneling rate obtained from the approximation proposed by Fonseca et al. [65]. When an excess electron is placed on one of the islands in the left-hand array, it is energetically favorable if there is a hole on the adjacent island in the right-handed array. Thus, an electron and a hole tend to pair and move together along the single electron dual-junction array. According to their results [66], the lifetime of the electron-hole pair (“exciton”) is longer than that of the single electron when the coupling capacitance C_c is large. This means that the binding energy of the electron-hole pair (“exciton”) is so large that a tunneling event in the left-handed array simultaneously induces a tunneling event in the left-handed array when a small driving voltage is applied to the system.

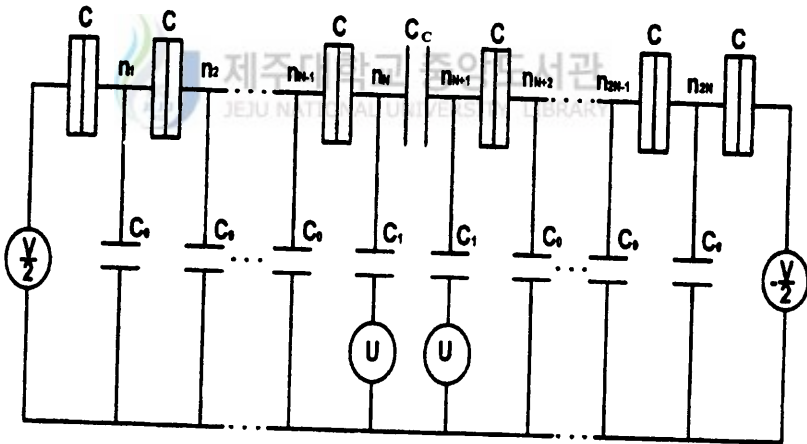
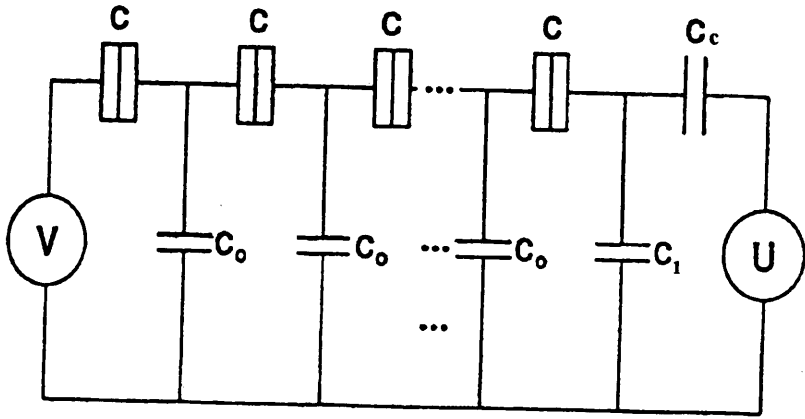


FIG. 24. (a) Single electron trap with N small junctions, with equal junction capacitances C , equal stray capacitances C_0 , input gate capacitances C_1 , and well capacitance C_c . The bias voltages of the two edges are, respectively, V and U . (b) Single electron dual-junction trap with $2N$ small junctions, with equal junction capacitances C , equal stray capacitances C_0 , equal input gate capacitances C_1 , and coupling capacitance C_c . The bias voltages of the two edges are, respectively, $V/2$ and $-V/2$, while the voltages in the middle are U .

If the coupling capacitance decreases the lifetime becomes shorter. This is due to the decrease in the binding energy of the “exciton” and then the two arrays become virtually independent. Thus, this system can be also used as a memory cell by holding an electron-hole pair (“exciton”) on the traps, i.e., “0” state for no extra electron-hole pair (“exciton”) on the traps and “1” state for an electron-hole pair (“exciton”) on the traps. In a sense, it could be considered as a single “exciton” trap [60]. The remarkable thing here is that their study is restricted to the case where the coupling capacitance is smaller than the junction capacitance and the role of the stray capacitance, which is known to be important in determining the soliton width in a one-dimensional (1D) array, has been neglected.

The purpose of this study is to present an exact analytical solution to the electrostatic problem of the biased single electron dual-junction-array trap consisting of equal stray capacitances C_0 , equal junction capacitances C , equal input gate capacitances C_1 , and coupling capacitance C_C , to derive analytical expressions for the total free energy and the threshold voltages for various charge transfer processes (a single electron, a single exciton, and a combined soliton), and to study the effects of the stray capacitances, the input gate capacitances, the coupling capacitance, the number of junction, and the cotunneling process on the threshold voltages of various charge solitons.

The starting point in studying the electrostatics of the single electron dual-junction-array trap is to identify the potential profiles for a given set up of the system. For a single electron dual-junction-array trap with $2N$ junctions, one needs to solve a set of $2N$ linear equations for the corresponding voltages (or equivalently, the charges) on the $2N$ junctions. A set of $2N$ linear equations for the voltages $\{V_i\}$ across each of the $2N$ junctions are developed into a matrix form, and solved

numerically without any presumptions. The key to our approach is to rewrite electrostatic equations as matrix equations for the island potentials $\{\Phi_i\}$; this enables us to derive the electrostatic equations in a tridiagonal matrix form and obtain an exact analytic result for the single electron dual-junction-array trap.

Although the bias voltage controls the average value of the current passing through the system, the dynamics of a single charge soliton in the system at $T = 0$ is in principle solely determined by the Gibbs free energy. The transfer of an soliton from one island to another through the tunnel junction between them is favorable if the Gibbs free energy decreases in this process, and vice versa. Thus, the essence of the dynamics is the evaluation of the Gibbs free energy, which consists of a charging energy term and a work done term. The above mentioned exact solutions of the electrostatics for the single electron dual-junction-array trap enable us to perform systematic studies for the Gibbs free energy and derive an exact analytical form for it at arbitrary charge configurations. This allows us to predict many interesting behavior of the system through the threshold voltage and compare them with numerical results reported previously by Amakawa et al. [66].

The rest of the chapter is organized as follows: In Sec. A, we obtain an exact analytic result of the island potentials $\{\Phi_i\}$ for the single electron dual-junction-array trap, based on the study of 1D array in Ref. 6. With the island potentials obtained in Sec. A, an exact analytical form for Gibbs free energy at arbitrary charge configurations will be derived in Sec. B. In Sec. C, we obtain the threshold voltages for various charge solitons including a single electron, a single exciton, and a combined soliton, using the exact analytical form for Gibbs free energy. In Sec. D, we present the numerical results of the threshold voltages for various charge solitons, to investigate the effects of the stray capacitances, the input gate capacitances, the

coupling capacitance, the number of junction, and the cotunneling process on the threshold voltages of various charge solitons. Conclusions will be given in the last section.

A. Potential Profile

We consider a single electron dual-junction-array trap, as illustrated in Fig. 24(b), where the end of two single electron traps is coupled to each other by a coupling capacitor C_C , each single electron trap consists of N small tunnel junctions in series, with equal stray capacitances C_0 and equal junction capacitances C , and the end of which couples to an input gate capacitance C_1 . The bias voltages of the two edges are, respectively, $V/2$ and $-V/2$, while the voltages in the middle are U . Also, the tunneling resistance R_T of each junction is assumed to be the same and $R_T \gg h/e^2$, which ensures that the wave function of an excess electron on an island is localized there. We denote the potential on each of the individual $2N$ islands between the junctions in the array by the column vector $\bar{\Phi} = \{\Phi_1, \Phi_2, \dots, \Phi_{2N}\}^T$, and the number of excess electrons on each of the individual $2N$ islands is denoted by the column vector $\bar{n} = \{n_1, n_2, \dots, n_{2N}\}^T$. The electrostatic equations for the island potentials $\{\Phi_i\}$ and the number of the excess island electrons $\{n_i\}$ are derived from the charge conservation and Kirchhoff's law, and they obey a set of $2N$ linear equations. These equations can be conveniently expressed in terms of a simple form as

$$\bar{S} \bar{\Phi} = \frac{e}{C} \bar{n}', \quad (7.1)$$

where \bar{n}' means that the first, the N -th, the $(N + 1)$ -th, and the last elements of \bar{n}' are replaced with $n_1 - CV/2e$, $n_N - C_1U/e$, $n_{N+1} - C_1U/e$, and $n_{2N} + CV/2e$,

respectively, to accommodate the effects of the bias voltages and $\bar{\bar{S}}$ is a $2N$ by $2N$ symmetric matrix given by

$$\bar{\bar{S}} = \begin{pmatrix} \bar{\bar{T}}_1 & \alpha \bar{\bar{I}} \\ \alpha \bar{\bar{I}}^T & \bar{\bar{T}}_2 \end{pmatrix} \quad (7.2)$$

with

$$\bar{\bar{T}}_1 = \begin{pmatrix} \bar{\bar{M}} & \bar{\bar{I}} \\ \bar{\bar{I}}^T & D' \end{pmatrix}, \bar{\bar{T}}_2 = \begin{pmatrix} D' & \bar{\bar{I}}'^T \\ \bar{\bar{I}}' & \bar{\bar{M}} \end{pmatrix}, \quad (7.3)$$

$$\bar{\bar{I}} = \begin{pmatrix} \bar{\bar{0}} & \bar{\bar{0}} \\ 1 & \bar{\bar{0}}^T \end{pmatrix}, \bar{\bar{I}}^T = \begin{pmatrix} \bar{\bar{0}} & 1 \\ \bar{\bar{0}} & \bar{\bar{0}} \end{pmatrix}. \quad (7.4)$$

Here, $\alpha = C_C/C$ is coupling constant, $D' = -1 - (C_1 + C_C)/C$, $\bar{\bar{M}}$ is a $(N-1)$ by $(N-1)$ symmetric tridiagonal matrix, having the same diagonal elements $D \equiv -(2 + C_0/C)$ and the same off-diagonal elements 1, and $\bar{\bar{0}}$ denotes a $(N-1)$ by $(N-1)$ null matrix. In Eqs. (7.3) and (7.4), the column vectors $\bar{\bar{I}} = (0, 0, \dots, 1)^T$, $\bar{\bar{I}}' = (1, 0, \dots, 0)^T$, and $\bar{\bar{0}} = (0, 0, \dots, 0)^T$ have $N-1$ elements, respectively.

Then, by taking the inverse matrix of $\bar{\bar{S}}$, i.e., $\bar{\bar{H}}$, we obtain the analytical expression of potential profiles in Eq. (7.1) as

$$\bar{\bar{\Phi}} = \frac{e}{C} \bar{\bar{H}} \bar{\bar{n}}' = \frac{e}{C} \begin{pmatrix} \bar{\bar{P}}_1 & \bar{\bar{Q}}_1 \\ \bar{\bar{Q}}_2 & \bar{\bar{P}}_2 \end{pmatrix} \bar{\bar{n}}', \quad (7.5)$$

where the elements of the $2N$ by $2N$ matrix $\bar{\bar{H}}$ have the following property: $H_{ij} = H_{ji} = H_{2N+1-j, 2N+1-i}$ and $\bar{\bar{P}}_1, \bar{\bar{P}}_2, \bar{\bar{Q}}_1$, and $\bar{\bar{Q}}_2$ are N by N symmetric sub-matrices to the matrix $\bar{\bar{H}}$. The symmetric matrix $\bar{\bar{P}}_1$ in Eq. (7.5) can be expressed by

$$\bar{\bar{P}}_1 = \begin{pmatrix} \bar{\bar{B}} & \frac{1}{D' + R_{N-1} - \alpha^2 / (D' + R_{N-1})} \bar{\bar{R}} \\ \frac{1}{D' + R_{N-1} - \alpha^2 / (D' + R_{N-1})} \bar{\bar{R}}^T & \frac{1}{D' + R_{N-1} - \alpha^2 / (D' + R_{N-1})} \end{pmatrix}, \quad (7.6)$$

where the elements of the $N - 1$ by $N - 1$ symmetric sub-matrix $\overline{\overline{B}}$ and the column vector $\overline{\overline{R}}$ are, respectively, given by

$$\left(\overline{\overline{B}}\right)_{ij} \equiv R'_{ij} = (-1)^{i+j+1} M'_{N-1-j} M_{N-1} / M'_{N-1} \quad \text{for } i \leq j \text{ and } i, j \leq N - 1, \quad (7.7)$$

$$R_i = \frac{\sinh \lambda}{\sinh N\lambda} \equiv R_{iN-1}. \quad (7.8)$$

Here, $M'_{j+1} = GM_j - M_{j-1}$ with $M_j = (-1)^j \sinh(j+1)\lambda / \sinh \lambda$ and $G = D - 1/(D' - \alpha^2/(D' + R_{N-1}))$, λ is determined by $-2 \cosh \lambda = D \equiv -(2 + C_0/C)$, and $R_{i,j}$ is the elements of the inverse matrix of a $N - 1$ by $N - 1$ symmetric matrix $\overline{\overline{M}}$ in Eq. (7.3), which is given by

$$R_{ij} = -\frac{\cosh(N + |j - i|)\lambda - \cosh(N - j - i)\lambda}{2 \sinh \lambda \sinh N\lambda}, \quad i, j = 1, 2, \dots, N - 1. \quad (7.9)$$

In addition, the elements of the N by N symmetric sub-matrices, $\overline{\overline{P}}_2$, $\overline{\overline{Q}}_1$, and $\overline{\overline{Q}}_2$ in Eq. (7.5) are, respectively, given by

$$\left(\overline{\overline{P}}_2\right)_{ij} \equiv R'_{N+1-jN+1-i} = R'_{N+1-iN+1-j}, \quad (7.10)$$

$$\left(\overline{\overline{Q}}_1\right)_{ij} = -\alpha R'_{N+1-jN} R_{iN}, \quad (7.11)$$

$$\left(\overline{\overline{Q}}_2\right)_{ij} = -\alpha R_{NN+1-i} R'_{jN}. \quad (7.12)$$

It is to be noted that Eq. (7.5), supplemented by Eqs. (7.6) and (7.10)–(7.12), is a general expression for the potential profile of the single electron dual-junction-array trap with $2N$ tunneling junctions with equal stray capacitances. If the value of α is taken as 0, Eq. (7.6) becomes the identical expression of symmetric matrix appearing in the potential profile for normal trap obtained by Hu et al. [6]. Moreover, Eq. (7.5)

reduces to the Hu et al.'s result [6] of the potential profile for one-dimensional array with $2N + 1$ tunneling junctions with equal stray capacitances if the value of α is taken as 1. Equation (7.5), together with Eqs. (7.6) and (7.10)–(7.12), is a basic result of this paper. Once a charge profile $\{n_i\}$ is known, we can use Eq. (7.5) to determine the potential profile $\{\Phi_i\}$ for the single electron dual-junction-array trap.

B. Free Energy and Charging Energy

In this section, we want to evaluate the Gibbs free energy of the single electron dual-junction-array trap, by using the exact solution $\bar{\Phi}$ of Eq. (7.5). Since the free energy is a crucial quantity in determining the rate of tunneling in small junctions, one needs to define it in a precise way. Basically, the free energy contains two terms, the electrostatic energy and the work done by moving the charged soliton through the system.

For a biased single electron dual-junction-array trap as illustrated by Fig. 24(b), the Gibbs free energy can be written as

$$F = E_s + W, \quad (7.13)$$

where the electrostatic energy is defined as

$$E_s = E_c - e \sum_{i=0}^{2N+1} n_i \Phi_i \quad (7.14)$$

with the charging energy

$$\begin{aligned} E_c = & \frac{C}{2} \sum_{i=1}^{N-1} (\Phi_{i+1} - \Phi_i)^2 + \frac{C}{2} \sum_{i=N+1}^{2N-1} (\Phi_{i+1} - \Phi_i)^2 + \frac{C}{2} \left(\Phi_1 - \frac{V}{2} \right)^2 \\ & + \frac{C}{2} \left(\Phi_{2N} + \frac{V}{2} \right)^2 + \frac{C_C}{2} (\Phi_{N+1} - \Phi_N)^2 + \frac{C_0}{2} \sum_{i=1}^{N-1} \Phi_i^2 + \frac{C_0}{2} \sum_{i=N+2}^{2N} \Phi_i^2 \\ & + \frac{C_1}{2} (U - \Phi_N)^2 + \frac{C_1}{2} (U - \Phi_{N+1})^2. \end{aligned} \quad (7.15)$$

In addition, in Eq. (7.13), the work due to the charge redistribution associated with the change of the charge profile $\{\bar{n}\}$ is given by

$$\begin{aligned}
W = & -C \sum_{i=1}^{N-1} (\Phi_{i+1} - \Phi_i)^2 - C \sum_{i=N+1}^{2N-1} (\Phi_{i+1} - \Phi_i)^2 - C_C (\Phi_{N+1} - \Phi_N)^2 \\
& -C \left(\Phi_1 - \frac{V}{2} \right)^2 - C \left(\Phi_{2N} + \frac{V}{2} \right)^2 - C_0 \sum_{i=1}^{N-1} \Phi_i^2 - C_0 \sum_{i=N+2}^{2N} \Phi_i^2 \\
& -C_1 (U - \Phi_N)^2 - C_1 (U - \Phi_{N+1})^2.
\end{aligned} \tag{7.16}$$

In order to study the change of the Gibbs free energy in the event of a charge soliton transfer, it is desirable to rewrite it as a function of the charge profile $\{n_i\}$. For this purpose, after some algebra with Eqs. (7.5) and (7.13)–(7.16), we can obtain the Gibbs free energy as

$$F = E_{ch} - \frac{e^2}{2C} \sum_{i=1}^{2N} \sum_{j=1}^{2N} n_i H_{ij} n_j - \frac{1}{2} V (Q_0 - Q_{2N+1}) = U (Q_N^g + Q_{N+1}^g), \tag{7.17}$$

where

$$E_{ch} = \frac{1}{4} C V^2 (1 + H_{11} - H_{12N}) + C_1 U^2 \left(1 + \frac{C_1}{C} H_{NN} + \frac{C_1}{C} H_{NN+1} \right), \tag{7.18}$$

$$Q_N^g = C_1 (U - \Phi_N), \quad Q_{N+1}^g = C_1 (U - \Phi_{N+1}), \tag{7.19}$$

$$Q_0 = n_0 e + C \left(\frac{V}{2} - \Phi_1 \right), \quad Q_{2N+1} = n_{2N+1} e + C \left(-\frac{V}{2} - \Phi_{2N} \right). \tag{7.20}$$

Equation (7.17) is a general expression for the Gibbs free energy of a single-electron dual-junction-array trap with bias voltage $\{V, U\}$, charge profile $\{n_i e\}$, and potential profile $\{\Phi_i\}$ on the islands. Based on the Gibbs free energy (7.17), one can directly study the dynamics of the single electron tunneling by calculating the change of the Gibbs free energy ΔF due to some charge transfer event. To be definite, here we discuss the case where the charge transfer happened between two islands k and k' ,

while the charges on the other islands are unchanged. We assume, however, that the tunneling between two islands N and $N + 1$ is negligible, so that we have two circuits that are independent galvanically but are coupled electrostatically [60]. We denote the charges on these islands before and after the charge transfer as $\{n_k, n_{k'}\}$ and $\{n'_k, n'_{k'}\}$, respectively, and the net transferred charges as Q , where Q can be a single electron, a single exciton, or a combined soliton, which will be discussed in the next section. Thus, we obtain, from Eq. (7.17), the change of the Gibbs free energy $\Delta F^Q(k, k')$ due to the charge transfer $\{n_k, n_{k'}\}$ to $\{n'_k, n'_{k'}\}$

$$\Delta F^Q(k, k') \equiv F(\{n'_k, n'_{k'}\}) - F(\{n_k, n_{k'}\}) = \Delta E^Q(k, k') + W^Q(k, k'), \quad (7.21)$$

where the detailed form of the change of the charging energy $\Delta E^Q(k, k')$ and the work done $W^Q(k, k')$ in Eq. (7.21) can directly be worked out from Eq. (7.17).

C. Threshold Voltage

Now, let us calculate the change of the Gibbs free energy $\Delta F^Q(k, k')$ due to some charge transfer by means of Eq. (7.21). Here we consider three cases of particular interest: (i) the *single charge soliton* (e) case, where an electron is transferred from the k th island to the k' th island in the left-hand side array, i.e., $n'_k - n_k = -1$, $n'_{k'} - n_{k'} = 1$, $n'_{2N-k+1} - n_{2N-k+1} = 0$, $n'_{2N-k'+1} - n_{2N-k'+1} = 0$; (ii) the *exciton soliton* (*electron-hole pair*, ex) case, where an electron in the left-hand side array is transferred from the k th island to the k' th island and an electron in the right-hand side array is simultaneously transferred from the $(2N - k' + 1)$ th island to the $(2N - k + 1)$ th island, i.e., $n'_k - n_k = -1$, $n'_{k'} - n_{k'} = 1$, $n'_{2N-k+1} - n_{2N-k+1} = 1$, $n'_{2N-k'+1} - n_{2N-k'+1} = -1$; (iii) the *combined soliton* (*exciton-single electron*, $ex-e$) case, where in addition to the exciton case, an electron in the left-hand side

array is transferred from the k' th island to the k'' th island, i.e., $n'_k - n_k = -1$, $n'_{k'} - n_{k'} = 0$, $n'_{k''} - n_{k''} = 1$, $n'_{2N-k+1} - n_{2N-k+1} = 1$, $n'_{2N-k'+1} - n_{2N-k'+1} = -1$. Under the above conditions, the change of the Gibbs free energy for each *charge soliton transfer* can be derived from Eq. (7.17) as

$$\begin{aligned} \Delta F^e(k, k') &= F^e(k') - F^e(k) = -\frac{e^2}{2C} (H_{k'k'} - H_{kk}) \\ &\quad - \frac{1}{2} eV (\delta_{0,k'} - \delta_{0,k} - \delta_{2N+1,k'} + \delta_{2N+1,k} - H_{1k'} + H_{2Nk'} + H_{1k} - H_{2Nk}), \end{aligned} \quad (7.22)$$

$$\begin{aligned} \Delta F^{ex}(k, k') &= F^{ex}(k') - F^{ex}(k) = -\frac{e^2}{C} (H_{k'k'} - H_{k'2N-k'+1} - H_{kk} + H_{k2N-k+1}) \\ &\quad - \frac{1}{2} eV (\delta_{0,k'} + \delta_{2N+1,2N-k'+1} - \delta_{0,k} - \delta_{2N+1,2N-k+1}) \\ &\quad + eV (H_{1k'} - H_{12N-k'+1} - H_{1k} + H_{12N-k+1}), \end{aligned} \quad (7.23)$$

$$\begin{aligned} \Delta F^{ex-e}(k, k'; k'') &= F^{ex-e}(k', k'') - F^{ex-e}(k) \\ &= -\frac{e^2}{2C} (H_{k''k''} + H_{k'k'} - 2H_{k''2N-k'+1} - H_{kk} + H_{k2N-k+1}) \\ &\quad - \frac{1}{2} eV (\delta_{0,k''} + \delta_{2N+1,2N-k'+1} - \delta_{0,k} - \delta_{2N+1,2N-k+1}) \\ &\quad + \frac{1}{2} eV (H_{1k''} - H_{12N-k'+1} - H_{12N-k''+1} + H_{1k'} - 2H_{1k} + 2H_{12N-k+1}), \end{aligned} \quad (7.24)$$

where the bias voltage U was taken as 0 for convenience.

The tunneling of a charge soliton from the k th island to the k' th island in the single electron dual-junction-array trap is energy favorable when the free energy $\Delta F^Q(k, k')$ is less than zero, and vice versa. Thus, the threshold energy V_t for the transfer of a charge soliton from the k th island onto the k' th island, can be obtained by equating $\Delta F^Q(k, k') = 0$. Applying this principle to Eqs. (7.22)–(7.24), we can obtain the threshold voltages for various *charge soliton transfer* cases as

$$V_t^e(k, k') = \frac{e}{C} \frac{(H_{k'k'} - H_{kk})}{\delta_{0,k'} - \delta_{0,k} - \delta_{2N+1,k'} + \delta_{2N+1,k} - H_{1k'} + H_{2Nk'} + H_{1k} - H_{2Nk}}, \quad (7.25)$$

$$\begin{aligned} V_t^{ex}(k, k') &= \frac{2e}{C} (H_{k'k'} - H_{k'2N-k'+1} - H_{kk} + H_{k2N-k+1}) \\ &\quad / [(\delta_{0,k} + \delta_{2N+1,2N-k+1} - \delta_{0,k'} - \delta_{2N+1,2N-k'+1}) \\ &\quad + 2(H_{1k'} - H_{12N-k'+1} - H_{1k} + H_{12N-k+1})], \end{aligned} \quad (7.26)$$

$$\begin{aligned} V_t^{ex-e}(k; k', k'') &= \frac{2e}{C} (H_{k'k'} - H_{k'2N-k'+1} - H_{kk} + H_{k2N-k+1}) \\ &\quad / [(-\delta_{0,k'} - \delta_{2N+1,2N-k'+1} + \delta_{0,k} + \delta_{2N+1,2N-k+1}) \\ &\quad + 2(H_{12N-k'+1} - H_{1k'} - H_{12N-k+1} + H_{1k})]. \end{aligned} \quad (7.27)$$

Equations (7.25)–(7.27) are key results of the threshold voltages for various *charge soliton transfer* cases, which enable us to analyze the charge transport in the single electron dual-junction-array trap. It is clearly seen from Eqs. (7.25)–(7.27) that the threshold voltages are very sensitive to the cotunneling process, the number of junction N , the coupling capacitance C_C , the stray capacitance C_0 , and the junction capacitance C , as well as the input gate capacitance C_1 through the elements of the $2N$ by $2N$ symmetric matrix \overline{H} .

D. Numerical Results

In this section, we present the numerical results of the threshold voltages obtained for various charge soliton transfer processes (a single electron, an exciton, a combined soliton). First, we study the C_0 , C_1 , C_C , and C dependence of threshold voltages for various charge soliton transfer processes in the case where one-junction tunneling, i.e., $m(\equiv k' - k) = 1$ for $k = 0$ in Eqs. (7.25)–(7.27), is allowed in the single electron

dual-junction-array trap having only three tunnel junctions ($N = 3$) on each array side, and then perform an analysis of the N and cotunneling dependences of the threshold voltages at a fixed value of C_1 , C_C , and C for various stray capacitances, as an example.

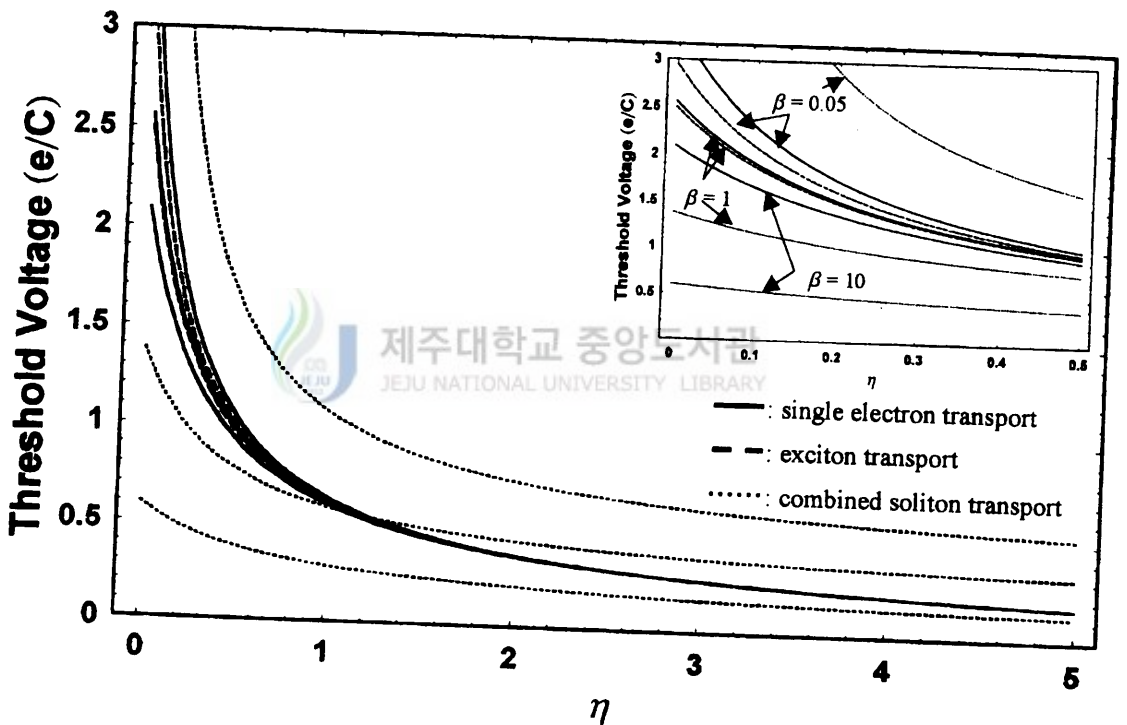


FIG. 25. Threshold voltages (in units of e/C) for injecting a charge soliton into the first island of single electron dual-junction-array trap with three junctions ($N = 3$) on each side as a function of $\eta = C_0/C$ at $\beta = C_1/C = 0.05, 1, 10$ and $\alpha = C_C/C = 0.5$. Shown in the inset is an enlarged part of the figure in the small α region. Also, C_C , C_1 , C , and C_0 are the coupling capacitance, input gate capacitance, junction capacitance, and stray capacitance, respectively.

The stray capacitance dependence of the threshold voltages (in units of e/C) for various charge solitons is illustrated by Fig. 25, where we plot the threshold voltages in Eqs. (7.25)–(7.27) as a function of the ratio of stray capacitance to the junction capacitance, i.e., $\eta = C_0/C$ at $\beta = C_1/C = 0.05, 1, 10$ and $\alpha = C_C/C = 0.5$. It is clearly seen from the figure that the threshold voltages of all charge solitons decrease with the increase of the value of η . For $\eta \rightarrow 0$ and small $\beta (< 1)$, the exciton has the lowest threshold voltage than any other solitons. This means that the exciton transport is dominant in the system, as reported by Amakawa et al. [66]. However, as can be seen from the inset which is enlarged part of the figure in the small η region, for large $\beta (\geq 1)$ the combined soliton has the lowest threshold voltage and the combined one is expected to be dominant. Thus, for no stray capacitance, the solitons which are dominant in the system can be a single exciton or a combined soliton depending on the input gate capacitance. The small change of η in the small $\eta (< 1)$ region leads to a lot of change of threshold voltage, but the threshold voltages are almost constant in the large $\eta (> 1)$ region. The interesting thing is the $\beta = 1$ case. For small $\eta (\leq 1)$, the combined soliton has the lowest threshold voltage, while for large $\eta (> 1)$ single electron or exciton has the lowest threshold voltage. Thus, the dominant soliton transport varies with the stray capacitance. Moreover, the threshold voltage of exciton merges into that of single electron for small η and large β or large η and small β . In that case, single electron and exciton transport coexist and will be dominant. For large β and η , however, the combined soliton transport is expected to be dominant.

Figure 26 shows the dependence of the threshold voltage (in units of e/C) on the input gate capacitance for various charge solitons, where we plot the threshold voltages in Eqs. (7.25)–(7.27) as a function of the ratio of input gate capacitance to

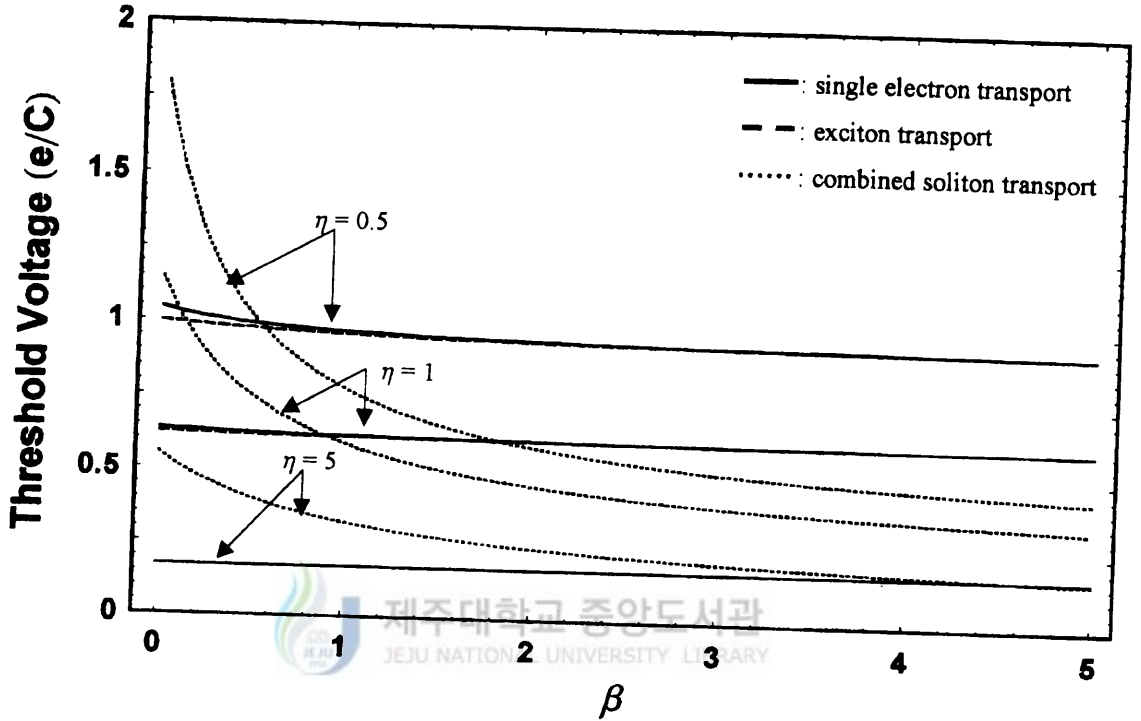


FIG. 26. Threshold voltages (in units of e/C) for injecting a charge soliton into the first island of single electron dual-junction-array trap with three junctions ($N = 3$) on each side as a function of $\beta = C_1/C$ at $\alpha = C_C/C = 0.5$ and $\eta = C_0/C = 0.5, 1, 5$, where C_C , C_1 , C , and C_0 are the coupling capacitance, input gate capacitance, junction capacitance, and stray capacitance, respectively.

the junction capacitance, i.e., $\beta = C_1/C$ at $\alpha = 0.5$ for various stray capacitances of $\eta = 0.5, 1, 5$. As can be seen from the figure, if the value of β increases for a specific value of η , the threshold voltages of single electron and exciton remain constant, whereas those of the combined soliton decrease. Moreover, the threshold voltage of exciton merges into that of single electron for small η and large β or large η and small β . In that case, single electron and exciton transport coexist and will be

dominant. For large β and η , however, the combined soliton transport is expected to be dominant.

Figure 26 shows the dependence of the threshold voltage (in units of e/C) on the input gate capacitance for various charge solitons, where we plot the threshold voltages in Eqs. (7.25)–(7.27) as a function of the ratio of input gate capacitance to the junction capacitance, i.e., $\beta = C_1/C$ at $\alpha = 0.5$ for various stray capacitances of $\eta = 0.5, 1, 5$. As can be seen from the figure, if the value of β increases for a specific value of η , the threshold voltages of single electron and exciton remain constant, whereas those of the combined soliton decrease. As a result, the change of soliton transports is expected from the increase of β . For small η , exciton transport dominates in the small β region, but if the value of β increases, the combined soliton becomes dominant. Furthermore, if the value of β and η increases, the slight difference of the threshold voltages between exciton and single electron disappears. Then, both soliton transport will be dominant for large η and small β . Thus, the charge soliton transport is sensitive to the values of the stray capacitance C_0 , the junction capacitance C , and the input gate capacitance C_1 . The results shown in Figs. 25 and 26 are restricted to the specific value of $\alpha = 0.5$. The threshold voltages (in units of e/C) for various charge solitons is shown in Fig. 27, as a function of the ratio of coupling capacitance to the junction capacitance, i.e., $\alpha = C_C/C$ at $\eta = 0.05$ for various input gate capacitances of $\beta = 0.5, 1, 5$. This figure shows that the threshold voltages of all charge solitons remain constant, except for small α and β . If the coupling capacitance approaches to zero, or the value of β increases, the threshold voltage of exciton merges into that of single electron. However, their threshold voltage have larger values than the combined soliton. As shown in the figure, for given parameters β and η the combined soliton has the lowest threshold voltages than

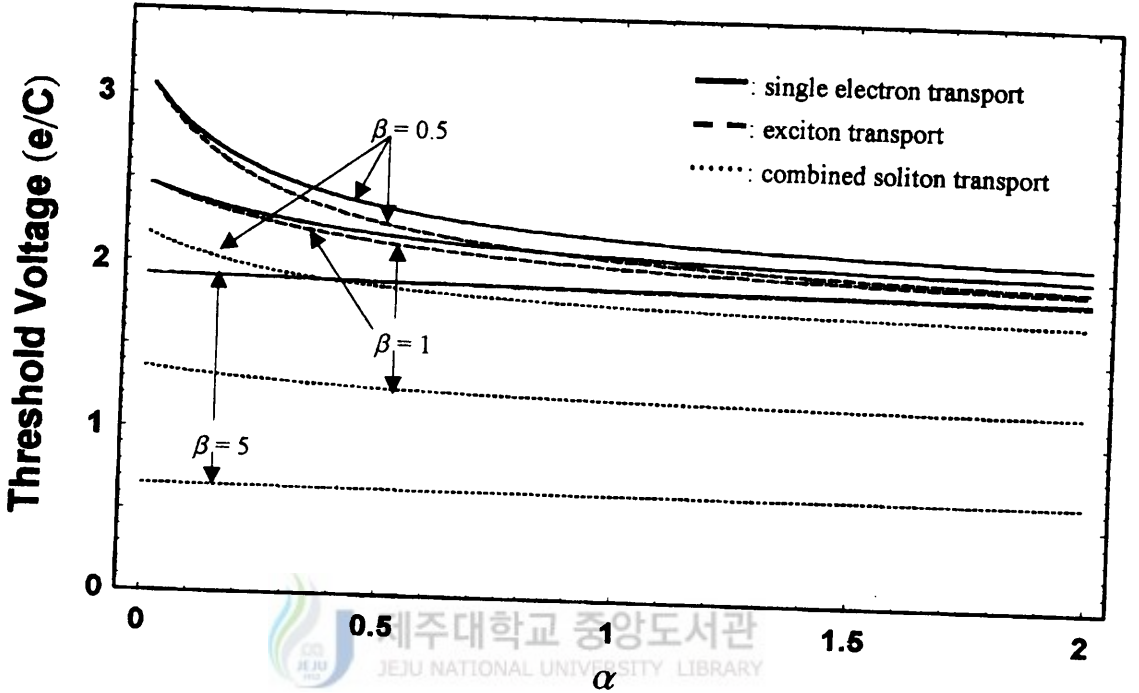


FIG. 27. Threshold voltages (in units of e/C) for injecting a charge soliton into the first island of single electron dual-junction-array trap with three junctions ($N = 3$) on each side as a function of $\alpha = C_C/C$ at $\eta = C_0/C = 0.05$ and $\beta = C_1/C = 0.5, 1, 5$, where C_C , C_1 , C , and C_0 are the coupling capacitance, input gate capacitance, junction capacitance, and stray capacitance, respectively.

any other solitons and hence the combined soliton transport is expected to be dominant for all given α . It should be noted that the results given in Figs. 24, 25, and 26 are valid for $N = 3$ and one-junction tunneling. As discussed before, the threshold voltages of charge solitons are influenced by the parameters characterizing the system, such as the coupling capacitance C_C , the stray capacitance C_0 , and the junction capacitance C , as well as the input gate capacitance C_1 . In addition, the cotunneling effect and the number of junction N also affect the threshold voltages of

charge solitons. Figure 28 shows the dependence of the threshold voltages for various charge solitons on the number of junction N at a fixed value of $\alpha = \beta = 0.5$ for various stray capacitances $\eta = 0.05, 1, 5$.

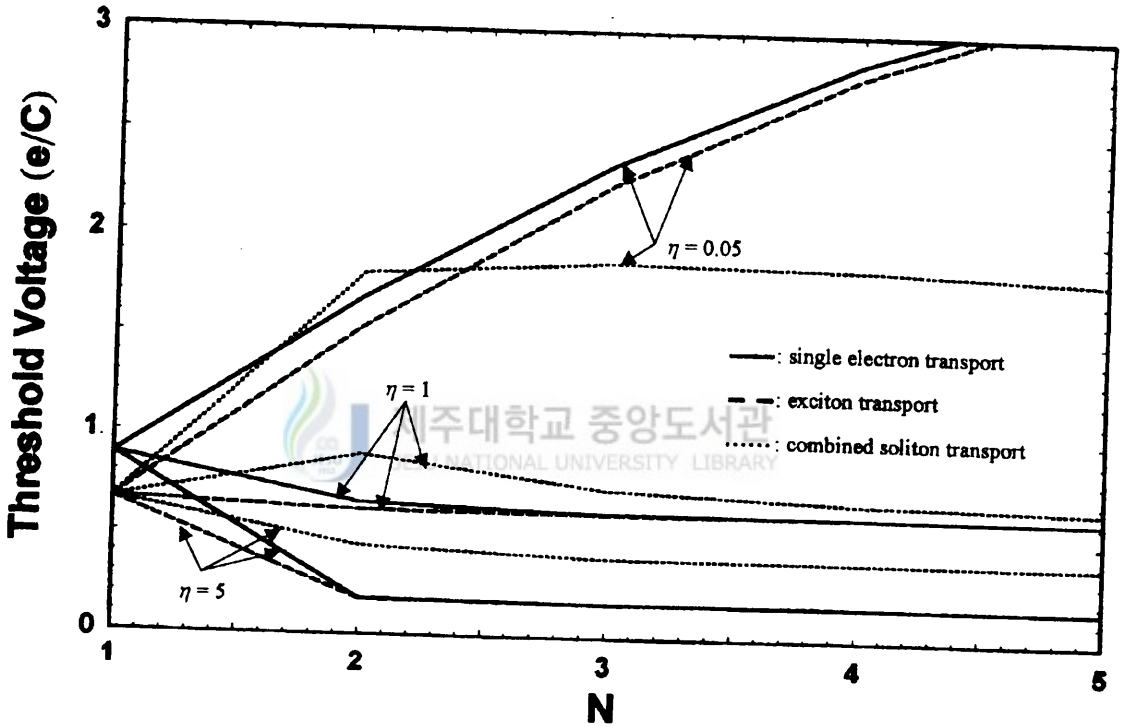


FIG. 28. Threshold voltages for injecting a charge soliton into the first island of single electron dual-junction-array trap as a function of the number of junction N at a fixed value of $\alpha = C_C/C = \beta = C_1/C = 0.5$ and $\eta = C_0/C = 0.05, 1, 5$, where C_C , C_1 , C , and C_0 are the coupling capacitance, input gate capacitance, junction capacitance, and stray capacitance, respectively.

It is clearly seen from the figure that, as mentioned in Fig. 25, the threshold voltages decreases with the increase of the stray capacitance and the changes of the dominant soliton in the transport is expected for $N \leq 3$, rather than $N > 3$. Comparing the

threshold voltages of charge solitons for $N = 2$ and that of charge solitons for $N = 3$ in the case of small η , we can see that the exciton transport is expected to be dominant for $N = 2$, whereas the combined soliton transport is dominant for $N = 3$. Thus, the change of the number of junction leads to any change of charge soliton transport. This is valid for $\alpha = \beta = 0.5$. Note that the N dependence of the threshold voltages for various charge solitons varies with the values of α and β , as is expected from Figs. 25, 26, and 27.

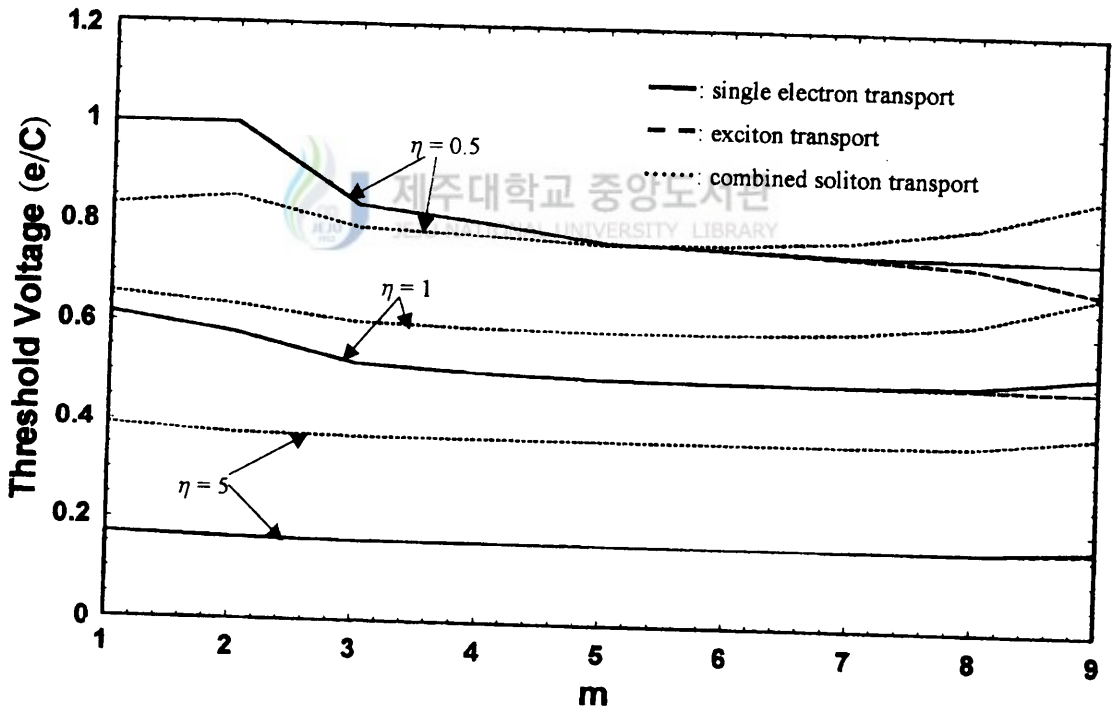


FIG. 29. Threshold voltages of single electron dual-junction-array trap with ten junctions ($N = 10$) on each side as a function of cotunneling (m) at $\alpha = C_C/C = \beta = C_1/C = 0.5$, and $\eta = C_0/C = 0.5, 1, 5$, where C_C , C_1 , C , and C_0 are the coupling capacitance, input gate capacitance, junction capacitance, and stray capacitance, respectively.

The cotunneling (m) dependence of the threshold voltages for various charge solitons is shown in Fig. 29, where the circuit parameters were taken as $N = 10$, $\alpha = \beta = 0.5$, and $\eta = 0.5, 1, 5$ as an example. As shown in the figure, the threshold voltages have various dependence on the cotunneling according to the stray capacitance. For small $\eta (\leq 1)$, the change of the dominant soliton in the transport from the combined soliton to the exciton is expected as the cotunneling is increased. However, one can see that if the stray capacitance increases, the single electron or exciton transport becomes dominant because the threshold voltages for single electron and exciton are nearly same. Thus, we can see that the threshold voltages of solitons can be influenced by the effect of cotunneling. The results are restricted to the special cases of $N = 10$, $\alpha = \beta = 0.5$, and $\eta = 0.5, 1, 5$. It should be noted that, as can be expected from previous figures, the threshold voltages of charge solitons can show different cotunneling dependence, according to the values of N , α , β , and η .

E. Conclusions

So far, we have presented an exact solution for the potential profiles of the biased single electron dual-junction-array trap with equal stray capacitances. Based on Eq. (7.5), we have obtained an analytical Gibbs free energy, as well as the threshold voltages of Eqs. (7.25)–(7.27) for various charge solitons including a single electron, an exciton, and a combined soliton. With the obtained threshold voltage, we have performed the numerical analysis, in order to understand the dependence of threshold voltages on the stray capacitance, the coupling capacitance, the input gate capacitance, and the number of junction, as well as the cotunneling.

Our results for the case where one-junction tunneling is allowed in the single

electron dual-junction-array trap having only three tunnel junctions ($N = 3$) on each array side show that the threshold voltages of all charge solitons decrease with the increase of the stray capacitance. For no stray capacitance and weak coupling and input gate capacitances, the exciton transport becomes dominant in the system, as reported by Amakawa et al. [66]. However, if the input gate capacitance is increased, the combined charge soliton has lowest threshold voltage than any other charge solitons and it becomes dominant in transport. Thus, for no stray capacitance, the solitons which are dominant in the system can be a single exciton or a combined soliton according to the input gate capacitance. A lot of change of threshold voltage in the small stray capacitance region is expected, but the threshold voltages are almost constant in the large stray capacitance region. In consequence, for the case where the input gate capacitance is same as the junction capacitance, the dominant soliton in transport can be a combined soliton, a single electron, or an exciton, depending on the stray capacitance. Thus, for a specific coupling capacitance, the dominant soliton in transport can be a combined soliton, a single electron, or an exciton, according to the stray capacitance and the input gate capacitance..

Various charge solitons having the lowest threshold voltage are also expected for specific values of the coupling capacitance, the input gate capacitance, and the stray capacitance as the number of junction changes. In particular, the changes of the dominant soliton in the transport is expected for $N \leq 3$, rather than $N > 3$, in the case of a given value of $\alpha = \beta = 0.5$. Comparing the threshold voltages of charge solitons for $N = 2$ and that of charge solitons for $N = 3$ in the case of small η , we can see that the exciton transport is expected to be dominant for $N = 2$, whereas the combined soliton transport is dominant for $N = 3$. Thus, the change of the number of junction leads to any change of charge soliton transport. In addition, the

effect of cotunneling, which is sensitive to the stray capacitance, plays an important role in determining solitons which are dominant in the system. For small stray capacitance, the change of the dominant soliton in the transport from the combined soliton to the exciton is expected as the cotunneling is increased. However, one can see that if the stray capacitance increases, the single electron or exciton transport becomes dominant because the threshold voltages for single electron and exciton are nearly same. Thus, various charge soliton transports are expected, depending on the parameters characterizing the system, such as the coupling capacitance C_C , the stray capacitance C_0 , and the junction capacitance C , the input gate capacitance C_1 , and the number of junction, as well as the cotunneling.

We conclude that, in studying charge transport of the biased single electron dual-junction-array trap with equal stray capacitances, it is necessary to treat the electrostatic problem exactly. The quantitative behavior identified in this paper should provide useful information pertaining to future experiments.

VIII. HYSTERETIC VOLTAGE GAP FOR A SINGLE ELECTRON DUAL-JUNCTION-ARRAY TRAP WITH STRAY CAPACITANCES

Correlated single-electron tunneling phenomena based on the Coulomb blockade effect in nanostructures have been attracting wide attention. A lot of work have been made [5,60,66,69,70] on the physics of SET phenomena and on the wide variety of SET device applications. One system of our interest is the single electron dual-junction-array trap, which is composed of two capacitively-coupled normal traps as shown in Fig. 24(b). In this system the currents in the left and right arrays flow in a highly correlated manner because charge transport in the system is strongly affected by electrostatic coupling. Recently, Amakawa, Fujishima, and Hoh [66] studied the charge transport in such a system by using computer simulation taking into account cotunneling, based on the tunneling rate obtained from the approximation proposed by Fonseca et al. [65]. However, their study is restricted to the case of small coupling capacitance region, i.e. $C_C/C < 1$, where C_C and C are the coupling capacitance and the junction capacitance, respectively. Therefore, there are still some important questions which remains unanswered for the large C_C region. In addition, the role of the stray capacitance, which is known to be important in determining the soliton width in a one-dimensional (1D) array, has not been fully explored. The purpose of this study is to present the hysteretic voltage gaps of the single electron dual-junction-array trap consisting of equal stray capacitances C_0 , equal junction capacitances C , equal input gate capacitances C_1 , and coupling capacitance C_C for various charge transfer processes (a single electron, an single exciton, and a combined soliton), on the basis of the exact analytical solution to the electrostatic problem of the single electron dual-junction-array trap presented in

the previous work [71], and to analyze them according to the parameters contained in the system. In particular, we are interested in the effect of the stray capacitance of the hysteretic voltage gap.

The starting point here is the Gibbs free energy, which can be written as [71]

$$F = E_{ch} - \frac{e^2}{2C} \sum_{i,j=1}^{2N} n_i H_{ij} n_j - \frac{1}{2} V Q_0 + \frac{1}{2} V Q_{2N+1} - U Q_N^g - U Q_{N+1}^g, \quad (8.1)$$

where V is the bias voltage, U is the gate voltage on the input gate capacitance, n_i is the number of excess electrons on the i th island, and H_{ij} is a matrix element which depends on C_0 , C , C_1 , and C_C . For detailed expressions of E_{ch} , H_{ij} , Q_0 , Q_{2N+1} , Q_N^g , and $U Q_{N+1}^g$, we refer to Eqs. (5)–(12) and (18)–(20) in Ref. 71.

Equation (8.1) is a general expression for the Gibbs free energy of a single-electron dual-junction-array trap with bias voltage $\{V, U\}$, charge profile $\{n_i e\}$ on the islands. Based on the Gibbs free energy (8.1), one can directly study the dynamics of the single electron tunneling by calculating the change of the Gibbs free energy ΔF due to some charge transfer event. To be definite, here we consider the three cases where the charge transfer happened between two islands k and k' , while the charges on the other islands are unchanged: (i) the *single charge soliton* (e) case, where an electron is transferred from the k th island to the k' th island in the left-hand side array (or the right-hand side array); (ii) the *exciton* (*electron-hole pair*, $e-h$) case, where an electron in the left-hand side array is transferred from the k th island to the k' th island and an electron in the right-hand side array is simultaneously transferred from the $(2N - k' + 1)$ th island to the $(2N - k + 1)$ th island; (iii) the *combined soliton* (*exciton-single electron*, $ex-e$) case, where in addition to the exciton case, an electron in the left-hand side array is transferred from the k' th island to the k'' th island. We assume, however, that the tunneling between two islands N and $N + 1$ is negligible, so that we have two circuits that are independent

galvanically but are coupled electrostatically [60]. We denote the charges on these islands before and after the charge transfer as $\{n_k, n_{k'}\}$ and $\{n'_k, n'_{k'}\}$, respectively, and the net transferred charges as Q , where Q can be a single electron, an exciton, or a combined soliton. Under the above conditions, the change of the Gibbs free energy for three cases of *charge soliton transfer* can be derived from Eq. (8.1).

The tunneling of a charge soliton from the k th island to the k' th island in the single electron dual-junction-array trap is energy favorable when the change of free energy $\Delta F^Q(k, k')$ is less than zero, and vice versa. Thus, the threshold energy V_t for the transfer of a charge soliton from the k th island onto the k' th island, can be obtained by equating $\Delta F^Q(k, k') = 0$. From Eqs. (8.1), we obtain (for convenience, we take $U = 0$) for the *single electron transfer* case, the *exciton case*, and the *combined soliton case*, respectively, as

$$V_t^e(k, k') = \frac{e}{C} \frac{(H_{k'k'} - H_{kk})}{\delta_{0,k'} - \delta_{0,k} - \delta_{2N+1,k'} + \delta_{2N+1,k} - H_{1k'} + H_{2Nk'} + H_{1k} - H_{2Nk}}, \quad (8.2)$$

$$\begin{aligned} V_t^{ex}(k, k') &= \frac{2e}{C} (H_{k'k'} - H_{k'2N-k'+1} - H_{kk} + H_{k2N-k+1}) \\ &\quad / [(\delta_{0,k} + \delta_{2N+1,2N-k+1} - \delta_{0,k'} - \delta_{2N+1,2N-k'+1}) \\ &\quad + 2(H_{1k'} - H_{12N-k'+1} - H_{1k} + H_{12N-k+1})], \end{aligned} \quad (8.3)$$

$$\begin{aligned} V_t^{ex-e}(k; k', k'') &= \frac{2e}{C} (H_{k'k'} - H_{k'2N-k'+1} - H_{kk} + H_{k2N-k+1}) \\ &\quad / [(-\delta_{0,k'} - \delta_{2N+1,2N-k'+1} + \delta_{0,k} + \delta_{2N+1,2N-k+1}) \\ &\quad + 2(H_{12N-k'+1} - H_{1k'} - H_{12N-k+1} + H_{1k})]. \end{aligned} \quad (8.4)$$

Equations (8.2)–(8.4) enable us to immediately find the tunneling and escape threshold voltages at $T = 0$ in the m -junction tunneling sequence ($k \longleftrightarrow k + m$) for the

single electron transfer case, the *exciton case*, and the *combined soliton case*, respectively.

For the m -junction tunneling events of the *single electron transfer case*, the tunneling threshold voltage at $T = 0$ is given by $V_t^e(0, m)$ or $V_t^e(2N + 1, 2N + 1 - m)$ because each absolute value is the largest for an electron tunneling into the trap (N th island) of the left-handed array or the trap ($N + 1$ th island) of the right-handed array, whereas the escape threshold voltage is given by $V_t^e(N, N - m)$ or $V_t^e(N + 1, N + 1 + m)$ because each absolute value is the largest for an electron escaping from the trap (N th island) of the left-handed array or the trap ($N + 1$ th island) of the right-handed array. As a matter of fact, $V_t^e(0, m)$ and $V_t^e(2N + 1, 2N + 1 - m)$ for the tunneling threshold voltage have an identical quantity, and $V_t^e(N, N - m)$ and $V_t^e(N + 1, N + 1 + m)$ for the escape threshold voltage are same each other because the circuit is symmetric. As a result, the tunneling and escape threshold voltages are, respectively, given by

$$V_t^e(0, m) = -\frac{e}{C} \frac{H_{mm}}{1 + H_{1m} - H_{2Nm}}, \quad (8.5)$$

$$V_t^e(N, N - m) = \frac{e}{C} \frac{H_{N-mN-m} - H_{NN}}{\delta_{0, N-m} - H_{1N-m} + H_{N-m2N} + H_{1N} - H_{1N+1}} \quad \text{for } 1 \leq m \leq N. \quad (8.6)$$

For the *exciton case*, the tunneling and escape threshold voltages are, respectively, given by $V_t^{ex}(0, m)$ and $V_t^{ex}(N, N - m)$ because their absolute values are, respectively, the largest for an exciton tunneling into the traps (N th and $N + 1$ th island) of both sides and for an exciton escaping from the traps, which are

$$V_t^{ex}(0, m) = \frac{e}{C} \frac{H_{mm} - H_{m2N-m+1}}{1 + H_{1m} - H_{12N-m+1}}, \quad (8.7)$$

$$V_t^{ex}(N, N-m) = \frac{2e}{C} (H_{N-mN-m} - H_{N-mN+1+m} - H_{NN} + H_{NN+1}) \times [-\delta_{0,N-m} - \delta_{2N+1,N+m+1} + 2(H_{1N-m} - H_{1N+m+1} - H_{1N} + H_{1N+1})]^{-1}. \quad (8.8)$$

Similarly, the tunneling and escape threshold voltages for the *combined soliton case*, are, respectively, given by $V_t^{ex-e}(0; m, N)$ and $V_t^{ex-e}(N; m, 0)$ because their absolute values are the largest for a combined soliton tunneling into the trap and for a combined soliton escaping from the trap, which are, respectively, obtained as

$$V_t^{ex-e}(0; m, N) = \frac{e}{C} \frac{H_{mm} + H_{NN} - 2H_{mN+1}}{2 + H_{1m} + H_{1N} - H_{1N+1} - H_{12N-m+1}}, \quad (8.9)$$

$$V_t^{ex-e}(N; m, 0) = -\frac{e}{C} \frac{H_{mm} - H_{NN} + H_{NN+1}}{1 - H_{1m} + H_{12N-m+1} + 2H_{1N} - 2H_{1N+1}}. \quad (8.10)$$

Equations (8.5)–(8.10) are general forms for the m -junctions cotunneling process, where solitons tunnel across m junctions at the same time. When $m = 1$, it becomes the special case of one junction tunneling.

An interesting phenomenon of the multi-junction trap, as in the measured $I-V$ curves [64] is the hysteretic loop, i.e. the tunneling and escape of a soliton do not occur at the same value of bias voltage V . Since we have obtained an analytic expressions for the threshold voltages for both the tunneling and escape of a single charge soliton in the single electron dual-junction-array trap, we can now study the hysteretic phenomenon in a quantitative way. For this purpose, we introduce the hysteretic voltage gap ΔV , which is defined as the difference between the threshold voltages for the tunneling and escape of a soliton in the single electron dual-junction-array trap. By this definition one can obtain the results for the hysteretic voltage gaps of a single-electron, an exciton, and a combined soliton with cotunneling transfer cases, respectively, as

$$\begin{aligned}\Delta V^e(m) &\equiv V_t^e(N, N-m) - V_t^e(0, m) \\ &= -\frac{e}{C} \left(\frac{H_{N-mN-m} - H_{NN}}{H_{1N-m} - H_{1N+m+1} - H_{1N} + H_{1N+1}} - \frac{H_{mm}}{1 + H_{1m} - H_{2Nm}} \right),\end{aligned}\quad (8.11)$$

$$\begin{aligned}\Delta V^{ex}(m) &\equiv V_t^{ex}(N, N-m) - V_t^{ex}(0, m) \\ &= \frac{e}{C} \left(\frac{H_{N-mN-m} - H_{N-mN+1+m} - H_{NN} + H_{NN+1}}{H_{1N-m} - H_{1N+m+1} - H_{1N} + H_{1N+1}} \right. \\ &\quad \left. - \frac{H_{mm} - H_{m2N-m+1}}{1 + H_{1m} - H_{12N-m+1}} \right),\end{aligned}\quad (8.12)$$

and

$$\begin{aligned}\Delta V^{ex-e}(m) &\equiv V_t^{ex-e}(N; m, 0) - V_t^{ex-e}(0; m, N) \\ &= -\frac{e}{C} \left(\frac{H_{mm} - H_{NN} + H_{NN+1}}{1 - H_{1m} + H_{12N-m+1} + 2H_{1N} - 2H_{1N+1}} \right. \\ &\quad \left. + \frac{H_{mm} + H_{NN} - 2H_{mN+1}}{2 + H_{1m} + H_{1N} - H_{1N+1} - H_{12N-m+1}} \right),\end{aligned}\quad (8.13)$$

where m denotes the number of junctions the electrons tunnel across. The ΔV of Eqs. (8.11)–(8.13) is a measure of the hysteretic effect for the *single charge soliton transfer* of the single electron dual-junction-array trap. When $\Delta V > 0$, there is a difference between the threshold voltages for the escape and tunneling of a charge soliton. After a charge soliton tunnels into the trap of system at a voltage above $V_t(0, m)$, the soliton cannot escape until the voltage is reduced to $V_t(N, N-m)$. Things are different at $\Delta V(m) < 0$, where a reduction of the voltage from $V_t(0, m)$ will immediately result in the escape of the soliton, i.e. the soliton cannot be trapped in the system. The quantities $V_t(N, N-m)$ and $V_t(0, m)$ are closely related to the lifetime for thermally activated escape and tunneling of a charge soliton, since the lifetime for thermally activated escape of a charge soliton from the trap is given [64] by $\tau_o \approx RC \exp[V_t(N, N-m)/k_B T]$ and the lifetime for thermally activated tunneling of a charge soliton into the trap is expressed by $V_t(0, m)$. Here T is the

temperature and k_B Boltzmann's constant, and R denotes the tunnel resistance in small tunnel junction. Therefore, the condition $\Delta V > 0$ means that the lifetime for the escape of a charge soliton is longer than that for the tunneling of a charge soliton, whereas, in the case of $\Delta V(m) < 0$, the lifetime for the escape of a charge soliton is shorter than that for the tunneling of a charge soliton. The hysteretic voltage gaps, together with the difference of the lifetime for the tunneling and escape of a charge soliton, strongly depend on the stray capacitance C , the input gate capacitance C_1 , the coupling capacitance C_C , the cotunneling m , and the number of junction N . Their dependence of the hysteretic voltage gaps can be analyzed using Eqs. (8.11)–(8.13). In the following, we study the C_0, C_C, C_1 , and m dependence of $\Delta V(m)$ by taking $N = 3$ as an example. The stray capacitance dependence of $\Delta V(1)$ (in units of e/C) for various charge solitons is illustrated by Fig. 31, where we plot the hysteretic voltage gap of Eqs. (8.11)–(8.13) as a function of the ratio of stray capacitance to the junction capacitance, i.e., $\eta (\equiv C_0/C)$ at $N = 3, m = 1$, and $\beta (\equiv C_1/C) = 0.5, 1, 5$ for two different coupling capacitances: (a) $\alpha (\equiv C_C/C) = 0.5$ and (b) $\alpha = 5$. This figure shows that all charge solitons, except for the single exciton in the case of $\alpha = 5$, have the maximum of hysteretic voltage gaps at $\eta = 0$ for all given β and α , and their hysteretic voltage gaps are decreased as the value of η is increased. For all given β and $\alpha = 5$, the hysteretic voltage gaps of single exciton have a more complicated dependence on the value of η : they reach their maximum value at some finite value of η , and then decrease with the increase of η , as shown in Fig. 30(b), where the maximum value of the hysteretic voltage gap depends on the value of β . As can be seen from Fig. 30(a), in the case of $\eta = 0$ the hysteretic voltage gaps of exciton are highest than those of any other charge solitons for all given β . This means that the difference of the lifetime for the tunneling and escape

of exciton is largest than that of any other solitons. Hence, the use of single exciton

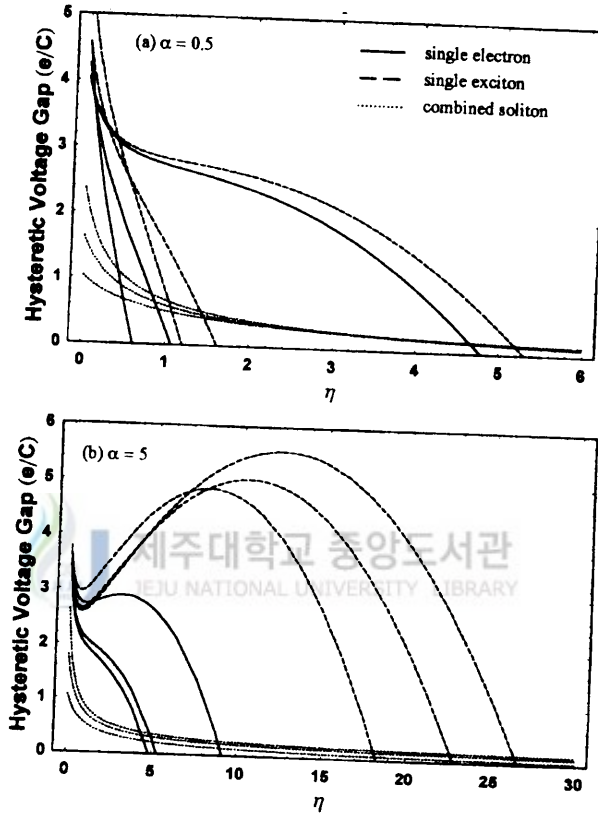


FIG. 30. The hysteretic voltage gaps $\Delta V(1)$ (in units of e/C) of a single electron dual-junction-array trap with $N = 3$ for various charge solitons, as a function of C_0/C at (a) $C_1/C = 0.5, 1, 5$ (from left-hand side to right-hand side of the bottom for solid lines and dashed lines, and from top to bottom of the left-hand side for dotted lines) for $C_C/C = 0.5$ and (b) $C_1/C = 0.5, 1, 5$ (from left-hand side to right-hand side of the bottom for solid lines, from right-hand side to left-hand side of the bottom for dashed lines, and from top to bottom of the left-hand side for dotted lines) for $C_C/C = 5$. Here C_C , C_1 , C , and C_0 are the coupling capacitances, input gate capacitances, junction capacitances, and stray capacitances, respectively.

can be possibly useful for constructing more stable single electron circuits, as suggested by Amakawa et al. [66]. When the value of β is small and the value of η is large, the hysteretic voltage gaps of combined soliton are highest. Hence, the difference of the lifetime for the tunneling and escape of combined soliton is largest than that of any other solitons. If the value of β is increased or the value of α is increased as shown in Fig. 30(b), the difference of the lifetime for the tunneling and escape of single exciton becomes largest for large η . It is interesting to note that the value of η mainly contributes to decrease the hysteretic voltage gaps for all charge soliton, except for single exciton case for large α . The another remarkable thing in this figure is that for all given α , β , and γ , the hysteretic voltage gaps of all charge solitons, except for the combined soliton, approach zero as the value of η increases. In zero hysteretic voltage gap, no hysteresis loop exists and the lifetime for the tunneling and escape of exciton is same. In consequence, all charge solitons cannot be trapped in the system. As can be seen from the figure, the critical stray capacitances η_c at which $\Delta V(1) = 0$ strongly depend on the values of α and β . For small α , the critical stray capacitances of single electron and single exciton increase with the increase of the value of β . However, for large α the critical stray capacitances of single electron increase as the value of β increases, whereas those of single exciton decrease with the increase of the value of β . Moreover, it is shown in Figs. 30(a) and 30(b) that for a fixed value of β the critical stray capacitances of all charge solitons increase with the increase of the value of α . The dependence of the critical stray capacitances on parameters given in the system can be readily obtained by putting $\Delta V(1) = 0$ in Eqs. (8.11)–(8.13). The detailed investigation will be discussed later.

The hysteretic voltage gap (in units of e/C) for various charge solitons is shown

in Fig. 31, as a function of α at $N = 3$, $m = 1$, and $\beta = 0.5, 1, 5$ for two different

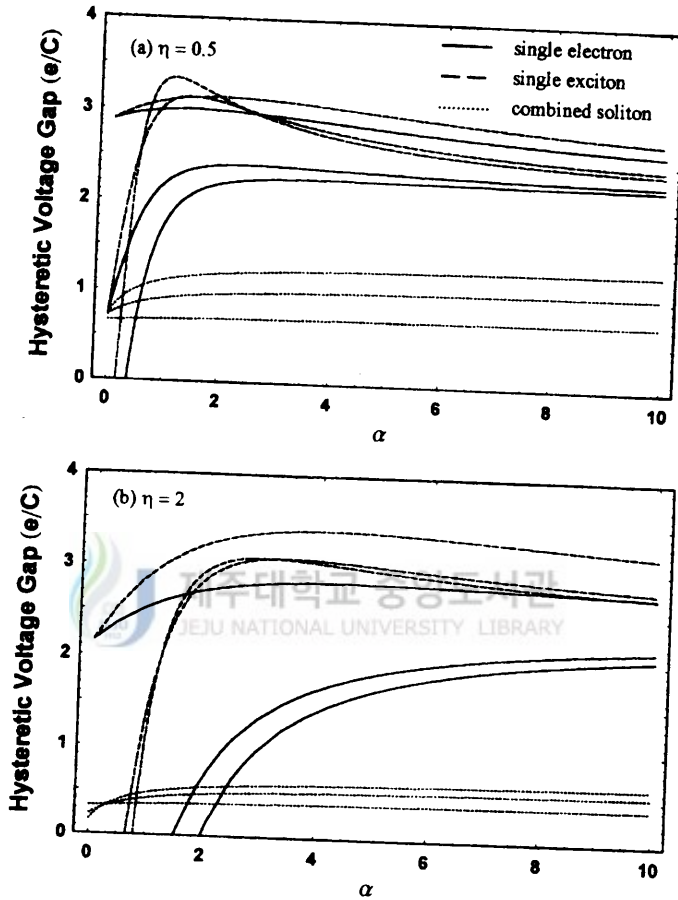


FIG. 31. The hysteretic voltage gaps $\Delta V(1)$ (in units of e/C) of a single electron dual-junction-array trap with $N = 3$ for various charge solitons, as a function of C_C/C at (a) $C_1/C = 0.5, 1, 5$ (from bottom to top of the left-hand side for solid lines and dashed lines, and from top to bottom for dotted lines) for $C_0/C = 0.5$ and (b) $C_1/C = 0.5, 1, 5$ (from bottom to top of the right-hand side for solid lines and dashed lines, and from top to bottom of the right-hand side for dotted lines) for $C_0/C = 2$. Here C_C , C_1 , C , and C_0 are the coupling capacitances, input gate capacitances, junction capacitances, and stray capacitances, respectively.

stray capacitances: (a) $\eta = 0.5$ and (b) $\eta = 2$. It can be seen from the figure that, for all given β and η the hysteretic voltage gaps of all charge solitons reach their maximum value at some finite α and then remain constant or decrease, depending on the value of β as the value of α increases. As shown in Fig. 31(a) for $\eta = 0.5$, if the value of β increases, the hysteretic voltage gaps of combined soliton decrease for all given α , whereas those of single electron increase. However, the hysteretic voltage gaps of single exciton increase, except for a specific α region. In the specific α region, the hysteretic voltage gaps of single exciton decrease and then increase with the increase of the value of β , depending on the value of η , as shown in Figs. 31(a) and 31(b). In very small α region, the hysteretic voltage gaps of combined soliton show two different features as the value of η increases. When the value of η is small, the hysteretic voltage gaps of combined soliton decrease with the increase of the value of β , whereas when the value of η is large, those of combined soliton increase with the increase of the value of β . In addition, for $\eta = 0.5$ and $\beta = 0.5$, the hysteretic voltage gaps of combined soliton are highest than those of any other charge solitons in very small α region. However, if the value of α increases, the hysteretic voltage gaps of exciton are highest than those of any other charge solitons. As shown in Fig. 31(b), if the value of η increases, the highest region of combined soliton increases. In this region, the difference of the lifetime for the tunneling and escape of combined soliton is longest.

Figure 32 shows the cotunneling m dependence of the hysteretic voltage gaps $\Delta V(m)$ (in units of e/C) for various charge solitons at $\alpha = 0.5$, $\beta = 5$, and $N = 10$, for different stray capacitances: $\eta = 0.005, 0.05, 0.5$. It can be seen from the figure that the hysteretic voltage gaps of single electron and single exciton at fixed values of α , β , and η become smaller for larger m . However, those of combined

soliton increase slightly and then decrease or remain constant for given η as the cotunneling increases. When the value of η is increased, the hysteretic voltage gaps of combined soliton are lowered for all given m , whereas those of single electron and single exciton have some interesting features, depending on the cotunneling: their hysteretic voltage gaps at $\eta = 0.005$ change from lowest for small m to highest for large m .

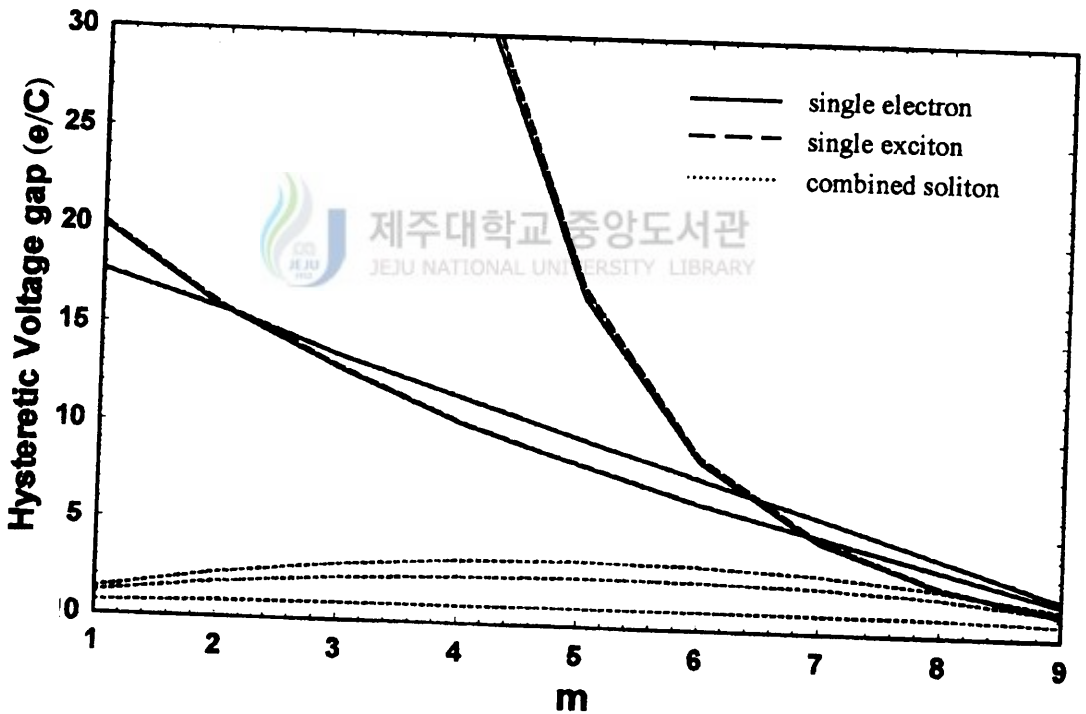


FIG. 32. The hysteretic voltage gaps $\Delta V(1)$ (in units of e/C) of a single electron dual-junction-array trap with $N = 10$ for various charge solitons, as a function of cotunneling m at $C_C/C = 0.5$ and $C_1/C = 5$ for $C_0/C = 0.005, 0.05,$ and 0.5 (from top to bottom of the right-hand side). Here $C_C, C_1, C,$ and C_0 are the coupling capacitances, input gate capacitances, junction capacitances, and stray capacitances, respectively.

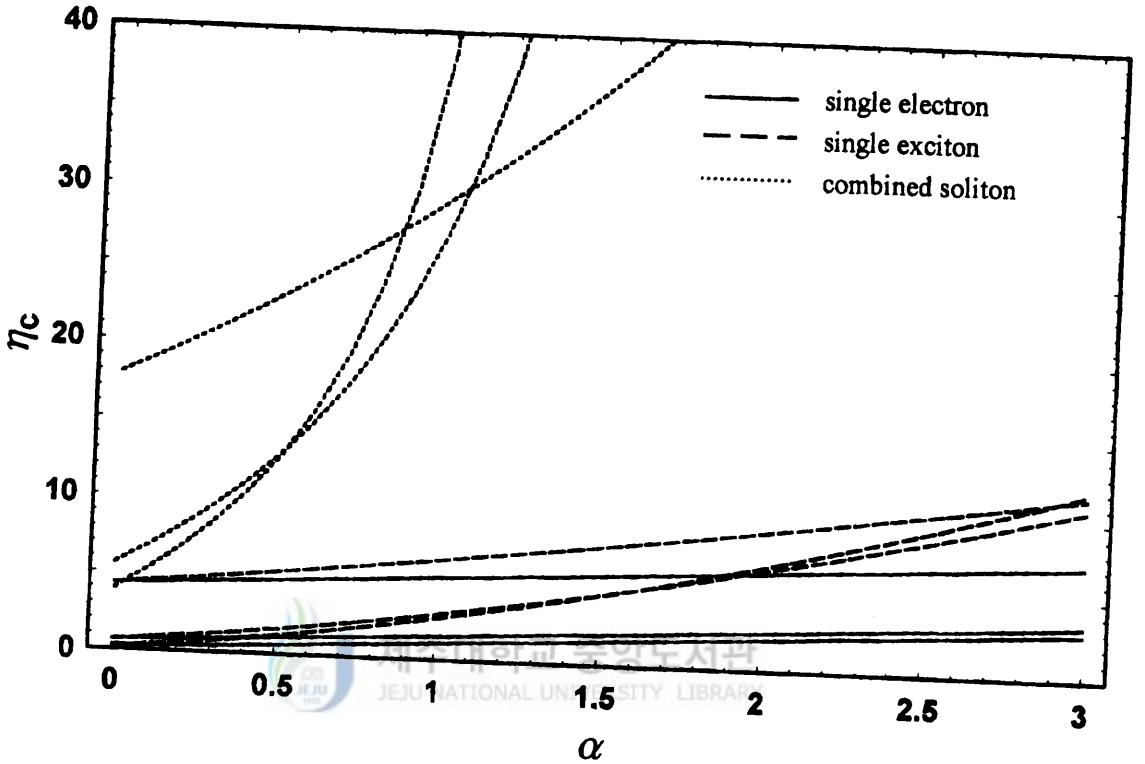


FIG. 33. The critical value η_c of C_0/C at which $\Delta V = 0$ for various charge solitons, as a function of C_C/C at $C_1/C = 0.5, 1, 2$ (from bottom to top of the left-hand side) for $m = 1$ and $N = 3$. Here, N is the number of tunneling junctions on each side of the single electron dual-junction-array trap and C_C , C_1 , C , and C_0 are the coupling capacitances, input gate capacitances, junction capacitances, and stray capacitances, respectively. For every point above each line there is no hysteresis.

Next, we study the α , β , and N dependence of the critical stray capacitances (η_c) in more detail, by taking $m = 1$ as an example. Their dependence of the critical stray capacitances can be readily obtained by putting $\Delta V(1) = 0$ in Eqs. (8.11)–(8.13), as discussed above. Since the analytical results of η_c have complicated forms, we present some results numerically in the following. The general relationship

between η_c and α for various charge solitons is illustrated in Fig. 33, where we plot η_c as a function of α at $\beta = 0.5, 1, 5$ for $N = 3$ and $m = 1$. As expected in Fig. 30, we can see from Fig. 33 that the critical stray capacitances of single electron increase slightly with the increase of the values of α and β , whereas those of single exciton and combined soliton increase with the increase of the value of α for all given β , but they have a more complicated dependence on the value of β for fixed values of α . In small α region, their critical stray capacitances increase with the increase of the value of β . However, they decrease with the increase of the value of β , except for specific regions of α , as the value of α increases. The N dependence of the critical stray capacitances for various charge solitons according to the value of β at $\alpha = 0.5$ and $m = 1$ is presented in Fig. 34. It can be seen from the figure that for given α and β , the changes of the critical stray capacitances of all charge solitons are expected for $N < 3$ and they are not influenced by the number of junction for $N \geq 3$ since they remain constant according to the number of junction. Moreover, for a fixed value of N , the critical stray capacitances for all charge solitons increase with the increase of the value of β .

So far, we have obtained the hysteretic voltage gaps of the single electron dual-junction array trap with equal stray capacitances for various charge solitons including a single electron, an exciton, and a combined soliton. With the obtained analytical results, we have performed the numerical analysis of the hysteretic voltage gaps, in order to understand their dependence on the stray capacitance, the coupling capacitance, the input gate capacitance, and the cotunneling. In addition, we have investigated the α , β , and N dependence of the critical stray capacitances (η_c) at which $\Delta V(1) = 0$ in Eqs. (8.11)–(8.13). Unfortunately, we don't have any experimental results of the single electron dual-junction array trap, except for Amakawa et

al.'s numerical results [66] obtained for no stray capacitance and weak coupling and input gate capacitances. Our results show that the hysteretic voltage gaps, together with the lifetime for the tunneling and escape of a charge soliton, strongly depend on the stray capacitance C , the input gate capacitance C_1 , the coupling capacitance C_C , and the cotunneling m . The hysteretic voltage gaps of exciton at $\alpha = 0.5$ and $\eta = 0$ for all given β are highest than that of any other charge solitons.

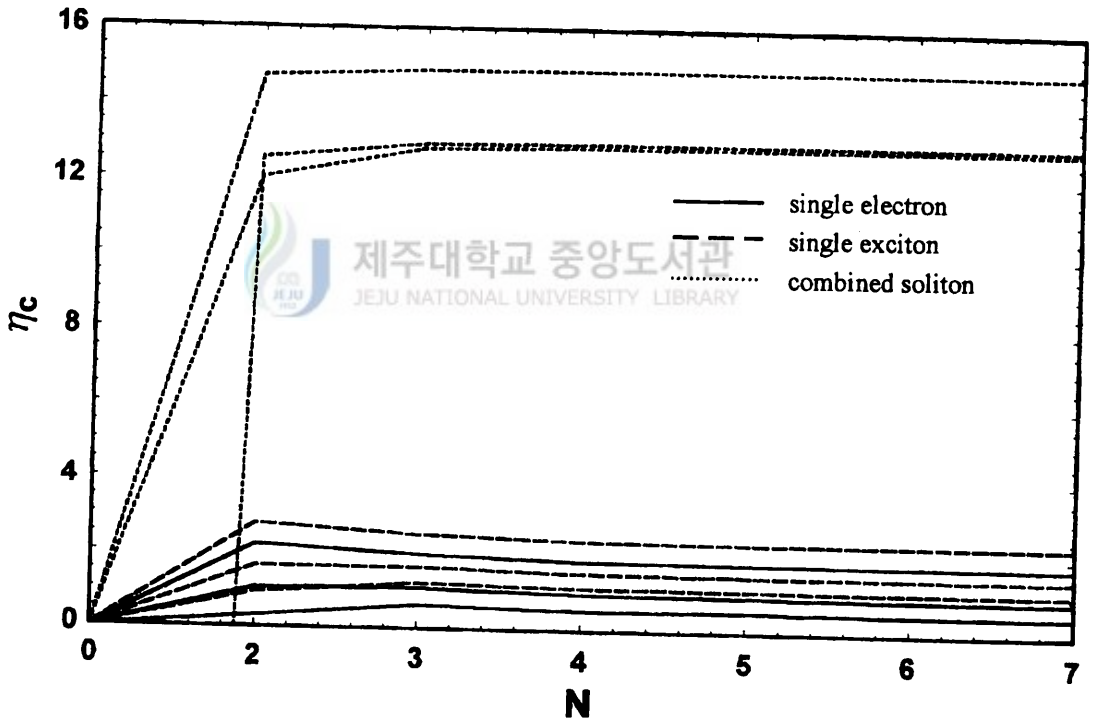


FIG. 34. The critical value η_c of C_0/C for $\Delta V = 0$ for various charge solitons, as a function of N at $C_1/C = 0.5, 1, 2$ (from bottom to top of the right-hand side) for $m = 1$ and $C_C/C = 0.5$. Here, N is the number of tunneling junctions on each side of the single electron dual-junction-array trap and C_C , C_1 , C , and C_0 are the coupling capacitances, input gate capacitances, junction capacitances, and stray capacitances, respectively. For every point above each line there is no hysteresis.

This indicates that the difference of the lifetime for the tunneling and escape of exciton is largest than that of any other solitons. Hence, the use of single exciton can be possibly useful for constructing more stable single electron circuits, as suggested by Amakawa et al. [66]. However, when the value of β is small and the value of η is large, the hysteretic voltage gaps of combined soliton is highest. This means that the combined soliton can be a candidate for constructing more stable single electron circuits. It is noted that if the value of β is increased or the value of α is increased, the difference of the lifetime for the tunneling and escape of single exciton becomes largest for large η . Moreover, the hysteretic voltage gaps of all charge solitons are very sensitive to the cotunneling effect. It is shown that the hysteretic voltage gaps of single electron and single exciton decrease with the increase of cotunneling, whereas the combined soliton has different dependence of the hysteretic voltage gaps on the cotunneling. They increase and then decrease or remain constant as the cotunneling increases. In addition, the critical stray capacitances in which no hysteresis is expected depend on the coupling capacitor C_C , the junction capacitance C , the input gate capacitance C_1 , and the number of junction, as well as the cotunneling. For given conditions, a lot of their changes are expected in terms of the values of α and β , rather than the number of junction.

In conclusion, the hysteretic voltage gaps, together with the lifetime for the tunneling and escape of a charge soliton, are very sensitive to the stray capacitance C , the input gate capacitance C_1 , the coupling capacitance C_C , the cotunneling m , and the number of junction N . A single exciton or a combined soliton can be a candidate for constructing more stable single electron circuits, depending on their parameters in the system. We expect the quantitative or qualitative behavior investigated in this paper to provide useful information pertaining to future experiments.

IX. CONCLUSIONS

So far we have studied theoretically two topics in nanostructures: (1) quantum transport phenomena such as EPR effect in low-dimensional systems with various confinement potentials including a parabolic well, a square well, and a triangular well, and MPR effect in bulk and low-dimensional electronic systems, and (2) single electron dynamics in single electron dual-junction-array trap. The results are summarized in the following:

In chapter 2, we have presented a theory of electric-field-induced MPR in n -Ge for the transverse configuration and obtained the MPR conditions given in Eqs. (2.21) and (2.24). As can be seen from Eqs. (2.21) and (2.24), MPR peak positions for the intervalley scattering by phonons strongly depend on the strength of the electric field, the possible phonon energy, the difference of Landau-level indices, and the magnetic field direction which leads to the difference in the effective mass between the initial and final states. Our results show that double peaks take place according to the non-vertical transition due to the intracollisional field effect. One of the peaks is shifted to the lower magnetic-field side and the other is shifted to the higher magnetic-field side as electric fields are increased and as the possible phonon energy and the difference of Landau-level indices are decreased.

In chapter 3, we have investigated the essential physics of the MPR effects in quasi-two-dimensional electronic system brought about by the electron confinement due to the electrostatic potential and the magnetic confinement by tilting a magnetic field. Qualitative features of the MPR effects according to the strength of the electrostatic potential and the tilt angle of the applied magnetic field were discussed in detail, based on a simple model of parabolic confining potential.

In chapter 4, we have studied the MPR and EPR effects for a Q1D quantum-wire structure in the presence and absence of any magnetic field, in which a Q1DEG is confined by a parabolic well in the y direction and three kinds of confinement potentials in the z direction, including the parabolic well, the square well, and the triangular well. The relaxation rates (and hence the transverse magnetoconductivity) show resonant behaviors: MPR at $P\tilde{\omega}_c = \omega_L$ and at $P\tilde{\omega}_c = \omega_L \pm \omega_{n'n}$ and EPR due to the subband in the z direction at $\omega_{n'n} = \omega_L$, which strongly depends on the subband structure in the z direction. Occupation of several electric subbands gives rise to the additional oscillatory behavior of MPR effect and EPR effect. It should be noted that the MPR and EPR peak positions are strongly sensitive to the strength of the magnetic field, the optical phonon energy, the characteristic frequency of the y -directional confinement Ω_y , and the type of the confinement potential well in the z direction.

In chapter 5, we have derived the conductivity σ_{yy} for Q1D electronic systems subjected to crossed electric ($\mathbf{E}||\hat{y}$) and magnetic fields $\mathbf{B} = (B_x, 0, B_z)$, based on a simple model of parabolic confining potentials and obtained the MPR conditions in the quantum limit condition, as a function of the strength (B) and tilt angle (θ) of the applied magnetic field (\mathbf{B}), as well as the strength of the parabolic potential parameters (ω_1 and/or ω_2). With the MPR conditions, we have investigated the physical characteristics of the MPR effects, according to the tilt angle of the applied magnetic field and the relative strength of the confining potential parameters, in such low dimensional systems. In particular, we have studied the qualitative features of the MPR effects, their physical origin, and the dimensional crossover between Q2D and Q1D systems associated with the confining potential in tilted magnetic fields and compared with the existing theoretical results because we are not aware of any

relevant experimental work on MPR on the dependence of the tilted magnetic field on the σ_{yy} for Q1D electronic systems.

In chapter 6, we have derived the longitudinal magnetoconductivity σ_{zz} for a simple model of superlattices and obtained the MPR conditions and an energy range in which the relaxation rates are allowed. With the MPR conditions and the obtained energy range, we have investigated the physical characteristics of the MPR effects in such superlattice systems. In particular, we have studied the qualitative features of the MPR effects, according to the miniband width and the temperature parameters and compared with the existing experimental [56,57] and theoretical [58] results.

In chapters 7 and 8, we have presented an exact solution for the potential profiles of the biased single electron dual-junction- array trap with equal stray capacitances. With the obtained threshold voltage, we have performed the numerical analysis, in order to understand the dependence of threshold voltages on the stray capacitance, the coupling capacitance, the input gate capacitance, and the number of junction, as well as the cotunneling. For no stray capacitance and weak coupling and input gate capacitances, the exciton transport becomes dominant in the system. However, if the input gate capacitance is increased, the combined charge soliton has lowest threshold voltage than any other charge solitons and it becomes dominant in transport. Thus, for no stray capacitance, the solitons which are dominant in the system can be a single exciton or a combined soliton according to the input gate capacitance. For the case where the input gate capacitance is same as the junction capacitance, the dominant soliton in transport can be a combined soliton, a single electron, or an exciton, depending on the stray capacitance. In addition, for a specific coupling capacitance, the dominant soliton in transport can be a combined soliton, a single electron, or an exciton, according to the stray capacitance and the input gate ca-

capacitance. The hysteretic voltage gaps $\Delta V(m)$, together with the lifetime for the tunneling and escape of a charge soliton, has a strong dependence on m , C_0/C , C_1/C , C_C/C , and N , and that no hysteresis loop exists beyond a critical value of η_c of C_0/C . For no stray capacitance, as previously discussed in the literature, the exciton can be a candidate for constructing more stable single electron circuits but we find that in addition to the exciton, the combined soliton can be a candidate according to the effect of stray capacitances.



REFERENCES

- [1] R. J. Nicholas, *Prog. Quant. Electr.* **10**, 1 (1985).
- [2] V. L. Gurevich and Yu A. Firsov, *Sov. Phys. JETP* **13**, 137 (1961).
- [3] W. Xu, F. M. Peeters, and J. T. Devreese, *Phys. Rev. B* **48**, 1562 (1993).
- [4] J. Y. Ryu and S. D. Choi, *Phys. Rev. B* **44**, 11328 (1991).
- [5] P. Delsing, in *Single Charge Tunneling, Coulomb Blockade Phenomena in Nanostructures*, edited by H. Grabert and M. H. Devoret, (Plenum Press, New York, 1992), ch 7 and references therein.
- [6] G. Y. Hu, R. F. O'Connell, Y. B. Kang, and J. Y. Ryu, *Int. J. Mod. Phys. B* **10**, 2441 (1996).
- [7] L. Eaves, R. A. Stradling, and R. A. Wood, *Proc. X. Int. Conf. Phys. Semicond.*, Cambridge, p. 818 (1970); L. Eaves, R. A. Houl, R. A. Stradling, R. J. Tidley, J. C. Portal, and S. Askenazy, *J. Phys. C* **8**, 1034 (1975).
- [8] C. Hamaguchi, Y. Hirose, and K. Shimomae, in *Application of High Magnetic Fields in Semiconductor Physics*, Proceedings of the International Symposium, edited by G. Landwehr (Springer, Berlin, 1983), p. 423.
- [9] P. G. Harper, J. W. Hodby, and R. A. Stradling, *Rep. Progr. Phys.* **37**, 1 (1973).
- [10] B. K. Ridley, *Quantum Processes in Semiconductors*, (Clarendon Press, Oxford, 1993),

p. 316.

- [11] K. Yamada, N. Miura, N. Kamata, and H. Futagawa, *Physica B* **177**, 461 (1992).
- [12] H. Futagawa, N. Miura, K. Yamada, N. Kamata, A. Kowata, and C. Hamaguchi, *J. Phys. Soc. Jpn.* **62**, 4407 (1993).
- [13] D. K. Ferry and C. Jacoboni, *Quantum Transport in Semiconductors* (Plenum Press, New York, 1992), p. 3.
- [14] A. Suzuki, *Phys. Rev. B* **45**, 6731 (1992).
- [15] I. S. Gradshteyn and I. M. Ryzhik, *Table of Integrals, Series, and Products* (Academic, New York, 1965).
- [16] N. Mori, N. Nakamura, K. Taniguchi, and C. Hamaguchi, *J. Phys. Soc. Jpn.* **57**, 205 (1988).
- [17] R. T. Payne, *Phys. Rev.* **139**, A570 (1965).
- [18] G. Nilsson and G. Nelin, *Phys. Rev. B* **3**, 364 (1971).
- [19] S. C. Lee, J. Y. Kim, D. C. Kim, D. L. Kim, G. Hu, and J. Y. Ryu, *J. Kor. Phys. Soc.* **32**, 138 (1998).
- [20] P. Vasilopoulos, M. Charbonneau, and C. M. Van Vliet, *Phys. Rev. B* **35**, 1334 (1987).
- [21] M. A. Brummell, R. J. Nicholas, M. A. Hopkins, J. J. Harris, and C. T. Foxon, *Phys. Rev. Lett.* **58**, 77 (1987).
- [22] N. Mori, H. Murata, K. Taniguchi, and C. Hamaguchi, *Phys. Rev. B* **38**, 7622 (1988).

- [23] P. Vasilopoulos, P. Warmenbol, F. M. Peeters, and J. T. Devreese, *Phys. Rev. B* **40**, 1810 (1989).
- [24] N. Mori, H. Momose, and C. Hamaguchi, *Phys. Rev. B* **45**, 4536 (1992).
- [25] J. Y. Ryu, G. Y. Hu, and R. F. O'Connell, *Phys. Rev. B* **49**, 10437 (1994).
- [26] A. Suzuki and M. Ogawa, *J. Phys. C* **10**, 4659 (1998).
- [27] G. Y. Hu and R. F. O'Connell, *Phys. Rev. B* **40**, 11701 (1989).
- [28] J. M. Ziman, *Principles of the Theory of Solids* (Cambridge University Press, Cambridge, 1972), p. 319.
- [29] M. Prasad and M. Singh, *Phys. Rev. B* **29**, 4803 (1984).
- [30] P. Vasilopoulos, *Phys. Rev. B* **33**, 8587 (1986).
- [31] P. Warmenbol, F.M. Peeters, and J.T. Devreese, *Phys. Rev. B* **39**, 7821 (1989); **37**, 4694 (1988).
- [32] Y. I. Moon, S. D. Choi, B. S. Zhang, S. Oh, and J. Y. Ryu, *J. Kor. Phys. Soc.* **28**, 334 (1995).
- [33] S. Komiyama, H. Eyferth, and J. P. Kotthaus, *J. Phys. Soc. Jpn.* **49**, 687 (1980).
- [34] A. Kastalsky, F. M. Peeters, W. K. Chan, L. T. Florez, and J. P. Harbison, *Appl. Phys. Lett.* **59**, 1708 (1991).
- [35] J. Y. Ryu, and R. F. O'Connell, *Phys. Rev. B* **48**, 9126 (1993).
- [36] R. Kubo, *J. Phys. Soc. Jpn.* **12**, 570 (1957).

- [37] G. D. Mahan, *Many-Particle Physics* (Plenum, New York, 1981).
- [38] *Handbook of Mathematical Functions*, edited by M. Abramowitz and I. A. Stegun, Natl. Bur. Stand. Appl. Math. Ser. No. 55 (GPO, Washington, 1964).
- [39] F. F. Fang and W. E. Howard, Phys. Rev. Lett. **16**, 797 (1966).
- [40] T. S. Rahman, D. L. Mills, and P. S. Riseborough, Phys. Rev. B **23**, 4081 (1981).
- [41] D. C. Tsui, Th. Englert, A. Y. Cho, and A. C. Gossard, Phys. Rev. Lett. **44**, 341 (1980).
- [42] G. Ploner, J. Smoliner, G. Strasser, M. Hauser, and E. Gornik, Phys. Rev. **57**, 3966 (1998).
- [43] N. Mori, K. Taniguchi, C. Hamaguchi, S. Sasa, and S. Hiyamizu, J. Phys. C **21**, 1791 (1988).
- [44] M. A. Brummell, D. R. Leadley, R. J. Nicholas, J. J. Harris, and C. T. Foxon, Surf. Sci. **196**, 451 (1988).
- [45] D. R. Leadley, R. J. Nicholas, J. Singleton, W. Xu, F. M. Peeters, J. T. Devreese, J. A. A. J. Perenboom, L. van Bockstal, F. Herlach, J. J. Harris, and C. T. Foxon, Phys. Rev. Lett. **73**, 589 (1994).
- [46] G. Berthold, J. Smoliner, E. Gornik, G. Böhm, G. Weimann, T. Suski, P. Wisniewski, C. Hamaguchi, N. Mori, and H. Momose, Surf. Sci. **395**, 637 (1994).
- [47] G. Ihm, M. L. Falk, S. K. Noh, J. I. Lee, and S. J. Lee, Phys. Rev. B **46**, 15530 (1992).
- [48] J. Singh, *Physics of Semiconductors and Their Heterostructures* (McGraw-Hill, Sin-

gapore, 1993), p. 455.

- [49] Yu A. Firsov, V. L. Gurevich, R. V. Parfeniev, and S. S. Shalyt, *Phys. Rev. Lett.* **12**, 660 (1964).
- [50] Yu A. Firsov, V. L. Gurevich, R. V. Parfeniev, and S. S. Shalyt, *Phys. Rev. Lett.* **12**, 660 (1964).
- [51] R. A. Stradling and R. A. Wood, *J. Phys. C* **1**, 1711 (1968).
- [52] J. R. Barker, *J. Phys. C* **5**, 1657 (1972).
- [53] J. Y. Ryu, Y. C. Chung, and S. D. Choi, *Phys. Rev. B* **32**, 7769 (1985).
- [54] N. Sawaki, *Surface Sci.* **170**, 537 (1986).
- [55] W. Xu, F. M. Peeters, J. T. Devreese, D. R. Leadley, and R. J. Nicholas, *Int. J. of Mod. Phys. B* **10**, 169 (1996).
- [56] H. Noguchi, H. Sakaki, T. Takamasu, and N. Miura, *Phys. Rev. B* **45**, 12148 (1992).
- [57] P. Gassot, J. Genoe, D. K. Maude, J. C. Portal, K. S. H. Dalton, D. M. Symons, R. J. Nicholas, F. Aristone, J. F. Palmier, and F. Laruelle, *Phys. Rev. B* **54**, 14540 (1996).
- [58] W. M. Shu and X. L. Lei, *Phys. Rev. B* **50**, 17378 (1994).
- [59] K. K. Likharev, *IBM J. Res & Dev.* **32**, 144 (1988).
- [60] D. V. Averin, A. N. Korotkov, and Yu. V. Nazarov, *Phys. Rev. Lett.* **66**, 2818 (1991).
- [61] D. V. Averin, A. A. Odintsov, and S. V. Vyshenskii, *J. Appl. Phys.* **73**, 1297 (1993).
- [62] R. Bauernschmitt and Y. V. Nazarov, *Phys. Rev. B* **47**, 9997 (1993).

- [63] K. Nakazato, R. J. Blaikie, and H. Ahmed, *J. Appl. Phys.* **75**, 5123 (1994).
- [64] P. D. Dresselhaus, L. Ji, S. Han, J. E. Lukens, and K. K. Likharev, *Phys. Rev. Lett.* **72**, 3226 (1994).
- [65] L. R. C. Fonseca, A. N. Korotkov, K. K. Likharev, and A. A. Odintsov, *J. Appl. Phys.* **78**, 3238 (1995).
- [66] S. Amakawa, M. Fujishima, and K. Hoh, *Dual-junction-array single electron trap in the Electrochemical Society October meeting*, vol. **96-2**, 572 (1996).
- [67] M. Matters, J. J. Versluys, and J. E. Mooij, *Phys. Rev. Lett.* **78**, 2469 (1997).
- [68] K. A. Matsuoka, K. K. Likharev, P. Dresselhaus, L. Ji, S. Han, and J. Lukens, *J. Appl. Phys.* **81**, 2269 (1997).
- [69] D. V. Averin and A. A. Odintsov, *Phys. Lett. A* **140**, 251 (1989).
- [70] G. Y. Hu and R. F. O'Connell, *Phys. Rev. B* **54**, 1522 (1996).
- [71] J. Y. Ryu, S. C. Lee, G. Y. Hu, and C. S. Ting, *J. Phys. C* **12**, 4641 (2000).

CURRICULUM VITAE

Personal Information

- Name: Sang Chil Lee
- Date of Birth: February 22, 1966
- Place of Birth: Cheju, Republic of Korea
- Present Address: Department of Physics, Cheju National University,
Cheju 690-756, Republic of Korea
- E-mail Address: chills@hanmail.net



Education

- 1984. 3 – 1993. 2: Department of Science Education, Cheju National University (B. S. in Physics)
- 1994. 3 – 1996. 2: Department of Physics, Cheju National University (M. S. in Physics)
- 1996. 3 – 2000. 2: Department of Physics, Cheju National University (Ph. D. in Physics)

Teaching Experiences

- 1997. 3 – 1999. 2: Lecturer for undergraduate course, Department of Physics at Cheju National University

- 1999. 8 – 1999. 12: Teaching assistant for graduate course, Department of Physics at University of Houston, USA
- 2000. 9 – 2001. 2: Lecturer for undergraduate course, Department of Physics at Cheju National University

Research Experiences

- 1994. 3 – 1999. 2: Research Assistant, Department of Physics at Cheju National University, Supervisor : Prof. Jai Yon Ryu
- 1999. 2 – 2000. 1: Researcher, Texas Center for superconductivity at University of Houston, USA, Supervisor : Prof. C. S. Ting
- 1999. 12 – 2000. 11: '99 Young Research Fellow of Korea Research Foundation
- 2000. 2 – 2001. 2: Research Assistant, Department of Physics at Cheju National University, Supervisor : Prof. Jai Yon Ryu

Research Fields

- Theoretical Condensed Matter Physics: Quantum Transport, Single Charge Tunneling, Nanoelectronics, Mesoscopic Physics, Strongly Correlated Systems, Quantum Computer

Computer Skills

- Working knowledge of C, C++, Visual Basic, Java, Fortran, Matlab, Mathematica (mathlink), Interface

Memberships

- Korean Physical Society: Member (Since 1995)
- American Physical Society: Member (Since 2000)

Publication Lists

1. **Sang Chil Lee**, Jai Yon Ryu, Jung Dae Ko, Y. Yu, Dong Shik Kang, and Suck Whan Kim, “ Magnetophonon resonances in the miniband transport in semiconductor superlattices ”, Journal of Physics: Condensed Matter (submitted for publication).
2. **Sang Chil Lee**, Jai Yon Ryu, Doo Chul Kim, Dong Shik Kang, and Suck Whan Kim, “ Hysteretic Voltage Gap for a Single Electron Dual-Junction-Array Trap with Stray Capacitances ”, Journal of Physics: Condensed Matter (submitted for publication).
3. **Sang Chil Lee**, Suck Whan Kim, Jai Yon Ryu, and C. S. Ting, “ Magnetophonon resonances of a quasi-one-dimensional electron gas system in tilted magnetic fields ”, Phys. Rev. B **62**(8), 5045 (2000).
4. Jai Yon Ryu, Suck Whan Kim, **Sang Chil Lee**, and C. S. Ting, “ Orbital magnetic susceptibility of a quasi-one-dimensional electron gas system in tilted magnetic fields ”, Phys. Rev. B **62**(1), 385 (2000).
5. **Sang Chil Lee**, Jai Yon Ryu, G. Y. Hu, and C. S. Ting, “ Exact solution of the electrostatic problem for a single-electron-dual-junction array trap ”, Journal of Physics: Condensed Matter **12**, 4641 (2000).

6. **Sang Chil Lee**, Ho Joeng Ko, Young Bong Kang, G. Y. Hu, and Jai Yon Ryu, “ Coulomb Blockade in a Multiple Tunnel-Junction System with Dual Gates ”, Journal of Korean Physical Society **34**(2), 154 (1999).
7. **Sang Chil Lee**, D. S. Kang, Jai Yon Ryu, Suck Whan Kim, and Hyung Soo Ahn, “ Magnetophonon Resonance of Quasi-Two-Dimensional Electronic System in Tilted Magnetic Fields ”, Journal of Korean Physical Society **34** (supp. 1), S115 (1999).
8. **Sang Chil Lee**, Y. Yu, D. S. Kang, D. C. Kim, C. K. Choi, and J. Y. Ryu, “ Coulomb Blockade in Turnstile with Multiple Tunnel Junctions ”, Journal of Korean Physical Society **34** (supp. 1), S109 (1999).
9. Yong Bong Kang, Dong Shik Kang, **Sang Chil Lee**, G. Y. Hu, and Jai Yon Ryu, “ Effect of Stray Capacitances on the Coulomb Blockade Threshold in a 3N-pump ”, Sae Mulli **39**(1), 318 (1999).
10. **Sang Chil Lee**, Y. B. Kang, J. Y. Ryu, G. Y. Hu, and S. D. Choi, “ Transverse electric-field-induced magnetophonon resonance in n-type Germanium ”, Physical Review B **57**(19), 11875 (1998).
11. **Sang Chil Lee**, J. Y. Kim, D. C. Kim, D. L. Kim, G. Y. Hu, and J. Y. Ryu, “ Transverse and Longitudinal Hot-Electron Magnetophonon Resonances in n-type Germanium ”, Journal of Korean Physical Society **32**(2), 138 (1998).
12. **Sang Chil Lee**, Yong Bong Kang, Jai Yon Ryu, Suck Whan Kim, and Hyung Soo Ahn, “ Magnetophonon and Electrophonon Resonance Effects in Quasi-Two-Dimensional Quantum Wells ”, Sae Mulli **38**(6), 427 (1998).

13. **Sang Chil Lee**, Dong Shik Kang, D. C. Kim, K. Y. Kim, D. L. Kim, and Jai Yon Ryu, “ Transverse and Longitudinal Hot-Electron Magnetophonon Resonances in n-type Silicon ”, *Sae Mulli* **38**(5), 365 (1998),
14. **Sang Chil Lee**, Y. B. Kang, D. C. Kim, and Jai Yon Ryu, N. L. Kang, and S. D. Choi, “ Magnetophonon and Eelectrophonon Resonances in Quantum Wires ”, *Physical Review B* **55**(11), 6719 (1997).
15. Y. I. Moon, Y. J. Lee, S. D. Choi, **Sang Chil Lee**, D. C. Kim, and Jai Yon Ryu, “ A Theory of Hot-Electron Quantum Magneto-transport in Quasi-Two-Dimensional Quantum Wells ”, *Journal of Korean Physical Society* **30**(2), 252 (1997).
16. Yong Bong Kang, Yong Jai Cho, **Sang Chil Lee**, and Jai Yon Ryu, “ Exact Solution for the Charge Soliton in a 2N-Turnstile ”, *Journal of Korean Physical Society* **29**(1), 129 (1996).
17. Boo Sun Zhang, **Sang Chil Lee**, D. C. Kim, Jai Yon Ryu, Sung Hwa Park, Yong Jai Cho, Kyu Soon Bae, and Sang Don Choi, “ A Study of the Hot-electron Magnetophonon Resonance Effect ”, *Sae Mulli* **36**(3), 242 (1996).

Conference Activities

1. **Sang Chil Lee**, Ho Jung Koh, Young Bong Kang, G. Y. Hu, and Jai Yon Ryu, “ Coulomb Blockade in an Asymmetric N-turnstile ”, The 5th Joint Symposium of Nagasaki University and Cheju National University on Science and Technology, 23-25,197, Nagasaki University, Japan (1998).

2. J. Y. Ryu, **Sang Chil Lee**, Y. B. Kang, and G. Y. Hu, “ Single Electron Dual Junction Array Trap with Stray Capacitances ”, Bulletin of the American Physical Society, 43(1), 426 (1998).
3. **Sang Chil Lee**, Y. Yu, D. C. Kim, C. K. Choi and Jai Yon Ryu, “Coulomb Blockade in Single Electron Pump and Single Electron Turnstile with Multiple Tunnel Junction ”, International Workshop on Physics and Applications of Semiconductor Quantum Structures, C68 (1998).
4. **Sang Chil Lee**, Jai Yon Ryu, Suck Whan Kim, “ Magnetophonon Resonances of Quasi-Two-and One-Dimensional Electronic Systems in Tilted Magnetic Fields ”, International Workshop on Physics and Applications of Semiconductor Quantum Structures, C69 (1998).
5. **Sang Chil Lee**, H. J. Koh, Y. B. Kang, J. Y. Ryu, G. Y. Hu, Sang Don Choi, “ Coulomb Blockade in Multiple Tunnel-Junction System with Two Gates ”, 한국물리학회 대구경북지부 창립 35주년 기념학술회의, p. 204 경북대학교 (1998).
6. **Sang Chil Lee**, Y. B. Kang, G. Y. Hu, and J. Y. Ryu, “ Single electron Dual Junction Array Trap with Stry Capacitances ”, Bulletin of the Korean Physical Society, 15(2), 237 (1997).
7. **Sang Chil Lee**, H. J. Koh, J. Y. Kim, and J. Y. Ryu, “ Magnetophonon and Electrophonon Resonances in Quantum Wires ”, Bulletin of the Korean Physical Society, 15(1), 75 (1997).
8. J. Y. Kim, **Sang Chil Lee**, Y. B. Kang, and J. Y. Ryu, “ Transverse and Longitudinal Hot-Electron Magnetophonon Resonances in n-type Germanium

- ”, Bulletin of the Korean Physical Society, 15(1), 75 (1997).
9. H. J. Koh, **Sang Chil Lee**, Y. B. Kang, and J. Y. Ryu, “ Coulomb Blockade in Few Gated Small Junction Systems ”, Bulletin of the Korean Physical Society, 15(1), 75 (1997).
 10. **Sang Chil Lee**, Ho. J. Koh, J. Y. Kim, Y. B. Kang, and J. Y. Ryu, “ Magnetophonon and Electrophonon Resonances in Quasi-Two Dimensional Quantum Wells ”, Bulletin of the Korean Physical Society, 14(2), 35 (1996).
 11. B. S. Zhang, **Sang Chil Lee**, D. C. Kim, and J. Y. Ryu, “ A Study of the Hot-electron Magnetophonon Resonance Effect ”, Bulletin of the Korean Physical Society, 14(1), 121(1996).
 12. **Sang Chil Lee**, B. S. Zhang, Tae Cheol An, and J. Y. Ryu, “Hot-electron magnetophonon resonance in n-type Germanium ”, Bulletin of the Korean Physical Society, 13(2), 322 (1995).

감사의 글

7년 동안의 대학원 생활을 지내고 보니 참으로 많은 것을 배우고 느낀 소중한 시간이었습니다. 먼저, 대학원 생활과 학위논문을 무사히 마치도록 지도와 격려를 해주신 류재연 교수님께 감사드립니다. 교수님은 특유의 성실함으로 대학원 생활 내내 저를 이끌어 주었습니다. 또한 저에게 충고와 격려를 하여 주신 모든 교수님들께 진심으로 감사를 드립니다.

제가 졸업하기까지는 주위의 많은 사람들의 도움이 있었으며 그 분들에게 이 글을 통해 고마운 마음을 전합니다. 어렵고 힘들 때 힘이 되어준 과학교육과 졸업 동창들과 교수님, 물리학과 대학원생들, 그리고 저의 졸업을 누구보다도 기뻐하실 부모님과 두 동생, 외삼촌께 이 기쁨과 보람을 전하고자 합니다.

이 학위논문은 한국학술진흥재단의 1999년도 신진연구인력 연구장려금 지원 사업을 통한 연구비 지원으로 이루어졌습니다. 경제적 어려움 없이 학위 논문을 완성할 수 있도록 도와준 재단에 감사드립니다.